AD-A115 443 MASSACHUSETTS INST OF TECH LEXINGTON LINCOLN LAB F/G 20/5
REMOTE SENSING OF TURBINE ENGINE GASES.(U)
SEP 81 D K KILLINGER, N MENYUK, A MOORADIAN F19628-80-C-0002
UNCLASSIFIED ESD-TR-82-014 NL

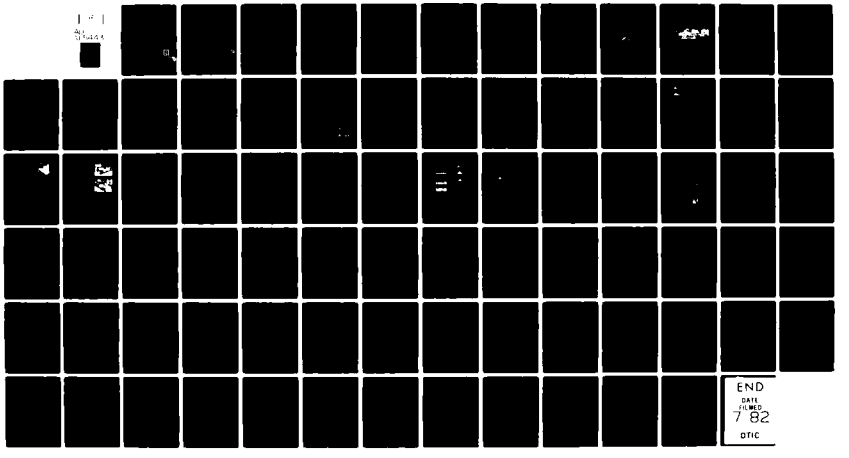

END
DATE FILMED
7-82
DTIC

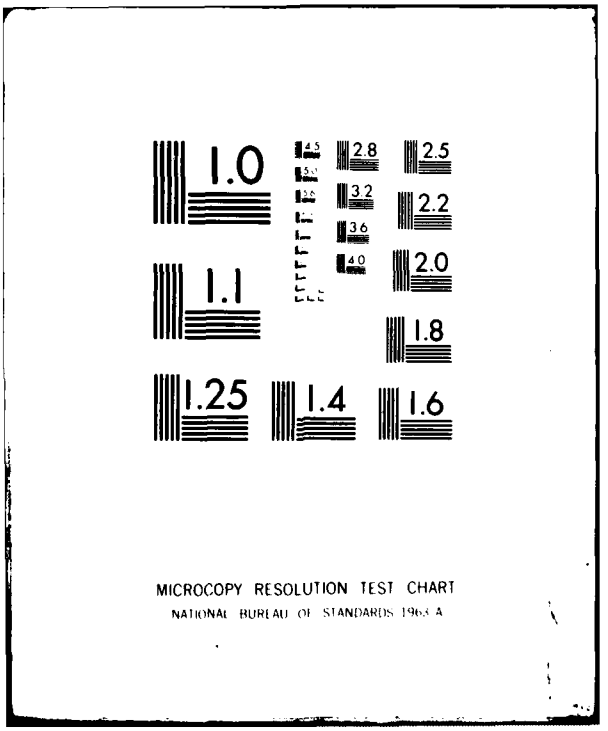
1.0
1.1
1.25
1.4
1.6
1.8
2.0
2.2
2.5
2.8
3.2
3.6
4.0
MICROCOPY RESOLUTION TEST CHART
NATIONAL BUREAU OF STANDARDS 1963 A

ESD-TR-82-014
ESL-TR-82-016

Final Report

Remote Sensing of Turbine Engine Gases

30 September 1981

Prepared for the Department of the Air Force
under Electronic Systems Division Contract F19628-80-C-0002 by

Lincoln Laboratory
MASSACHUSETTS INSTITUTE OF TECHNOLOGY
LEXINGTON, MASSACHUSETTS

MASSACHUSETTS INSTITUTE OF TECHNOLOGY
LINCOLN LABORATORY

REMOTE SENSING OF TURBINE ENGINE GASES

D.K. KILLINGER
N. MENYUK
A. MOORADIAN
Group 82

FINAL REPORT
TO THE
AIR FORCE ENGINEERING AND SERVICES CENTER

1 OCTOBER 1980 — 30 SEPTEMBER 1981

ISSUED 5 APRIL 1982

LEXINGTON MASSACHUSETTS

Contents

I. INTRODUCTION

This is the FY 81 final report on the program entitled "Remote Sensing of Turbine Engine Gases" supported by the Air Force Engineering and Services Center (AFESC). The effort is part of a larger on-going program at Lincoln Laboratory to develop laser remote sensing techniques for the detection and identification of atmospheric species as a means for environmental monitoring and tactical detection and discrimination. Previous research for AFESC conducted during FY 79 and FY 80 is documented in Final Reports ESD-TR-79-319/ESL-TR-80-09 and ESD-TR-81-41/ESL-TR-81-16, respectively.[1,2]

The specific tasks which were conducted during FY 81 for this research program consisted of the following: (1) the feasibility demonstration of a dual-laser differential-absorption LIDAR (DIAL) system for the remote sensing of CO, NO, and C_2H_4, (2) the development of a data acquisition and processing system for the dual-laser DIAL system, (3) the laser remote sensing of CO and C_2H_4 in the exhaust of a stationary jet aircraft, and (4) the laser remote sensing of hydrazine, monomethylhydrazine (MMH), and unsymmetrical dimethylhydrazine (UDMH).

Each of the tasks is described in detail in the following sections. Supportive documentation is included in the appendices.

II. FEASIBILITY DEMONSTRATION OF DUAL-LASER DIAL SYSTEM

The direct-detection 10 μm dual-laser DIAL system as described in Ref. 2 was modified to permit operation at both 5 μm and 10 μm. A schematic of the dual-laser DIAL system is shown in Fig. 1. Two CO_2 lasers provided the tunable pulsed primary radiation near 10 μm; Laser 1 was tuned to the on-resonance absorption transition and Laser 2 was tuned to the off-resonance transition. Radiation near 5 μm was generated through use of $CdGeAs_2$ frequency-doubling crystals. The output radiation from the two lasers was then joined through use of a 50/50 beamsplitter, expanded in diameter by a factor of 10, and directed out the laboratory window toward topographic

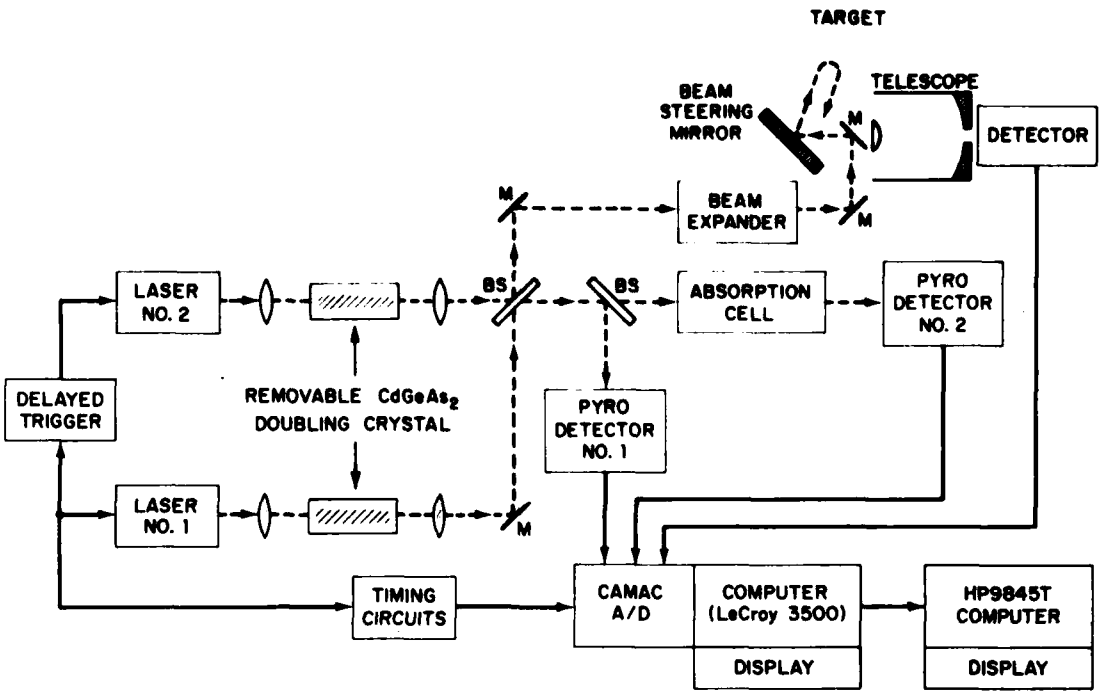

Fig. 1. Schematic of dual-CO_2 laser differential-absorption LIDAR (DIAL) system.

targets at ranges up to 2.7 km away. The pulsed LIDAR returns were collected by a 30 cm Cassegrainian telescope and detected by cooled HgCdTe detectors. The returned LIDAR signals were normalized to the laser energy in each pulse and calibrated for absorption through use of absorption cells in the laboratory. The output signals were analyzed in real time by the computerized data acquisition system.

The DIAL system shown in Fig. 1 was used to measure the path-averaged concentration of CO and C_2H_4 in the atmosphere. While NO was also detected near strong vehicular exhaust sources, the ambient concentration of NO in the atmosphere is less than our DIAL system sensitivity of approximately 10-20 ppb; the ambient level of NO is usually less than 1 ppb.

Concentrations of CO and C_2H_4 in the atmosphere as measured by the dual-laser DIAL system were found to be essentially similar to those measured previously[1,2] using a single-laser DIAL system. However, using the dual-laser DIAL system greatly improved the accuracy of the measurements, which were found to be limited by the effects of atmospheric turbulence. These results are presented in detail in Appendices A, B, and C. A synopsis of the results is given below.

The limiting factor in determining the accuracy, and hence sensitivity, of a DIAL system is often due to fluctuations in the LIDAR returns. These fluctuations, for a direct-detection system, are caused by perturbations imposed on the beam by atmospheric turbulence. A series of measurements was conducted to quantify these effects and the results can be summarized as follows:

1. Atmospheric fluctuations were measured to have time scales longer than 1-10 ms, dependent upon wind and atmospheric effects. For time periods less than this temporal correlation time, the atmosphere is essentially stationary.
2. A dual-laser DIAL system can eliminate the effects of atmospheric turbulence if both DIAL pulses are transmitted within this characteristic correlation time.

3. A theoretical model was developed that correctly predicts the increase in accuracy of a dual-laser DIAL system compared to a single-laser DIAL system. This model is based on the measured correlation time and statistical fluctuations of single-laser LIDAR returns.

As an example of the increase in sensitivity measured with the dual-laser system, it was found that the standard deviation of the DIAL measurement was approximately 7% for the single-laser DIAL system and 3% for the dual-laser DIAL system; this data was obtained using a diffuse target at a range of 2.7 km and integrating 100 pulses. These values correspond to a path-averaged DIAL sensitivity for the remote sensing of C_2H_4 in the atmosphere of 8 ppb for the single-laser DIAL system and 3.5 ppb for the dual-laser DIAL system for a range of 2.7 km (Appendix C).

These results have quantified the accuracy of these DIAL measurements and provided insight into the physical mechanisms that presently limit such measurements.

III. DEVELOPMENT OF DATA ACQUISITION AND PROCESSING SYSTEM FOR DUAL-LASER SYSTEM

The computerized data acquisition system, as described in Ref. 2, was originally developed for use with the single-laser DIAL system. This data acquisition system was modified both in hardware and in software in order to be used with the dual-laser DIAL system. The specifics of the computer system are presented in Appendix C. An overview of its capabilities are presented in the following.

A LeCroy 3500M computerized data acquisition system was used to acquire the high-speed LIDAR signals. The pulsed LIDAR returns were detected by two 11-bit peak-sensing A/D CAMAC modules (LeCroy Model No. 2259). The pulsed signals from the pyroelectric detectors were measured using two charge-integrating A/D CAMAC modules (LeCroy Model No. 2249SG). The 3500M was able to record the LIDAR pulses, normalize them to the laser energy in each pulse, and perform a statistical and temporal analysis of

the signals. This analysis was done in real time at laser pulse-repetition-rates of up to 50 to 100 Hz. Typical analysis included the calculation of the average value, standard deviation, and temporal correlation of the LIDAR returns as well as those pulses transmitted through the laboratory absorption cell (Fig. 1). In addition, the average concentration of the absorbing species in the atmosphere was calculated and displayed.

IV. LASER REMOTE SENSING OF CO AND C_2H_4 IN JET ENGINE EXHAUST

The dual-laser DIAL system was used to detect CO and C_2H_4 in the exhaust of an A-10 jet aircraft at a range of 2.7 km. An approximate schematic of the measurement geometry is shown in Fig. 2; the dual-laser DIAL system was located inside the Lincoln Laboratory Laser Remote Sensing Facility, and not on the roof as shown in Fig. 2. A photo of the A-10 jet aircraft is shown in Fig. 3; the A-10 aircraft was provided for a one-day experiment by Colonel Robert Reynolds and Captain Michael Bolanger of the 104th Tactical Fighter Group, Massachusetts Air National Guard.

The DIAL measurements utilized backscattered radiation from several targets behind the aircraft at a range of 2.7 km. The aircraft was situated approximately 15 m upwind from the LIDAR beam and the initial flow direction of the A-10 exhaust plume was perpendicular to the LIDAR beam direction. Temporal changes in the concentration of C_2H_4 were measured as the tethered A-10 engines were started, operated at a fast idle, and turned off. This was followed by similar measurements of the changing concentration of CO in the atmosphere as the A-10 engines were restarted and increased in speed.

Results for the remote sensing of ethylene (C_2H_4) are shown in Fig. 4. The measured path-averaged background concentration of C_2H_4 was approximately 2-5 ppb. Increases in the C_2H_4 concentration on the order of 5 ppb were observed when the A-10 started its engines; larger increases were evident when the engines were turned off.

Fig. 5 shows the results for the remote sensing of CO. As seen in the figure, the background path-averaged concentration of CO was about 400 ppb and increased by approximately 100 ppb when the A-10 started its engines. A decrease in CO was also observed when the engine speed was increased.

B82-3933A

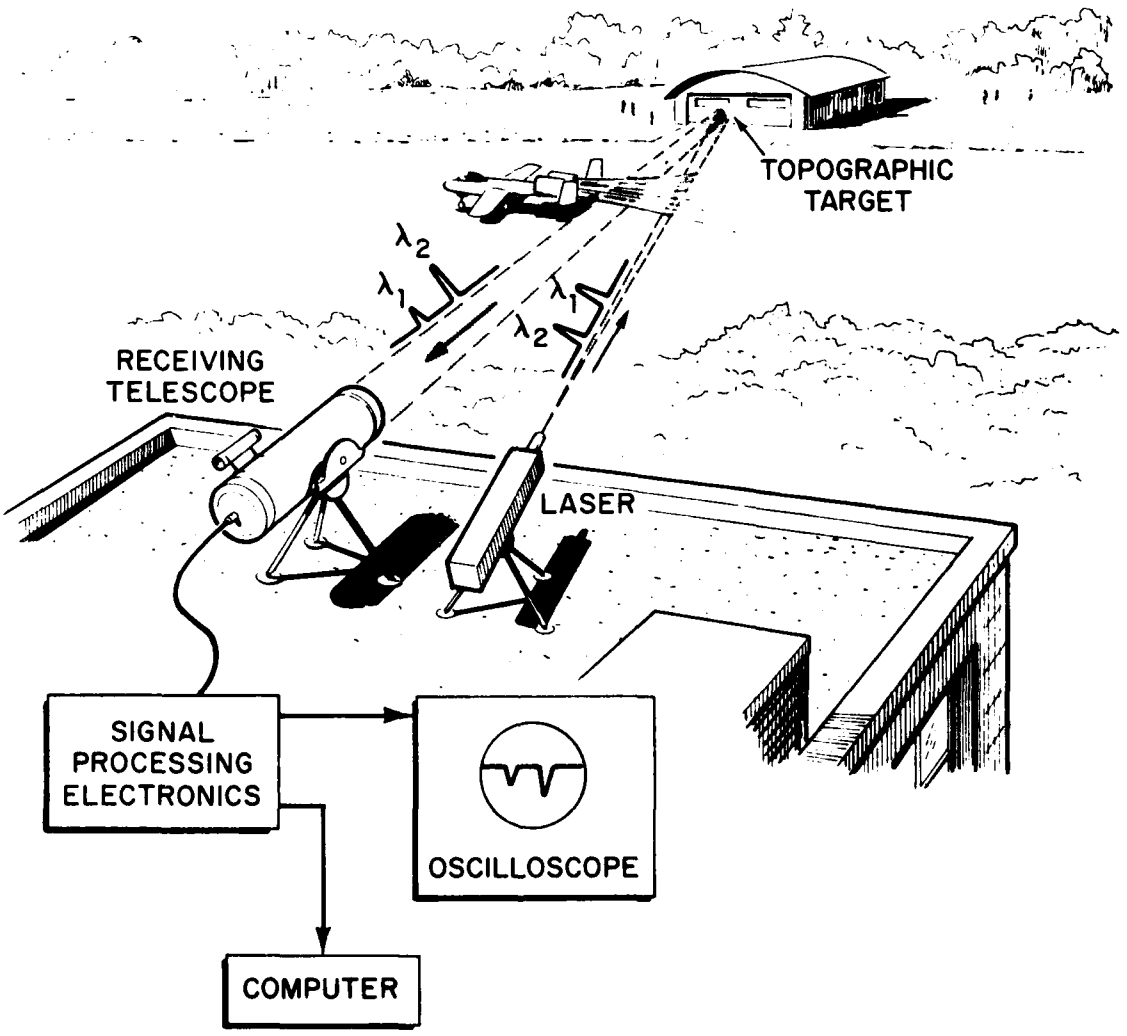

Fig. 2. Pictoral schematic of DIAL measurement of molecular effluent from A-10 aircraft.

CP95-529

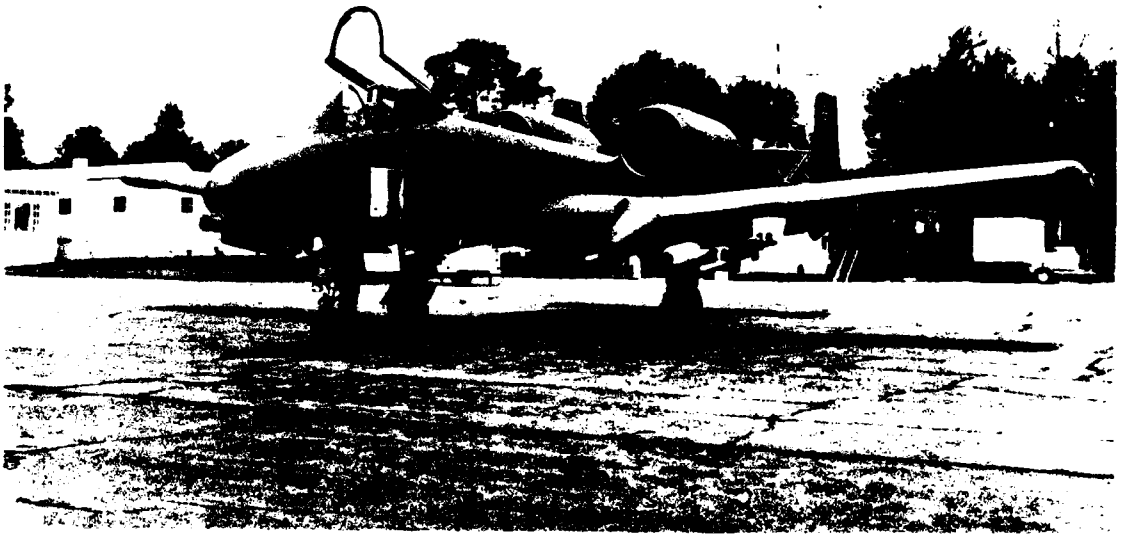

Fig. 3. Photograph of A-10 aircraft.

C82-3921

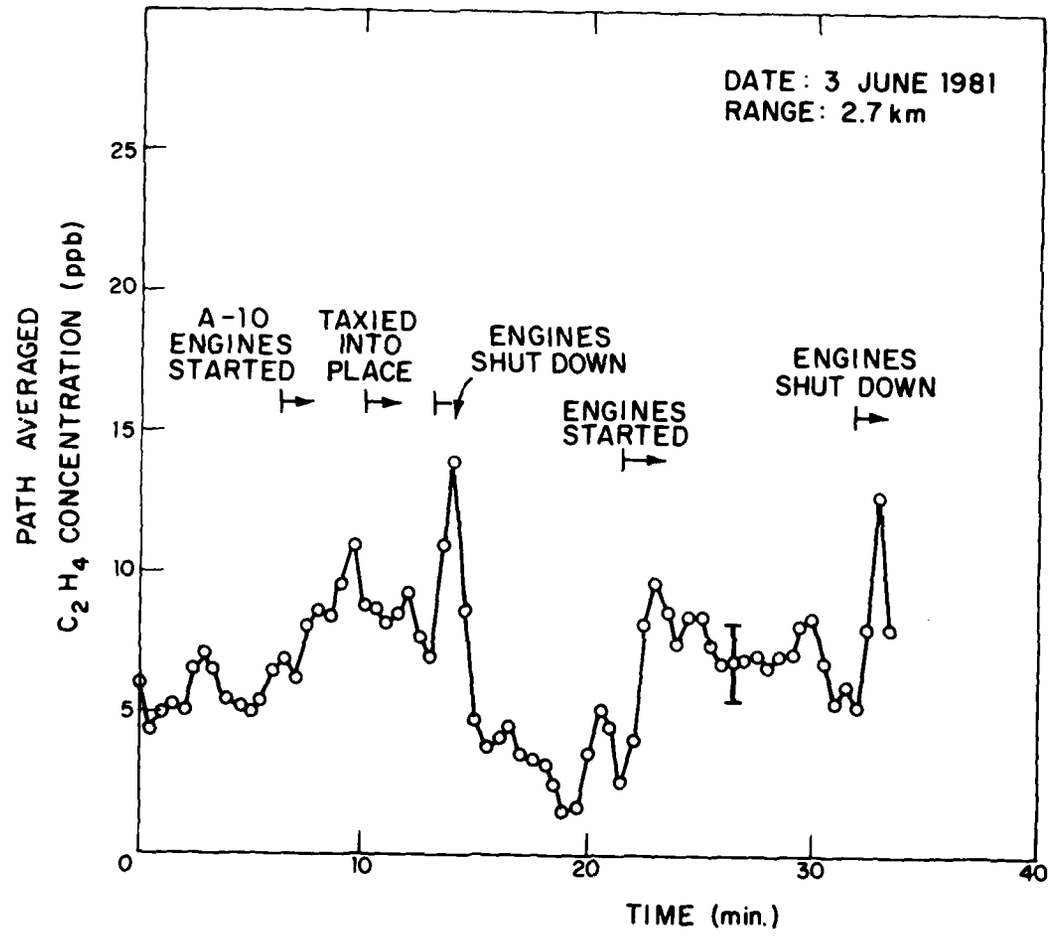

Fig. 4. Laser remote detection of C_2H_4 from the exhaust of an A-10 jet aircraft located at a range of 2.7 km.

C82-3920

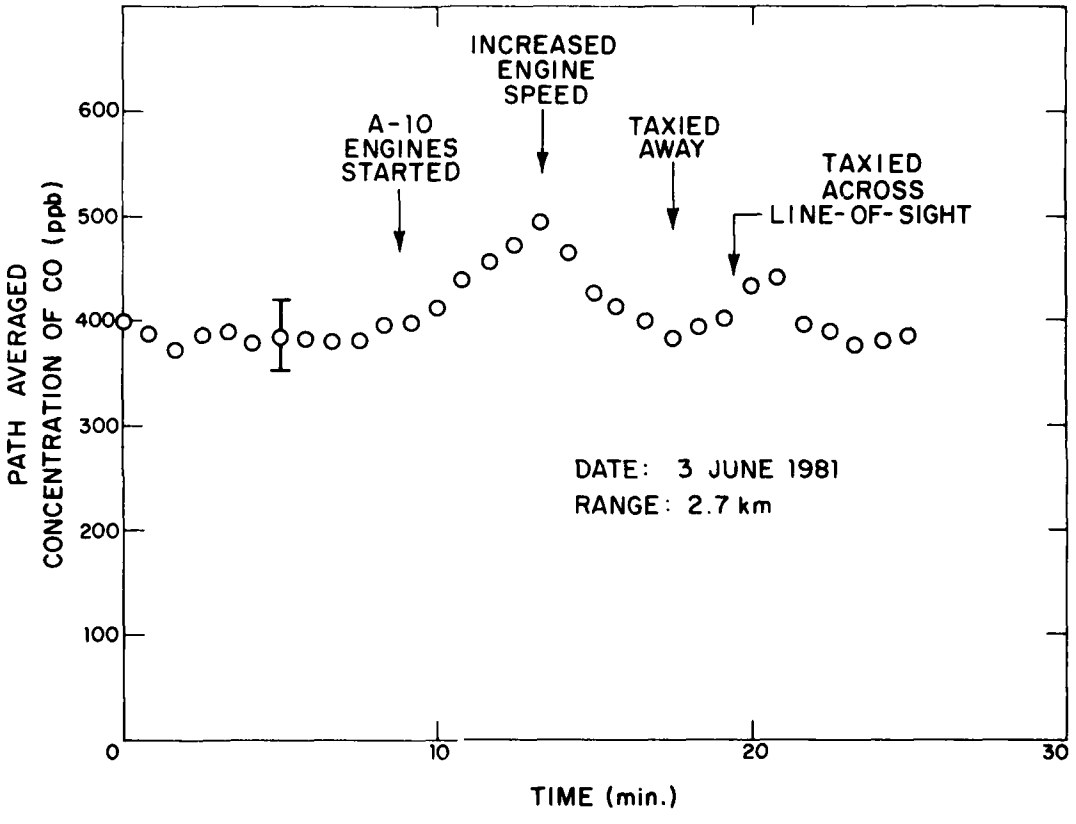

Fig. 5. Laser remote detection of CO from the exhaust of an A-10 jet aircraft located at a range of 2.7 km.

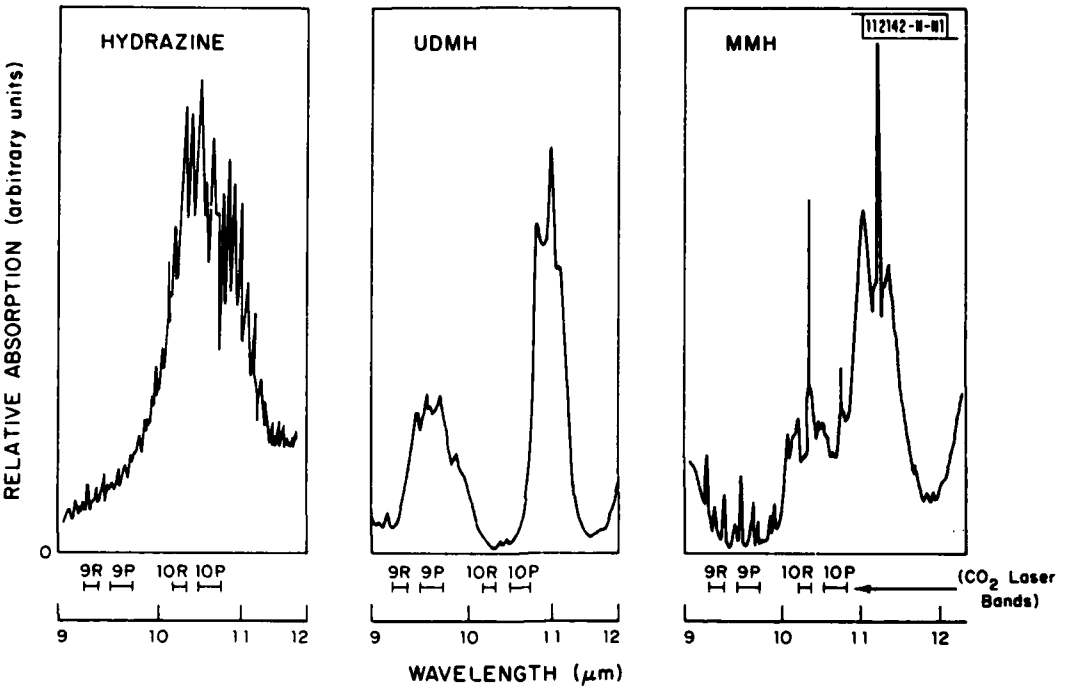

Fig. 6. Absorption spectra of hydrazine, UDMH, and MMH near the CO_2 laser transitions.

The above path-averaged results may be compared with those predicted from knowledge of the localized exhaust effluent concentration of the A-10 aircraft. The localized concentrations at idle speed from an A-10 are approximately 400 ppm-meter for CO and 15 ppm-meter for C_2H_4, with a reduction in CO concentration at faster engine settings; in addition, the cross-sectional mass concentration of the exhaust plume is fairly constant over a range of 10-20 meters behind the A-10.[3] Under these approximations, one calculates that the expected increase in the path-averaged C_2H_4 concentration over the integrated 2700 m range should have been (400 ppm-meter/2700 m) ~ 5 ppb. Similarly, the expected path-averaged increase for CO should have been approximately 150 ppb. These results are consistent with the measured increases observed in Figs. 4 and 5.

V. LASER REMOTE SENSING OF HYDRAZINE, MMH, AND UDMH

The dual-laser DIAL system has been used to test the remote sensing of hydrazine, unsymmetrical dimethylhydrazine (UDMH), and monomethylhydrazine (MMH). The detailed results of these measurements are presented in Appendix D. An overview of the most important results are presented below.

Vibrational bands of the hydrazines occur in the 9-11 μm region where the CO_2 laser operates.[4] This may be seen in Fig. 6 which shows the relative absorption of hydrazine, MMH, and UDMH as a function of wavelength along with the R and P branches of the CO_2 laser transitions near 9.6 μm and 10.6 μm. Utilizing this spectral information as well as knowledge of interfering absorbing species, CO_2 laser transitions were chosen to maximize the differential-absorption signal for remote sensing of the hydrazine compounds (see Appendix D).

The remote sensing of the toxic hydrazine compounds was accomplished using the DIAL system shown in Fig. 1 and a large, enclosed, chemically inert, polypropylene tank (104 cm long x 62.5 cm diameter with 15° slanted polypropylene windows). This tank was placed outside the laboratory window between the target and the transmitter so that the LIDAR beam passed through it. LIDAR returns were obtained using a large flat aluminum plate at a range of 2.7 km as the LIDAR target.

The differential-absorption signal was recorded for the LIDAR returns as a function of time after a known amount of the liquid hydrazine compound was injected into the tank. A similar measurement was performed using the absorption cell in the laboratory (Fig. 1).

From a comparison of the differential-absorption signal of the LIDAR returns and the absorption cell signals, the experimental sensitivity of the DIAL system was determined. It was found that the path-averaged sensitivity of the DIAL system was approximately 35 ppb, 45 ppb, and 70 ppb for hydrazine, UDMH, and MMH, respectively. This level of sensitivity was primarily due to the level of fluctuations observed for the LIDAR returns. The limits imposed on a DIAL system due to these fluctuations over long integration times are covered in detail in Appendix D. Further experimental and theoretical investigations into this limitation are currently being conducted.

VI. CONCLUSIONS AND RECOMMENDATIONS

The research described in this report has shown the capability of a dual-CO_2 laser DIAL system for the remote sensing of turbine engine exhaust gases as well as toxic hydrazine species. These experimental results have quantified the sensitivity and detection range of the dual-laser DIAL system and have indicated that the basic limitation of such remote sensing measurements is due primarily to atmospheric turbulence. In addition, these investigations have indicated the capability of the dual-laser DIAL system to eliminate the effect of atmospheric turbulence.

These results reported herein are encouraging and indicate that a dual-CO_2 laser DIAL system is able to measure several molecular and chemical species in the atmosphere at ranges up to 3 km and at concentrations in the ppb range. Further studies and experimental measurements to increase system sensitivity and selectivity are currently being conducted.

REFERENCES

1. A. Mooradian, D. K. Killinger and N. Menyuk, "Remote Sensing of Turbine Engine Gases," Final Report, Lincoln Laboratory, M.I.T., (30 September 1979), ESD-TR-79-319/ESL-TR-80-09, DTIC AD-A084544/6.

2. D. K. Killinger, N. Menyuk and A. Mooradian, "Remote Sensing of Turbine Engine Gases," Final Report, Lincoln Laboratory, M.I.T., (30 September 1980), ESD-TR-81-41/ESL-TR-81-16, DTIC AD-A099638.

3. H. Clewell, AFESC, Tyndall AFB, private comunication.

4. D. A. Stone, "Autoxidation of Hydrazine, Monomethylhydrazine and Unsymmetrical Dimethylhydrazine," in SPIE Proceedings, Vol. 289, 1981 International Conference on Fourier Transform Infrared Spectroscopy, H. Sakai, Editor (1981), p. 45.

APPENDIX A

The following is a reprint of a journal article published in Applied Physics Letters, 15 June 1981, entitled "Effect of Turbulence-Induced Correlation on Laser Remote Sensing Errors."

Effect of turbulence-induced correlation on laser remote sensing errors

D. K. Killinger and N. Menyuk
Lincoln Laboratory, Massachusetts Institute of Technology, Lexington, Massachusetts 02173

(Received 2 March 1981; accepted for publication 31 March 1981)

Using a 10.6-μm dual-laser differential-absorption laser remote sensing system, we have measured the short- and long-term temporal correlation of the returns from topographic targets and retroreflectors in order to investigate the effect of atmospheric turbulence on laser remote sensing measurement errors. Our results quantify the improvement obtained through use of a dual-laser system compared to that of a single-laser system and are in good agreement with those predicted by a theory which considers the effect of partial temporal correlation on the resultant measurement error.

PACS numbers: 42.68.Rp, 42.10.Qj

Several studies[1-3] have shown that atmospheric turbulence can greatly influence the accuracy of laser remote sensing measurements through temporal changes in the atmospheric absorption characteristics. However, little experimental work has been conducted in order to quantify such effects, particularly in the case of differential-absorption LIDAR (DIAL) measurements.

In this letter, we report the results of experiments using a pulsed, tunable dual-CO_2 laser DIAL system to measure the short- and long-term temporal correlation of the laser returns and the effect of these temporal correlations on the overall measurement error. From measurements of the statistical and temporal properties of the returns from several different topographic targets and retroreflectors, we have determined the accuracy of these laser remote sensing measurements and quantified the relative improvement obtainable by use of a dual-laser system compared to that of a single-laser system. This improvement was found to be in good agreement with that predicted by a theory which considers the effect of nonzero temporal cross-correlation terms on the statistical propagation of errors in the DIAL equation; this theory is an outgrowth of previous work by Schotland[4] and Kjelaas *et al.*[5] These results are important since they experimentally quantify the role that atmospheric turbulence plays in the determination of errors in laser remote sensing measurements and the role that temporal correlation plays in effecting an overall increase in measurement accuracy through the use of signal-averaging techniques.

Our experiments were conducted using a system similar to that reported previously.[6,7] The system basically consists of two individually triggered mini-TEA CO_2 lasers[8] coupled by means of a 50% beamsplitter to a common LIDAR (laser radar) optical system containing a $\times 10$ beam expander, beam steering mirror, 30-cm Cassegrain telescope, and HgCdTe detector; this direct detection LIDAR system had a laser beam divergence of 0.4 mrad and a receiver field of view of 1.1 mrad. The laser energy per pulse was 10 mJ with a pulse length of 100 ns. The time separation of the two lasers was set at 35 μs, which provided temporal separation between the two LIDAR returns. Through the use of beamsplitters, an absorption cell, and fast pyroelectric detectors, the energy and frequency of each laser pulse was monitored to provide normalization and calibration data on a pulse to pulse basis.

The LIDAR returns were obtained from several topographic targets and retroreflectors at ranges up to 2.7 km and typically had a signal to noise ratio on the order of 10 or more. Using high-speed analog-2-digital converters and appropriate gating electronics, the returns were recorded for periods up to 10 min using a dual-computer digital data acquisition system. The collected LIDAR returns were normalized to the energy in each laser pulse, compared to predetermined thresholds to eliminate laser misfires ($< 1\%$), analyzed for statistical parameters (mean, standard deviation, log normal variance, temporal correlation, and frequency power spectrum), and displayed graphically in real time on the computer. For this analysis, both lasers operated on the 10.611-μm $P(22)$ line. Similar results have been obtained using other CO_2 laser transitions.

Figure 1 shows a typical graphical display of the time history of dual-laser LIDAR returns obtained from a small retroreflector at a range of 2.7 km with the lasers operating at a 10-Hz pulse repetition frequency. As seen in Fig. 1, the two returns are highly correlated on a short-term (35 μs) basis and partially correlated for longer times (> 50 ms). These results are indicative of the various temporal and spatial scales of the perturbations induced on the propagated laser radiation by the effects of atmospheric turbulence.

It has recently been shown by Kjelaas *et al.*,[5] using a cw laser absorption spectrometer, that one may exploit such correlations in the two laser beams to reduce the overall

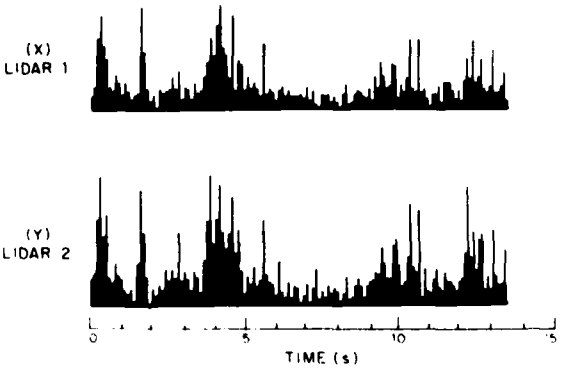

FIG. 1. Graphical display of the normalized intensity of the pulsed LIDAR returns from a retroreflector (range 2.7 km) as a function of time; upper plot (X) is for LIDAR 1 and lower plot (Y) is for LIDAR 2.

 0003-6951/81/120968-03$00.50

measurement error. We have expanded these studies to encompass two-way measurements applicable to differential-absorption LIDAR.

Figure 2 shows some experimental results of the measured standard deviation (normalized to the mean) of the LIDAR returns as a function of the number of returns integrated; the PRF of the lasers was 5.4 Hz. Results are given for two targets, a 1-in. retroreflector and the side of a large painted metal building, both located at a range of 2.7 km. The data was obtained by recording the LIDAR returns for a 10-min period and later performing an integrated moving average of the data; the standard deviation presented in Fig. 2 is the standard deviation of this "moving window" average for N pulses contained within the "window." Results are shown in Fig. 2 for both the individual LIDAR returns, X and Y, and that obtained by dividing the return values on a pulse-pair basis, (X_i/Y_i), where i refers to the ith return. The standard deviations obtained for X were approximately the same as those obtained for Y, so that, for simplicity, only the rms average of these two values is shown in Fig. 2.

The data shown in Fig. 2 supports several conclusions. These are (i) the measurement error (standard deviation) decreases as the number of pulses integrated N is increased, (ii) the measurement error for the dual-laser data (X_i/Y_i) is substantially less than that for each individual LIDAR signal, and (iii) the decrease in measurement error shows departures from the expected $\sqrt{N}$ behavior as N becomes large; the $\sqrt{N}$ behavior is expected, since the variance of the mean value of a distribution σ_m^2 is related approximately to the variance of the ensemble distribution σ^2 as $\sigma_m^2 = \sigma^2/N$. These points may be better understood from consideration of the cross correlation of the returns.

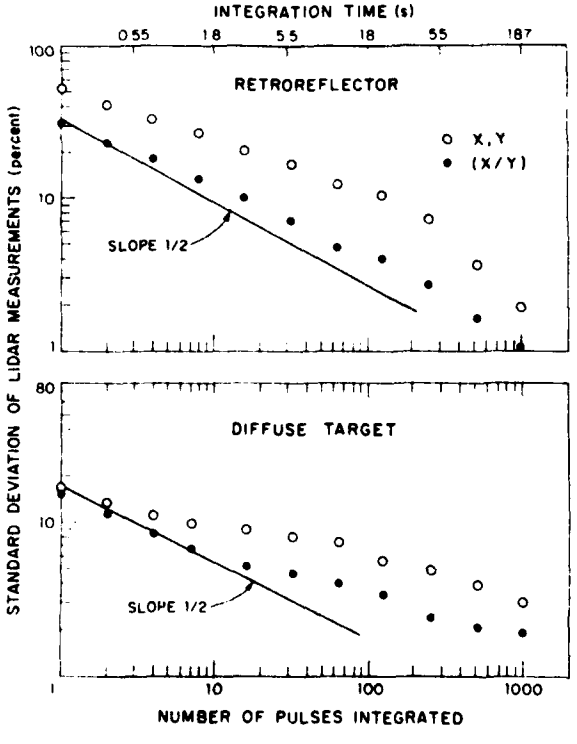

FIG. 2. Measured standard deviation of single- and dual-laser LIDAR returns as a function of the number of pulses integrated; X, Y refer to single-laser returns, and (X/Y) refers to the ratio of the dual-laser pulse-pair returns (X_i/Y_i).

The cross-correlation coefficient $\rho_{\Delta t}$ may be defined[9] as

$$\rho_{\Delta t} = \frac{\langle (X_i - \bar{X})(Y_i - \bar{Y})\rangle}{[\langle (X_i - \bar{X})^2\rangle \langle (Y_i - \bar{Y})^2\rangle]^{1/2}} = \frac{\sigma_{xy}}{\sigma_x \sigma_y}, \quad (1)$$

where X_i and Y_i are the normalized individual LIDAR returns of the ith pulse, $\bar{X} = \langle X_i \rangle$ is the ensemble average of X, σ_x and σ_y are the standard deviation of these returns, $\Delta t = 35\,\mu$s and is the pulse separation time between the X_i LIDAR pulse and the Y_i LIDAR pulse, and σ_{xy} is the covariance of the returns. As seen in Eq. (1), $\rho_{\Delta t}$ represents the fraction of the total statistical fluctuations which are correlated.

Equation (1) was used to determine the correlation coefficient $\rho_{\Delta t}$ of the dual-laser LIDAR returns using the same data as was used in Fig. 2. For $\Delta t = 35\,\mu$s, the measured correlation coefficient values were $\rho_{\Delta t} = 0.868$ for the retroreflector data and $\rho_{\Delta t} = 0.593$ for the diffuse (optically rough) target. These values are similar to those obtained from a more general study of $\rho_{\Delta t}$ as a function of Δt given elsewhere.[10]

The concentration of an absorbing specie determined from a DIAL measurement is related to $\ln(X/Y)$. The determination of $\ln(X/Y)$ may be made from sequential measurements of a single-laser DIAL system as $\ln(\langle X_i \rangle / \langle Y_j \rangle)$ or from dual-laser DIAL measurements which exploit the temporal correlation of the two returns on a pulse-pair basis as $\ln(\langle X_i/Y_i \rangle)$. To relate the measurement error of these two processes, one may consider the statistical propagation of error[11] in a general function $g = f(Z_1, Z_2, \ldots)$ to first order approximately as

$$\sigma_g^2 \simeq \sum_{l,k=1}^{n} \left(\frac{\partial f}{\partial Z_l}\bigg|_0\right)\left(\frac{\partial f}{\partial Z_k}\bigg|_0\right)\sigma_{z_l z_k}, \quad (2)$$

where the derivatives are evaluated at $\bar{Z}_l$ and $\bar{Z}_k$. Equations (1) and (2) may be used to obtain the normalized variance of the dual-laser DIAL measurements $\sigma_{\ln}^2(\xi) = \sigma_\xi^2/(\bar{\xi})^2$, as

$$\frac{\sigma_\xi^2}{(\bar{\xi})^2} = \frac{\sigma_x^2}{(\bar{X})^2} + \frac{\sigma_y^2}{(\bar{Y})^2} - 2\rho_{\Delta t}\frac{\sigma_x \sigma_y}{\bar{X}\bar{Y}}, \quad (3)$$

where $\xi \equiv X_i/Y_i$ and $\sigma_{xx} \equiv \sigma_x^2$. Equation (3) may be simplified under the conditions that $\sigma_x = \sigma_y \equiv \sigma$ and $\bar{\xi} = \bar{X} = \bar{Y} = 1$ as

$$\sigma_\xi^2 = 2\sigma^2(1 - \rho_{\Delta t}). \quad (4)$$

As seen in Eqs. (3) and (4), the effect of a nonzero temporal correlation is to reduce the dual-laser measurement error. It should be noted that the effect of signal averaging N pulses over a time period T is to operate with $(1/N)\Sigma$ [or $(1/T)\int dt$] on Eq. (3). The resultant measurement error is, thus, directly dependent upon any nonstationary terms in Eq. (3).

Our experimental results shown in Fig. 2 may be understood in light of the arguments presented above. Using the measured value of the correlation coefficient, $\rho_{\Delta t} = 0.868$ and 0.593, and the values from Fig. 2 of $(\sigma_x/\bar{X}) \simeq (\sigma_y/\bar{Y}) = 0.545$ and 0.164, Eq. (3) yields values of $(\sigma_\xi/\bar{\xi}) = 0.28$

and 0.147 for the retroflector and diffuse target, respectively. These values are in good agreement with the measured values for $(\sigma_\xi/\bar{\xi})$ of 0.31 and 0.15 shown in Fig. 2. In addition, the observed deviations from the expected square-root dependence of σ versus N in Fig. 2 are due to nonstationary terms in Eqs. (1) and (3), including $\bar{X}$, σ_x, and thus $\rho_{\Delta t}$.[10] These deviations exemplify the role that long-term temporal changes in the atmosphere have on the signal averaged DIAL measurement error obtained from the time integral of Eq. (3) and are indicative of nonergodic processes (i.e., the ensemble average is not equal to the time average).

Atmospheric turbulence can induce short-term adiabatic[1,2] perturbations on the LIDAR returns through several mechanisms including beam wander, angle-of-arrival, and interference effects. In addition, longer-term perturbations may also be present due to gross changes in the atmospheric absorption background associated with nonstationary localized concentrations of absorbing species. These different perturbations will affect the return signals in different analytical ways. This may be seen qualitatively through use of the familiar LIDAR equation by expressing the return from laser 1 as

$$X = Ae^{-\alpha}, \tag{5}$$

and that from laser 2 as

$$Y = Be^{-\beta}, \tag{6}$$

where A and B are constants appropriate to the DIAL system, encompassing range, target reflectively, aperture, and beam pointing effects; α and β are associated with the absorption characteristics of the propagation path. Equation (2) may be used with Eqs. (5) and (6) to yield

$$\frac{\sigma_\xi^2}{(\bar{\xi})^2} \cong \frac{\sigma_x^2}{(\bar{X})^2} + \frac{\sigma_y^2}{(\bar{Y})^2} - 2\frac{\sigma_{AB}}{\bar{A}\bar{B}} - 2\sigma_{\alpha\beta}. \tag{7}$$

Equation (7) is valid for the case where higher order terms as well as $\sigma_{A\beta}$ and $\sigma_{B\alpha}$ are negligible. Comparison of Eq. (3) and Eq. (7) indicates that turbulence-induced cross correlation can arise both from linear terms (A,B) and the exponential terms (α,β) in Eqs. (5) and (6); σ_{AB} is associated with geometrical effects, while $\sigma_{\alpha\beta}$ is associated with changes in the atmospheric attenuation. It should be noted that Eqs. (2), (3), and (7) are approximations valid under several simplifying conditions and should be modified in the more general case to include a more rigorous treatment of the propagation of the covariance terms for nonidentical or non-Gaussian distributions.

This work was sponsored by the National Aeronautical and Space Administration and the Air Force Engineering and Services Center.

[1] R. S. Lawrence and J. W. Strohbehn, Proc. IEEE 58, 1523 (1970).
[2] R. L. Fante, Proc. IEEE 63, 1669 (1975).
[3] S. F. Clifford, Opt. Quantum Electron 8, 95 (1976).
[4] R. M. Schotland, J. Appl. Meteor. 13, 71 (1974).
[5] A. G. Kjelaas, P. E. Nordal, and A. Bjerkestrand, Appl. Opt. 17, 277 (1978).
[6] D. K. Killinger, N. Menyuk, and W. E. DeFeo, Appl. Phys. Lett. 36, 402 (1980).
[7] N. Menyuk, D. K. Killinger, and W. E. DeFeo, Appl. Opt. 19, 3282 (1980).
[8] N. Menyuk and P. F. Moulton, Rev. Sci. Instrum. 51, 216 (1980).
[9] G. E. P. Box and G. M. Jenkins, *Time Series Analysis* (Holden-Day, San Fransisco, 1976).
[10] N. Menyuk and D. K. Killinger, Opt. Lett. (to be published).
[11] 1975].
[12] A. Ishimaru in *Laser Beam Propagation in the Atmosphere*, edited by J. W. Strohbehn (Springer, Berlin, 1978), p. 157.

APPENDIX B

The following is a reprint of a journal article published in Optics Letters, June 1981, entitled "Temporal Correlation Measurements of Pulsed Dual CO_2 LIDAR Returns."

Temporal correlation measurements of pulsed dual CO_2 lidar returns

N. Menyuk and D. K. Killinger

Lincoln Laboratory, Massachusetts Institute of Technology, Lexington, Massachusetts 02173

Received February 5, 1981

The temporal correlation and statistical properties of backscattered returns from specular and diffuse topographic targets have been measured by using a pulsed dual-laser direct-detection lidar system operating near 10.6 μm. Our results show that atmospheric-turbulence fluctuations can effectively be frozen for pulse separation times of the order of 1–3 msec or less. However, only incomplete correlation was achieved; the diffuse target returns yielded much lower correlation than that obtained with the specular targets. This is shown to be due to uncorrelated system noise effects and different statistics for the two types of target returns.

The use of differential-absorption lidar (DIAL) techniques has long been recognized as one of the most sensitive means for the long-range remote sensing of atmospheric pollutants.[1-3] At present, most DIAL systems used for pollution detection employ a single laser that measures, in turn, the atmospheric absorption at the off-resonance and on-resonance frequencies of the pollutant being investigated. In grating-tuned pulsed-laser systems, it is common to operate at one frequency for several pulses[4,5] before moving the grating to the second frequency. The delay between absorption measurements at the on-resonance and off-resonance frequencies under these conditions varies from several seconds to a few minutes. Such delay times are very long relative to temporal fluctuations that are due to atmospheric turbulence effects. It is important that these temporal fluctuations be experimentally quantified as they directly influence the associated accuracy of any DIAL measurement.

In this Letter we report the results of a study of the temporal correlation and statistical properties of backscattered returns from both specular and diffuse (optically rough) topographic targets using a dual-laser DIAL system. Our results indicate that the atmosphere is essentially "frozen" for times of the order of 1–3 msec; these results are consistent with those obtained previously by Ku *et al.*[6] and by Marthinsson *et al.*[7] using a diode and cw CO_2 lasers, respectively, and retroreflector targets. However, by using topographic targets as well as a retroreflector, we have found that the nature of the target can significantly affect the observed correlation during this time and thus effectively reduce the expected improvement in measurement accuracy attainable through the use of a dual-laser DIAL system relative to a single-laser system.

Our measurements were carried out with the dual-laser direct-detection differential-absorption lidar system shown schematically in Fig. 1 and is similar to the single-laser system reported previously.[5,8]

Pulsed line-tunable mini-TEA CO_2 lasers[9] were used to provide the transmitted radiation. The pulse delay between the firing of the two lasers can be varied from about 3 μsec to greater than 200 msec. The beams from the two lasers were positioned to lie along a common path through use of a beam splitter. Portions of each beam were directed to a pyroelectric detector, which served to normalize the output of each pulse. Another portion of the beam was directed through an absorption cell to a second pyroelectric detector, which, for this experiment, was evacuated and used only as a laboratory check of the system operation. The major part of the radiation from the lasers was sent through a 10× beam expander to a beam-steering mirror and directed toward topographic targets outside our laboratory window at ranges up to 2.65 km. The radiation backscattered from the target was detected by a 30-cm Cassegrain telescope and a HgCdTe detector. The outputs of the three detectors were digitized in separately gated analog-to-digital converters and sent to the system data-acquisition computer, where the lidar signal returns were normalized to the laser power on a pulse-to-pulse basis. The correlation coefficients are computed from the average of several hundred pulse pairs.

The correlation coefficient ρ may be given as

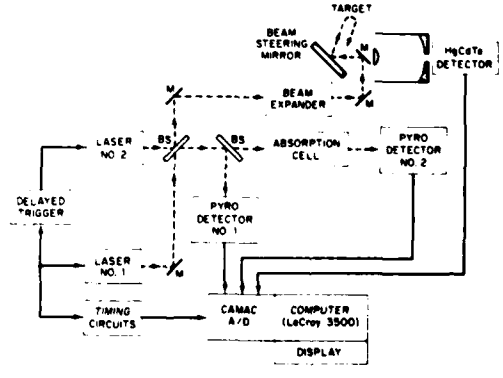

Fig. 1. Schematic of dual-laser DIAL system used for temporal correlation measurements.

Reprinted from **Optics Letters**, Vol. 6, page 301, June 1981

$$\rho(x,y) = \frac{\langle (x_i - \bar{x})\,(y_i - \bar{y})\rangle}{[\langle (x_i - \bar{x})^2\rangle\ \langle (y_i - \bar{y})^2\rangle]^{1/2}} = \frac{\sigma_{xy}}{\sigma_x \sigma_y}, \quad (1)$$

where x_i and y_i are the normalized lidar returns of the ith pulse of the leading laser and delayed laser, respectively, σ_x and σ_y are the standard deviations of the normalized lidar returns from the respective lasers; and σ_{xy} is the covariance of the returns. The angle brackets correspond to ensemble averages.

Equation (1) was also used to compute the correlation coefficient for the normalized absorption-cell signal from pyroelectric detector no. 2 in Fig. 1. In this case, with no atmospheric-turbulence effects to cause correlated deviations from the average return, the only deviation from the average arises from system noise, which should be uncorrelated. We found the correlation coefficient to be negligible, which served to check that the system electronics was not inadvertently introducing a spurious correlation.

Figure 2 shows the results of our measurements of the temporal cross-correlation coefficient of the normalized lidar returns as a function of the separation time between the two laser pulses. Each point corresponds to an average over a minimum of 500 pulse pairs and was obtained with both lasers operating on the 10.6-μm $P(24)$ line at a pulsed repetition frequency of 15 Hz. The values shown were obtained from a retroreflector at a range of 2.65 km, from a specular target consisting of small metallic light fixtures atop a pole 2 km distant, and from the side of a large building 1.5 km away, which served as an extended diffuse target. The measured correlation coefficients are seen to be essentially constant for delay times up to about 1–3 msec and then to decrease with further increases in delay time. By 100-msec delay, the correlation coefficient has been reduced to the order of ~0.1–0.2. The observed decorrelation time of 1–3 msec is in general accord with previous results.[6,7]

As expected, the specular target and retroreflector yielded high pulse-pair correlation at short pulse-delay times. However, the correlation measured for the diffuse target is seen to be limited to a value of approximately 0.5. This limitation was found to apply to several other diffuse targets investigated.

To understand the results presented in Fig. 2, consideration must be given to the differences inherent in

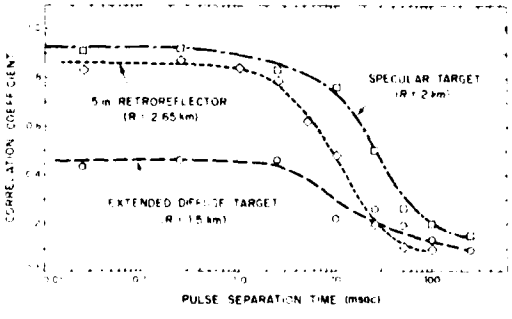

Fig. 2. Correlation coefficient versus pulse separation time for backscattered CO_2 laser $P(24)$ radiation at 10.632 μm from a 12.7-cm retroreflector, a specular target, and an extended diffuse target at the ranges shown.

the backscattered radiation reflected from the different targets. The retroreflector and the light fixture are specular targets, and glint (directional reflectance) forms their major reflective component, whereas the building is optically rough, and speckle (interference effects) plays a more dominant role.[10,11]

In our DIAL system the detection field of view (1.1 mrad) encompasses almost three times the diameter of the laser beam (0.4 mrad). For the extended diffuse target this field of view is large enough to encompass the entire beam area at the target, even after including anticipated spot movement that is due to turbulence-induced, and hence correlated, beam wander.[12] Deviations of the return signal from the mean value that are due to the correlated beam-wander effect are therefore minimized. Furthermore, under these conditions, the detected signal amplitude represents the return from the entire beam and hence averages out strong local fluctuations. This aperture-averaging effect[10,13] effectively reduces the magnitude of these fluctuations, which can be due to turbulence-induced laser-beam scintillation,[14] diffraction-caused nodal patterns,[15] or speckle effects at the target.[11] The overall effect of diffuse scattering and aperture averaging should therefore be to reduce the deviation of the individual pulses from the mean. Furthermore, possible frequency differences between the outputs of the two lasers operating on the same transition line are relatively small ($\Delta\nu/\nu \lesssim 10^{-5}$) and should not lead to the lowered correlation observed for the diffuse target.[16,17]

The specular targets are subject to different aperture-averaging effects, being much smaller than the laser beam at the target range. They are also subject to turbulence-induced angle-of-arrival effects.[18] Under the conditions of our experiments, the backscattered signals from the specular targets should exhibit a much greater variation than the signal return from the diffuse target.[10]

In order to investigate these effects directly, histograms of the backscattered lidar returns from all three targets were obtained. The results are shown in Fig. 3. Each histogram involves 2000 pulses and gives the number of returns at each relative intensity level. The returns from the retroreflector and specular target are seen to have a large statistical spread, with standard deviations of about 80 and 60%, respectively, and an almost log-normal distribution. However, the standard deviation of the diffuse target is much smaller, approximately 20%, and is seen to have a statistical distribution more closely approximating a normal distribution. These results are consistent with the arguments presented above and with calculations that consider aperture-averaging effects on lidar returns from specular and rough targets.[10,11]

The standard deviations of the lidar returns shown in Fig. 3 may be compared with those measured by using the normalized signal from pyroelectric detector no. 2. This value was found to be about 6%, with a correlation coefficient of zero. This 6% value represents the normalization capability of our DIAL system and is attributable to electronic and optical effects within our laboratory. Such variation will also be present in all the lidar returns, which will also contain additional uncor-

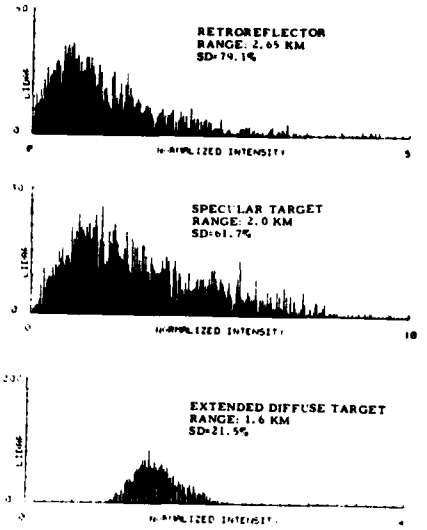

Fig. 3. Histograms of lidar returns from a 12.7-cm retroreflector, a specular target, and an extended diffuse target. Each histogram represents the backscattered return from 2000 laser pulses and was obtained from the computer display.

related or noise signals that are due to pulse-to-pulse variations of the individual laser outputs in the form of changes of mode quality or small directional shifts in the laser beam.

This uncorrelated signal variation represents a small percentage of the standard deviations observed in the backscattered returns from the specular targets, but it is a significant fraction of the standard deviation of the diffuse target return. The combination of these noise effects, coupled to the relatively small variance of the backscattered lidar return, is apparently sufficient to limit the correlation coefficient obtainable with an extended diffuse target. It should also be noted that since a topographic target such as the side of a building will not, in general, be perfectly diffuse, a significant part of the observed correlation may be due to glint from a small specular component of the target.

If the above arguments are valid, the departure from unity in the measured correlation coefficients for all the targets should be explicable on the basis of a constant uncorrelated term forming a part of the lidar returns. To establish quantitatively if this is consistent with our correlation data (Fig. 2), the uncorrelated term may be introduced explicitly into Eq. (1) under certain simplifying assumptions. Specifically, the standard deviation of the lidar returns from both lasers are assumed equal, $\sigma_x = \sigma_y = \sigma$, and we express the measured variance, σ^2, as the sum of a correlated and an uncorrelated contribution; i.e., $\sigma^2 = \sigma_c^2 + \sigma_u^2$. Then $\sigma_{xy} = \sigma_c^2$; note that the uncorrelated component of σ_{xy} is identically zero. For this case, Eq. (1) simplifies to the form

$$\rho = \sigma_c^2/(\sigma_c^2 + \sigma_u^2) = 1 - (\sigma_u/\sigma)^2. \qquad (2)$$

As is seen in Eq. (2), the effect of an uncorrelated noise component is to reduce the measured correlation coefficient. It should be noted that the correlated component, σ_c, is due to temporal correlations imposed on the lidar beam by atmospheric turbulence.

Within the framework of the above assumptions we can use the experimental values of ρ and σ of the diffuse target in conjunction with Eq. (2) to establish a value of σ_u. Taking $\rho = 0.46$ and $\sigma = 0.215$, as given in Figs. 2 and 3, respectively, Eq. (2) yields $\sigma_u = 0.16$. When this value of σ_u and the measured values $\sigma = 0.79$ and 0.62 obtained with the retroreflector and light fixture are used, Eq. (2) yields $\rho = 0.96$ and 0.93, respectively. These may be compared with the experimental values, $\rho = 0.87$ and 0.92. Considering the measurement variability in the experimental values of σ and ρ over different time intervals, the agreement shown is reasonable and, most importantly, indicates that the departure of the observed correlation coefficient from unity is directly related to the relative strength of the uncorrelated variance, $(\sigma_u/\sigma)^2$.

In conclusion, we have found that time delays between pulses of the order of 1–3 msec or less are needed to freeze out the effects of atmospheric turbulence. However, the level of achievable correlation has been found to be strongly target dependent and is ultimately limited by the relative uncorrelated optical and electronic noise effects, σ_u/σ, of the overall DIAL system.

This research was sponsored by the National Aeronautics and Space Administration and the U.S. Department of the Air Force, in part with specific funding from the Air Force Engineering and Services Center.

References

1. H. Kildal and R. L. Byer, Proc. IEEE **59**, 1644–1663 (1971).
2. R. M. Measures and G. Pilon, Opto-electronics **4**, 141–153 (1972).
3. R. L. Byer and M. Garbuny, Appl. Opt. **12**, 1496–1505 (1973).
4. E. R. Murray and J. E. van der Laan, Appl. Opt. **17**, 814–817 (1978).
5. D. K. Killinger, N. Menyuk, and W. E. DeFeo, Appl. Phys. Lett. **36**, 402–405 (1980).
6. R. T. Ku, E. D. Hinkley, and J. O. Sample, Appl. Opt. **14**, 854–861 (1975).
7. B. Marthinsson, J. Johansson, and S. T. Eng, Opt. Quantum Electron. **12**, 327–334 (1980).
8. N. Menyuk, D. K. Killinger, and W. E. DeFeo, Appl. Opt. **19**, 3282–3286 (1980).
9. N. Menyuk and P. F. Moulton, Rev. Sci. Instrum. **51**, 216–220 (1980).
10. J. H. Shapiro, Project Reps. TST-24 (DDC AD-A063767) and TST-27 (DDC AD-A065627) (Lincoln Laboratory, Massachusetts Institute of Technology, Lexington, Mass., 1978).
11. J. W. Goodman, Proc. IEEE **53**, 1688–1700 (1965).
12. T. Chiba, Appl. Opt. **10**, 2456–2461 (1971).
13. J. R. Kerr and J. R. Dunphy, J. Opt. Soc. Am. **63**, 1–8 (1973).
14. P. H. Dietz and N. J. Wright, J. Opt. Soc. Am. **59**, 527–535 (1969).
15. M. Born and E. Wolf, *Principles of Optics* (Pergamon, Oxford, 1975), pp. 382 *et seq*.
16. S. T. Hong and A. Ishimaru, Radio Sci. **11**, 551–559 (1976).
17. A. G. Kjelaas, P. E. Nordal, and A. Bjerkestrand, Appl. Opt. **17**, 277–284 (1978).
18. R. F. Lutomirski and R. E. Warren, Appl. Opt. **14**, 840–846 (1975).

APPENDIX C

The following is a reprint of a journal article published in IEEE Journal of Quantum Electronics, September 1981, entitled "Remote Probing of the Atmosphere Using a CO_2 DIAL System."

Remote Probing of the Atmosphere Using a CO_2 DIAL System

DENNIS K. KILLINGER AND NORMAN MENYUK

(*Invited Paper*)

Abstract - An overview of our laser remote sensing effort is presented. Using both fundamental and frequency-doubled CO_2 laser radiation in a differential absorption LIDAR (DIAL) system, background concentrations of CO, NO, and C_2H_4 in the atmosphere as well as increases due to localized emission sources have been measured. These species have been detected using the backscattered laser radiation from topographic targets at ranges to 2.7 km with a sensitivity of ±10 ppb. In addition, using a dual-laser DIAL system, the effect of induced correlation of the LIDAR returns due to atmospheric turbulence has been investigated. These results have been used to help quantify the accuracy of the DIAL measurements and are shown to be consistent with theory.

Manuscript received April 20, 1981. This work was supported by the National Aeronautics and Space Administration and the Department of the Air Force, in part by the Air Force Engineering and Services Center and the Air Force Office of Scientific Research.

The authors are with the Lincoln Laboratory, Massachusetts Institute of Technology, Lexington, MA 02173.

I. INTRODUCTION

LASER remote sensing has been shown to be a useful probe of the concentration, temperature, pressure, and velocity of molecular constituents in the atmosphere. Several different laser remote sensing techniques have been developed and they include differential absorption LIDAR (DIAL) [1], Raman scattering [2], and laser induced fluorescence [3], [4]. Studies have indicated that, of these techniques, infrared DIAL offers several advantages [5]. These include 1) a high degree of sensitivity per laser probe energy, 2) a wide variety of molecules which exhibit absorption characteristics in the infrared, and 3) the high relative degree of eye safety provided by lasers operating in the infrared compared to the visible and UV region.

0018-9197/81/0900-1917$00.75

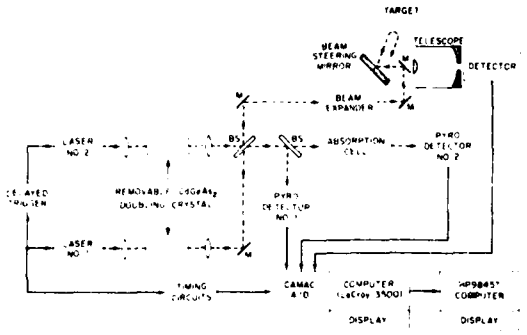

Fig. 1. Schematic of dual-laser DIAL system.

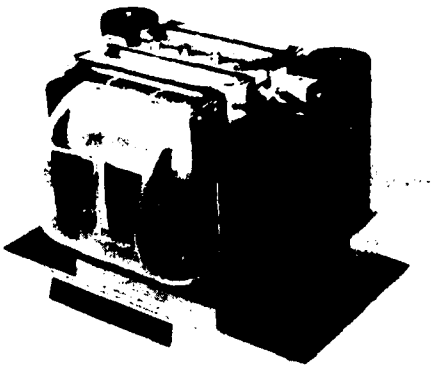

Fig. 2. Photograph of mini-TEA CO_2 laser.

Our research in the laser remote sensing field has been directed toward the development of new laser sources in the infrared spectral region and their use in a DIAL system to demonstrate both their capabilities and limitations for the remote sensing of molecular species in the atmosphere. This program has included the development of a direct-detection differential absorption LIDAR system incorporating a pulsed high-repetition-rate mini-TEA (transverse excited atmosphere) CO_2 laser as the primary radiation source. This laser can be used with or without frequency-doubling $CdGeAs_2$ crystals to provide line-tunable coherent radiation in both the 5 and 10 μm wavelength regions of the infrared. Frequency-doubled radiation near 5 μm has been used for the detection of CO and NO in the atmosphere, while radiation near 10.6 μm has been used to detect C_2H_4. Measurements have been made with the mini-TEA lasers used in both single- and dual-laser DIAL systems, and a study has been made of the improvement in the measurement error achievable with the dual-laser system. This research has led to a better understanding of the role that atmospheric turbulence plays in determining DIAL measurement errors.

This paper is an overview of our laser remote sensing effort. Some of the subjects discussed have been reported previously [6]-[9]; however, many additional results and salient details omitted in previous reports are given here and the overall scope of the research is presented for the first time.

A detailed description of the experimental systems used for our measurements is given in Section II, followed in Section III by a brief discussion of the theory needed for remote sensing of molecular constituents in the atmosphere with a DIAL system. The results of experimental measurements made for the remote sensing of C_2H_4, CO, and NO in the atmosphere are given in Section IV. Finally, a discussion and analysis of DIAL measurement errors, involving a comparison of the relative merits of single- and dual-laser systems and a study of the role played by atmospheric turbulence, is presented in Section V.

II. Experimental Apparatus

Our experiments were conducted using several versions of the differential absorption CO_2 LIDAR system shown schematically in Fig. 1. The DIAL system was comprised of a pulsed mini-TEA CO_2 laser, removable $CdGeAs_2$ frequency-doubling crystals for second-harmonic generation, an X10 beam expander, a 40 cm beam-steering mirror, a 30 cm Cassegrain telescope, HgCdTe or InSb detectors, high-speed A/D converters, and a dual-computer data acquisition system. Using this system, the backscattered returns from topographic targets (trees, hills, telephone poles, buildings) were easily detected at ranges up to 2.7 km and at signal-to-noise levels on the order of 10 or more, dependent upon the target reflectivity. The details of each of the subsystems of the DIAL system are presented in the following sections.

A. Mini-TEA CO_2 Laser

A photograph of the mini-TEA CO_2 laser used in our experiments is given in Fig. 2. The main discharge section of this laser consists of a UV-preionized discharge between Rogowski profile electrodes with an active volume of 1.8 cm^3 and has been described previously [10]. The discharge is thyratron triggered and may operate at a pulse repetition frequency (PRF) up to 500 Hz. A gas mixture of $(CO_2:N_2:He:H_2) \approx (1:1.2:0.4:0.2)$ at atmospheric pressure is used in a semi-closed recirculating system for the laser active medium; the overall gas makeup (replenishment) rate is approximately 5 ℓ (STP) per minute and is dependent on the operating PRF. A slight flow of He through tripropylamine is used as a seed gas for photoionization within the discharge.

The laser cavity is approximately 65 cm long and uses a three-mirror configuration. The output coupler is a 1 m radius-of-curvature ZnSe mirror with a reflectivity of 85 percent. A 120 line/mm grating is used as the end mirror. In order to eliminate burning of the grating, a planar mirror (55 percent reflectivity) is placed in the cavity, located approximately 10 cm from the grating. This configuration limits the operating linewidth of the laser to approximately three longitudinal modes ($\approx$700 MHz).

The laser output pulse energy is approximately 20 mJ with a pulsewidth of approximately 100 ns and a TEM_{00} output mode. The laser is tunable over approximately 55 lines within the R and P branches of the CO_2 laser transitions near 9.6 and 10.6 μm. As the laser operates at atmospheric pressure, each laser line can be tuned over its gain bandwidth of approximately 0.02 cm^{-1} by slight adjustment of the grating angle. This laser has proven to be a stable, reliable radiation source for remote sensing experiments. Typical lifetimes for

this laser are on the order of 10^8 pulses before arcing of the main electrodes begins to degrade its performance. At that time, the UV-preionizer electrodes have to be regapped and the main discharge electrodes cleaned of seed gas residue.

B. Optical Configuration

Fig. 3 is a photograph of our dual-laser DIAL system. The two mini-TEA CO_2 lasers serve as the primary radiation source; they are separately triggered with a time delay between the laser firings which can be varied from 2 μs to greater than 200 ms. For experiments conducted with 5 μm radiation, the outputs are frequency-doubled using high-purity $CdGeAs_2$ crystals [11] which were grown at Lincoln Laboratory; pulse averaged doubling efficiencies are typically 10-20 percent, although efficiencies of over 28 percent have been achieved.

The output from the doubling crystals are recollimated and joined through use of a 50/50 ZnSe beamsplitter. Portions of the combined beam are split off by BaF_2 beamsplitters and routed to a spectrometer, a pyroelectric detector for energy calibration, and a 50 cm long cell for absorption calibration; the pyroelectric detectors are Models #410 (Eltec, Inc.) and were used in conjunction with a 20 kΩ load. Since the delay time between each laser discharge is sufficient to permit temporal separation of the pulses, each laser pulse may be calibrated for energy and absorption characteristics on a pulse-to-pulse basis.

The main portion of the laser beam was directed toward an X10 beam expander and enlarged to a 6 cm diameter; the divergence of the beam was measured to be approximately 0.25 mrad. The beam was directed toward targets outside our laboratory window using a remote controlled motor-driven 40 cm beam-steering mirror. Backscattered LIDAR returns were collected by a collinear 30 cm Cassegrain telescope and detected noncoherently by either a 1 mm diameter HgCdTe detector ($D^* = 2.8 \times 10^{10}$ cm $\cdot$ Hz$^{1/2}$ $\cdot$ W^{-1}) for 10 μm radiation or a 1 mm diameter InSb detector ($D^* = 1 \times 10^{11}$ cm $\cdot$ Hz$^{1/2}$ $\cdot$ W^{-1}) for 5 μm radiation; both detectors were cooled to liquid nitrogen temperatures. The field of view of the detector/telescope was approximately 1.1 mrad. A video camera collinear with the LIDAR telescope was used to permit visual pointing of the beam-steering mirror. The angular pointing resolution of the beam-steering mirror was approximately 0.003 mrad.

C. Computer Data Acquisition System

The output pulses from the LIDAR and pyroelectric detectors were routed to a computer controlled high-speed analog-to-digital data acquisition system. A photograph of this system is shown in Fig. 4. The pulsed outputs from the HgCdTe or InSb detector and the pyroelectric detectors were amplified and detected by two 10-bit charge-integrating A/D CAMAC modules (LeCroy Model #2249SG); A/D trigger gate widths were typically 200-300 ns to compensate for the inherent 50-100 ns temporal jitter in the laser pulses. The relative timing of the A/D trigger gates was determined by a set of programmable time delay modules, in order to provide for the necessary time separation between the two laser (LIDAR) pulses as well as the time delay for the LIDAR returns.

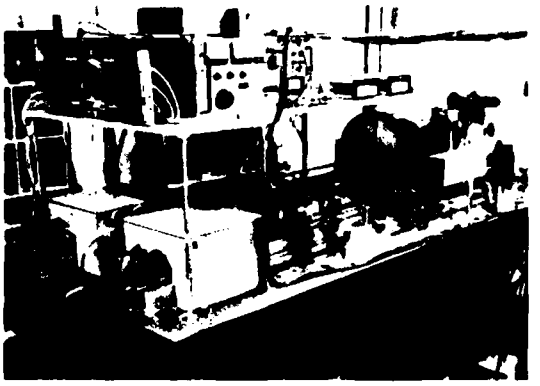

Fig. 3. Photograph of DIAL system.

Fig. 4. Photograph of digital data acquisition system.

The A/D CAMAC modules were interfaced with a LeCroy 3500 data acquisition computer. This computer is based on an eight-bit Intel 8085 central processing unit (CPU) and has dual floppy discs, a hardware floating point processor, 64 kilobytes of memory, CP/M software with FORTRAN, and graphic display. This system is capable of acquiring the input data at high speed, normalizing the LIDAR returns on a pulse-to-pulse basis, and rejecting any data associated with laser misfires. Dependent upon the complexity of the data analysis to be performed, this system is capable of acquiring six channels of input data and can 1) perform a signal average at a rate up to 500 Hz, 2) statistically analyze these data in real time at a rate up to 50 Hz, 3) graphically display the normalized data at a rate up to 20 Hz, and 4) calculate the histogram of the data at a rate up to 100 Hz.

For the overall collection and statistical analysis of these data, the histogram of the data is transferred (<0.3 s) from the LeCroy 3500 computer to a Hewlett-Packard HP9845T computer through use of a GPIB data bus. The HP9845T is used to analyze the DIAL data and perform a statistical analysis (mean, standard deviation, variance of the log normal, and power spectrum) of the data. This analysis is performed in real time while the LeCroy 3500 system is acquiring more LIDAR data. The output from the HP9845T is displayed graphically and a hard copy may be obtained if desired.

We have found this digital data acquisition system to be

extremely useful in our laser remote sensing experiments and it has significantly enhanced the signal-to-noise ratio obtainable with our DIAL system compared to analog signal processing (boxcar integrators and analog ratiometers). The integration capability of an analog boxcar integrator is severely limited by the low duty cycle (PRF times the pulsewidth) of our DIAL system.

III. Theory

The theoretical aspects of laser remote sensing have been covered extensively in the literature [5], [12]-[14]. Therefore, only a brief outline of the pertinent theory related to direct-detection DIAL measurements using backscattered laser radiation from topographic targets will be presented.

The basic concept of the laser remote sensing of atmospheric constituents using a direct-detection, pulsed differential absorption LIDAR (DIAL) system involves the measurement of the intensity of the backscattered radiation from a laser radar (LIDAR) as a function of the frequency of the transmitted laser radiation. For the simplest case, two laser frequencies (λ and λ') are selected such that λ and λ' are on-resonance and off-resonance, respectively, with an absorption transition of the molecular specie which is being measured. The concentration of the absorbing species may be deduced from the differential absorption of the backscattered laser radiation at wavelength λ compared to that at λ'.

The instantaneous power of the backscattered LIDAR radiation, P, may be given approximately by

$$P = (P_t \rho A K/\pi R^2) \exp\left(-2\int(\sigma N + \beta)\, dR\right) \tag{1}$$

where P_t is the transmitted LIDAR power in watts, ρ is the reflectivity of the target, A is the area of the receiving telescope, K is the overall optical efficiency of the system, and R is the range from the LIDAR to the target. σ is the absorption cross section and N is the concentration of the absorbing molecule, and β is the background absorption coefficient of the atmosphere, not including that due to the absorbing molecule (σN); the causal delay term $\delta(t - 2cR)$ is implicit in (1). Equation (1) is valid under the assumption that the projection of the transmitted laser beam at the target is equal to or smaller than the telescope resolution. In (1), the LIDAR return P is dependent upon the frequency of the laser radiation through such terms as σ, β, and possibly ρ.

Equation (1) may be used to represent the case of the laser frequency on-resonance with the molecular absorption transition; a similar equation with P', σ', and β' may be used to represent the case for the off-resonance frequency. These two equations may then be combined to solve for the path averaged concentration of the absorbing molecule N_a, yielding

$$N_a = \frac{\ln(P/P')}{2(\sigma' - \sigma)R}\left[1 - \frac{2(\beta' - \beta)R}{\ln(P/P')}\right] \tag{2}$$

where $N_a \equiv (1/R)\int_0^R N\, dR$. As seen in (2), the path averaged value of the concentration N_a is directly related to the differential absorption of the two LIDAR returns P/P'. The term $2(\beta' - \beta)R/\ln(P/P')$ in (2) represents a correction term due to the frequency-dependent background absorption of the atmosphere; where possible, the laser frequencies λ and λ' are selected such that this term is negligible.

The value of the molecular differential absorption term, $\sigma' - \sigma$ in (2), may be ascertained from laser absorption measurements. The transmission of laser radiation with power P_0 through an absorption cell of length L may be expressed as

$$P_c = P_0 \exp - \sigma N_c L \tag{3}$$

where N_c is the concentration of the gaseous absorber in the cell and P_c is the power of the laser radiation after transmission through the cell. Using (3) and a similar equation with P_c' and σ', one obtains $\sigma' - \sigma = (N_c L)^{-1} \ln(P_c/P_c')$; substitution into (2) yields

$$N_a = N_c\left(\frac{L}{2R}\right)\left(\frac{\ln(P/P')}{\ln(P_c/P_c')}\right)\left[1 - \frac{2(\beta' - \beta)R}{\ln(P/P')}\right]. \tag{4}$$

Equation (4) is especially useful when simultaneous measurements of the differential absorption LIDAR signal and a laboratory absorption cell are available, as in our experiments (Fig. 1). This provides an internal calibration of the absorption coefficients at the laser transmitted frequencies and automatically ensures that frequency drifts of the lasers are properly taken into account; it should be noted that (4) is valid only when the temperature, pressure, and composition of the absorption cell and the ambient atmosphere are equal, so that the population distribution of the absorbing molecules and pressure broadened linewidths are the same.

Equation (4) expresses the path averaged concentration N_a of the atmospheric species in terms of the measured parameters as long as the LIDAR signal-to-noise ratio is large. However, it does not address the problem of detection-range limitations. The detection range is dependent upon several factors that have been discussed extensively in the literature [5], [12]-[14]. One of the most important factors is the minimum change in P and P' which is detectable. This minimal change may be associated either with detector noise limitations or changes in the background absorption of the atmosphere.

The change in the DIAL return ΔP may be expressed, using (1), approximately as

$$\Delta P = P' - P \approx \frac{K\rho A P_t T}{\pi R^2}\left[1 - \exp(-2\sigma N R)\right] \tag{5}$$

where σ' and $\beta - \beta'$ have been assumed to be negligible, N is assumed homogeneous, and T is the atmosphere transmission $T = \exp(-2\beta' R)$. Equation (5) may be used to determine the minimum concentration of the absorbing specie $N_{\min}$ that can be detected.

For the case when the minimal change in the LIDAR return ΔP which can be detected is determined by the detector noise equivalent power NEP, this may be expressed by setting ΔP = NEP in (5) to yield

$$N_{\min} \geq \frac{(\text{NEP})\,\pi R}{2K\rho A P_t \sigma \exp(-2\beta' R)} \tag{6}$$

where it is assumed that $N_{\min}$ is sufficiently small so that $\exp(-2\sigma N_{\min} R) \approx 1 - 2\sigma N_{\min} R$. As seen in (6), the mini-

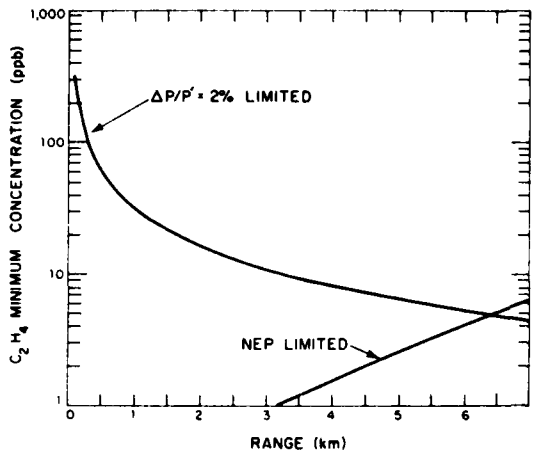

Fig. 5. Estimated DIAL detection sensitivity of atmospheric C_2H_4 as a function of range for the case of detector noise (NEP) limited detection and differential return ($\Delta P/P'$) limited detection.

mum detectable concentration of the pollutant species is dependent on the range and the value of the noise equivalent power NEP.

Another important case is when the uncertainty in the measurement is determined by the minimum fractional change in the LIDAR return $\Delta P/P'$ that can be measured accurately. In this case, (5) yields

$$N_{min} \cong \frac{(\Delta P/P')}{2\sigma R} \tag{7}$$

where again the assumption that $2\sigma N_{min} R \ll 1$ has been made. Equation (7) is useful when large-scale background fluctuations in the LIDAR returns limit the sensitivity of the measurement. This limit is often more restrictive than that imposed by (6).

As an example, one may use typical parameter values for our DIAL system of NEP $\approx 2 \times 10^{-8}$ W, $K \approx 0.1$, $\rho \approx 0.1$, $A \approx 0.06$ m^2, and $P_t \approx 10^5$ W in order to estimate N_{min}. For the remote detection of C_2H_4 using radiation near 10.532 μm, the on-resonance value for σ is 32.1×10^5 (km · atm)$^{-1}$ and β is 0.12 km^{-1} for the U.S. Standard Atmosphere [15]. Using these values in (6) yields, for the NEP-limited detection sensitivity,

$$N_{min}(\text{ppb}) = (16.4 \times 10^{-2})\, R \exp(0.24R) \tag{8}$$

where the range is given in km and the concentration is in parts per billion (ppb) of an atmosphere. Similarly, (7) yields

$$N_{min}(\text{ppb}) = 31.1/R \tag{9}$$

for the $\Delta P/P'$-limited detection sensitivity, where the minimum observable change in $\Delta P/P'$ is taken to be equal to 2 percent (see Section V).

Equations (8) and (9) are plotted in Fig. 5. As seen in Fig. 5, the detection sensitivity of the DIAL measurement of atmospheric C_2H_4 is limited by the differential return ($\Delta P/P'$) at short ranges and by the detector noise (NEP) at the longer ranges.

IV. DIAL Measurements of C_2H_4, CO, and NO

Several evolutionary versions of the DIAL system shown in Fig. 1 were used to detect and measure concentrations of C_2H_4, CO, and NO present in the atmosphere. CO and NO were detected using frequency-doubled CO_2 laser radiation and C_2H_4 using 10.6 μm radiation.

These results were obtained using an early version of the DIAL system shown in Fig. 1 which had only one laser. The laser frequency was shifted from the on-resonance transition to the off-resonance transition through use of a PZT micrometer (Burleigh "Inchworm") to rotate the laser grating. Differential absorption readings were obtained by recording the LIDAR return for a few minutes to establish the off-resonance backscattered signal P' and then switching the laser frequency to the on-resonance transition, thus obtaining the on-resonance value P. In general, the statistical variability (standard deviation) and drift in the observed P' value determined the uncertainty in the measurement.

For the measurements of CO and NO, the signal processing system consisted of boxcar integrators and analog ratiometers. This system was capable of performing a signal average of approximately 5-10 pulses only; this limitation was due to analog signal errors introduced by the integration processing electronics in the boxcar integrators. Later experiments were conducted using the digital data acquisition system shown in Fig. 4. These later experiments included those for the remote sensing of C_2H_4. Details of these experiments are contained in the following sections. Since some of the results for the remote sensing of CO and NO have been published previously [6], [7], our discussion here will be limited to some additional results and a brief description of the most pertinent conclusions.

A. C_2H_4

Laser remote sensing measurements of atmospheric C_2H_4 were conducted using a single-laser DIAL system with the digital data acquisition system shown in Fig. 4. This was done using the coincidence of the absorption transition of C_2H_4 near 10.53 μm with the $P(14)$ laser transition of CO_2. The work presented in this section was conducted to establish measurement uncertainties using the DIAL technique and is an outgrowth of previous work by Murray *et al.* [16] and Rothe [17].

The absorption coincidences pertinent to the measurement of C_2H_4 in the atmosphere are given in Fig. 6, which shows the relative transmission of the atmosphere [18] near 10.53 μm (949 cm^{-1}); also indicated is the increase in absorption near the $P(14)$ CO_2 laser transition due to the presence of 40 ppb of C_2H_4. For the results presented here, the $P(14)$ CO_2 laser line was used as the on-resonance absorption line and the $P(12)$ line was used as the off-resonance transition. The relevant absorption values for C_2H_4 were measured using the laboratory absorption cell filled with 470 ppb of C_2H_4 in air and agreed to within 5 percent with previously published results [19], [20]. These values are $\sigma = 32.1$ (cm · atm)$^{-1}$ and $\sigma' = 4.33$ (cm · atm)$^{-1}$ for the $P(14)$ and $P(12)$ transitions, respectively; the values for the background absorption coefficients of the atmosphere were calculated [15] to be approxi-

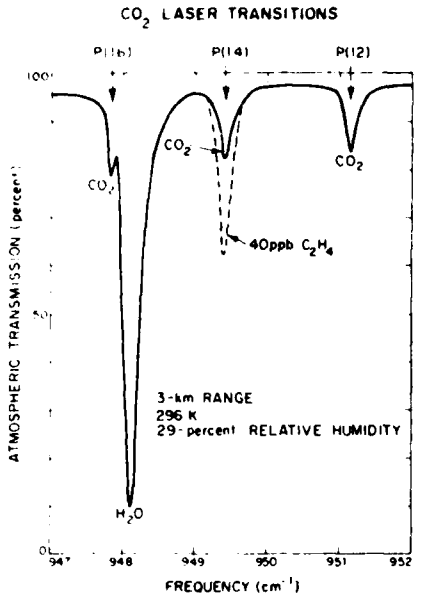

Fig. 6. Transmission spectrum of the atmosphere near 10.53 μm (949 cm^{-1}) relevant to the remote sensing of C_2H_4 using CO_2 laser radiation. The increase in the absorption due to the presence of 40 ppb of C_2H_4 is shown.

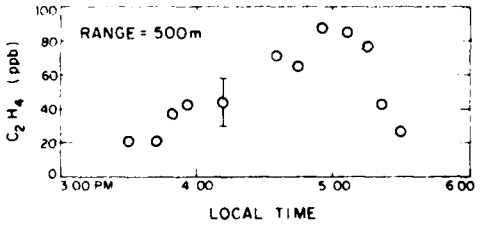

Fig. 7. Dial measurements of C_2H_4 over a traffic roadway.

mately $\beta = 0.122$ km^{-1} and $\beta' = 0.116$ km^{-1}. These values were used in (4) to deduce the path averaged concentration of C_2H_4 from our DIAL measurements.

Using our DIAL system, the concentration of ambient C_2H_4 over a traffic roadway (range 500 m) was measured and the results are shown in Fig. 7. They indicate the increase in the concentration of C_2H_4 due to the increased traffic flow. Peak concentrations of C_2H_4 as high as 230 ppb were measured on other days.

Fig. 8 shows results obtained for a path which transversed a runway of an active airfield adjacent to Lincoln Laboratory located at a range of about 2.2 km; the target used was a flight hangar at a range of 2.7 km. As seen, the ambient background level of C_2H_4 was on the order of 10-20 ppb. Large increases in the atmospheric concentration of C_2H_4 due to aircraft exhaust or fuel emission were observed as air traffic increased. Of interest is the observation that when the wind direction was from the airfield toward our laboratory, significant amounts of C_2H_4 were observed. However, when the wind direction shifted 180° on the next day, little C_2H_4 was detected; aircraft traffic was similar on the two days.

The measurement uncertainty of the airfield results was on

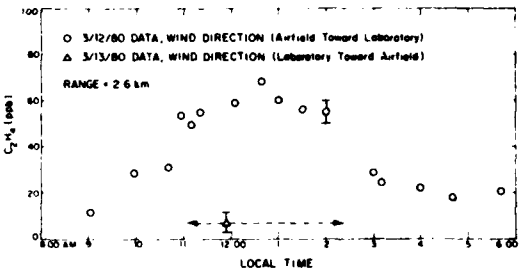

Fig. 8. DIAL measurements of C_2H_4 over an airfield.

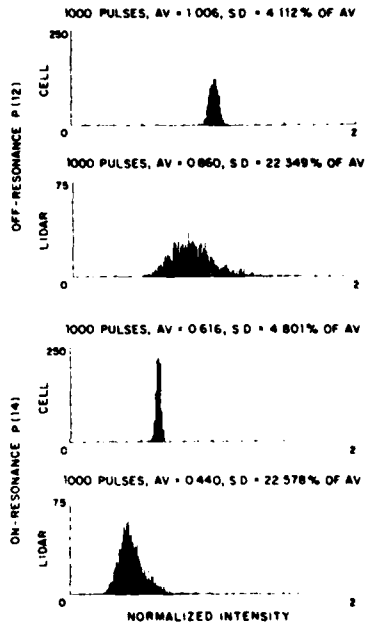

Fig. 9. Histogram (statistical distribution) of LIDAR returns from the airfield and absorption cell signals showing differential absorption due to C_2H_4.

the order of 10 ppb. This error was primarily due to temporal variation in the LIDAR return and the associated statistical uncertainty in determining the mean value of the return. This may be explicitly seen in Fig. 9, which shows the histogram (statistical distribution) of the LIDAR returns from the airfield for both the on-resonance and the off-resonance frequencies; also included are the normalized signals obtained for the absorption cell which contained 470 ppm of C_2H_4 in air. In Fig. 9 the differential absorption is evident for both absorption cell signals as well as the LIDAR returns; the observed change corresponds to an average ethylene concentration in the atmosphere of approximately 60 ± 10 ppb. The effect of such statistical variations on the DIAL measurement error will be discussed more fully in Section V.

B. CO

Remote sensing of CO in the atmosphere requires spectral coincidences between the absorption transitions of CO near 5 μm and a frequency-doubled laser transition of CO_2. In addition, the coincidence should lie in a region of the atmo-

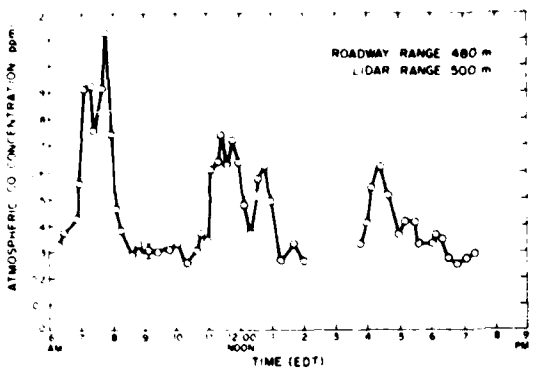

Fig. 10. DIAL measurements of CO over a traffic roadway.

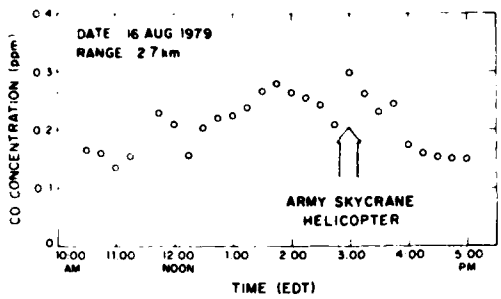

Fig. 11. DIAL measurements of CO over an airfield showing increased concentration due to approach of turbine powered helicopter at a range of 2.4 km.

spheric transmission spectrum that is relatively free of interference. For the detection of CO, our experiments [6], [21] used the absorption coincidence of the frequency-doubled $R(18)$ CO_2 laser transition near 2154.604 cm^{-1} with the $R(2)$ absorption line of CO near 2154.596 cm^{-1}; the frequency-doubled $R(20)$ CO_2 laser transition served as the off-resonance radiation. The path averaged concentration of atmospheric CO was determined from the DIAL returns on the basis of (4); 500 ppm of CO in air (STP) was used in the 50 cm absorption cell for absorption calibration. The pertinent absorption characteristics for the doubled $R(18)$ and $R(20)$ laser transitions were approximately $\sigma = 25.7$ $(cm \cdot atm)^{-1}$, $\sigma' \cong 0$, $\beta = 0.019$ km^{-1}, and $\beta' = 0.036$ km^{-1}, respectively [15].

Fig. 10 shows the atmospheric concentration of CO obtained over the course of several hours for a path which crossed a main traffic roadway leading toward the airfield adjacent to the laboratory. The topographic target used was a painted sign located at a range of 500 m; the roadway was at a range of 480 m. The results shown were obtained by smoothing the DIAL data over 15 min periods. Actual temporal resolution was on the order of seconds and was such that large increases in the CO concentration due to individual cars and trucks were easily observable under light traffic conditions. The results clearly reflect the increased vehicular traffic during the periods of morning arrival, lunchtime, and evening departure.

Measurements of CO were also taken using a topographic target (large painted flight hangar) at a range of 2.7 km. The results are shown in Fig. 11. As seen, the average concentration of CO was measured to be between 160 and 250 ppb. Short-term increases in the CO concentration were recorded when strong sources of CO emission were located close to the DIAL line of sight. The marked increase in CO shown in Fig. 11 was obtained when a turbine-powered Army Skycrane helicopter landed within the laser line of sight at a range of 2.4 km; the observed increase in the path averaged concentration of CO corresponds to a localized CO concentration near the helicopter on the order of 2 ppm, if it is assumed that the increased CO concentration was confined to a region within a radius of 50 m of the aircraft.

The overall measurement error for DIAL detection of CO was approximately ±10 ppb for the 2.7 km measurements and was primarily due to temporal changes in the off-resonance LIDAR signal.

C. NO

For the detection of atmospheric NO, a determination was made of the absorption coincidences which could be used [21], [22]. Consideration of the atmospheric transmission, NO absorption, and available CO_2 laser power eliminated all the coincidences except that between the frequency-doubled 10.6 μm $P(24)$ CO_2 laser line near 1881.098 cm^{-1} and the $R(\frac{1}{2})_{1/2}$ absorption line of NO near 1881.040 cm^{-1}. For this absorption transition, the absorption coefficient σ is approximately [23] 1.2 $(cm \cdot atm)^{-1}$ and the background absorption coefficient β is estimated [15] to be approximately 0.6 km^{-1}. The doubled $P(16)$ and $P(14)$ CO_2 laser transitions near 1877.378 and 1884.768 cm^{-1}, respectively, may be used as the off-resonance transitions; for these transitions, $\beta' = 0.6$ km^{-1} with an uncertainty of ±0.3. These relatively large values for β and β' are due to the strong absorption of water vapor in this spectral region. Because of the large value of β and β' and the uncertainty in these values, the correction term in (4), $2(\beta' - \beta)R/\ln(P/P')$, is not negligible and in fact may be the dominant term in (4).

While the value of β and β' may be estimated by using the HITRAN or LASER computer program (AFGL atmospheric absorption data tapes) [15], [23], small individual errors in the theoretical contributions of a large number of absorption lines may lead to a large error in the differential absorption results $\beta' - \beta$. Because of this possibility, it was determined that an experimental measurement of $\beta' - \beta$ would be essential for the remote sensing of NO in the atmosphere to be accurate.

To experimentally determine the value of $\beta' - \beta$, use was made of the range dependence of the differential absorption LIDAR returns. Taking the derivative of (2), for the case of no absorbing species present ($N_a = 0$), yields

$$\frac{d[\ln(P/P')]}{dR} = 2(\beta' - \beta). \tag{10}$$

Equation (10) indicates that a plot of the logarithm of the ratio of the DIAL returns versus range should lie on a straight line passing through the origin, with a slope equal to twice the difference of the atmospheric absorption coefficients, $2(\beta' - \beta)$.

Using the off-resonance doubled $P(14)$ and $P(26)$ lines,

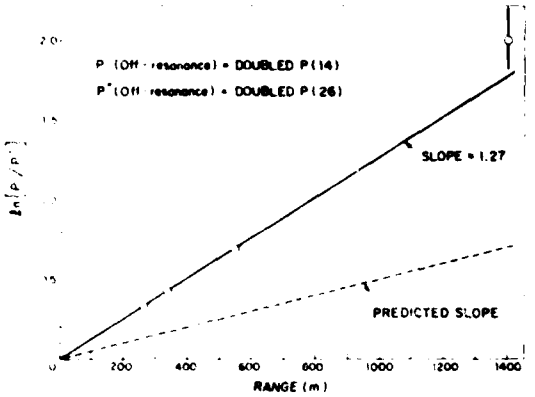

Fig. 12. Differential absorption LIDAR returns as a function of range obtained for the off-resonance doubled $P(14)$ and $P(26)$ lines. The slope of the line indicates the difference in the background atmospheric absorption coefficients, $2(\beta' - \beta)$.

differential absorption returns were obtained as a function of range; our results are shown in Fig. 12. As seen, our results agree with the analytical prediction of (10). However, the measured value of $\beta' - \beta$ is more than twice that predicted using the AFGL tapes for the same atmospheric conditions. These results indicate that the predicted values for β and β' may not be used under our experimental conditions to determine the absolute concentration of NO in the atmosphere.

The range-dependent approach, however, may be used to measure the increase in NO concentration above ambient; ambient levels of NO are generally less than 1 ppb [7]. In this case, using (2), one obtains

$$\frac{d[\ln (P/P')]}{dR} = 2(\beta' - \beta) + 2(\sigma' - \sigma) N_a. \tag{11}$$

As seen in (11), the effect of the presence of NO ($N_a > 0$) is to change the slope of the measured differential absorption return ratio.

Fig. 13 shows results obtained using the on-resonance doubled $P(24)$ transition and the off-resonance $P(26)$ transition for various targets, all located along the same line of sight within an angular spread of 4°. As seen in the figure, the data point at a range of 480 m departs from the ambient background extinction line, indicating an increase in absorption due to the presence of NO. The LIDAR returns corresponding to this data point were obtained for a path which crossed a busy traffic roadway at a height of 3 m. The deviation of this point from the ambient extinction line is well beyond our experimental uncertainty (40 ppb) and corresponds to a path averaged NO concentration of 90 ppb. Concentrations during a period of heavy traffic yielded an NO concentration of up to 250 ppb, as indicated by the arrow and lower data point in Fig. 13.

The laser beam path to the target at 550 m in Fig. 13 passed the traffic roadway at a height of 15 m and was obtained immediately after that obtained from the target at 480 m range. This reduction in NO concentration from the data obtained at a 3 m height over the roadway to that at 15 m is indicative of the fast oxidation rate of NO by ambient oxygen.

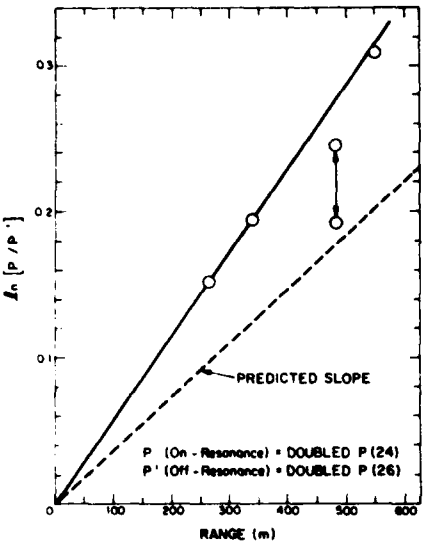

Fig. 13. DIAL measurements of NO. The presence of NO is indicated by the increase in the absorption of the DIAL returns over the ambient extinction value for the target located at 480 m (traffic roadway).

V. Statistical and Temporal Analysis of DIAL Measurement Errors

Our experimental results from the measurements of CO, NO, and C_2H_4 obtained using a single-laser DIAL system indicated that temporal fluctuations in the LIDAR returns represented a basic limitation to the accuracy of these measurements. These fluctuations are due primarily to temporal changes in the atmospheric propagation path of the LIDAR returns and directly influence the statistical error of a DIAL measurement [25]-[31].

It has long been recognized that the use of a dual-laser DIAL system should be able to "freeze out" these temporal fluctuations. Therefore a dual-laser DIAL system should have a smaller measurement uncertainty or error than a single-laser DIAL system. This may be seen by noting that for a single-laser DIAL system the determination of $\ln (P/P')$ in (2) is made by measuring $\ln (\langle P \rangle / \langle P' \rangle)$ where $\langle P \rangle$ is the time average of P. These measurements are made by first measuring the average value of P, $\langle P \rangle$, over a time period of a few seconds or minutes, then switching the laser frequency to subsequently determine $\langle P' \rangle$. Such a DIAL technique is subject to uncertainties caused by temporal changes in the atmosphere between the two sequential measurements. This may be contrasted to measurements obtained using a dual-laser DIAL system; in the case where the time separation between the P-LIDAR return and P'-LIDAR return is sufficiently short to "freeze out" the atmospheric fluctuations, the determination of $\ln (P/P')$ in (2) involves the measurement of pulse pairs $\ln (\langle P_i/P_i' \rangle)$ where the subscript i refers to the ith pulse.

The experimental research to be presented in this section was designed to measure the difference between $\ln (\langle P_i \rangle / \langle P_i' \rangle)$ and $\ln (\langle P_i/P_i' \rangle)$. Using the 10.6 μm dual-laser DIAL and digital data acquisition system shown in Fig. 1, we measured the statistical distribution, energy spectral density, temporal

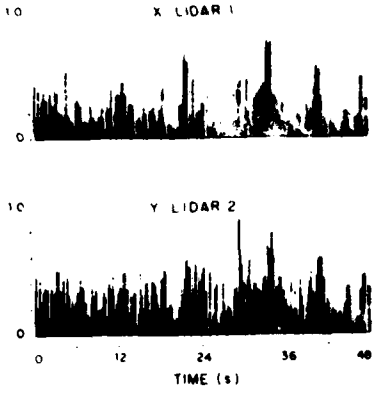

Fig. 14. Temporal history of normalized dual-laser LIDAR returns from a 1 in retroreflector; the time separation between the LIDAR 1 returns, X, and the LIDAR 2 returns, Y, was 35 μs.

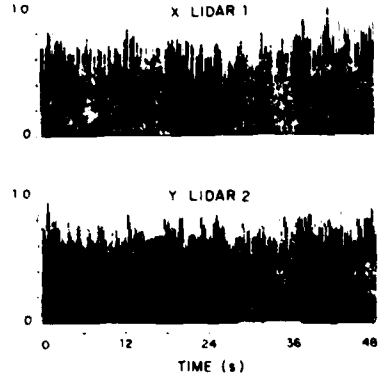

Fig. 15. Temporal history of normalized dual-laser LIDAR returns from a large painted building (diffuse target).

history, and temporal cross correlation of the LIDAR returns from several different targets at different ranges [8]. In addition, the measurement accuracy of the dual-laser DIAL system was determined and compared to that obtainable with the single-laser DIAL system. The observed increase in the measurement accuracy was found to be in good agreement with that predicted from a theory which considered the statistical and temporal character of the DIAL returns [9].

A. Temporal and Statistical Distribution of Dual-Laser LIDAR Returns

The temporal history of approximately 4000 dual-laser LIDAR returns from several different targets was recorded using the DIAL system shown in Fig. 1. Examples of these records are shown in Figs. 14 and 15 for the LIDAR returns obtained from a 1 in retroreflector and a large (>10 m) painted metal building, respectively, both located at a range of 2.7 km. In the figures, the corresponding normalized LIDAR returns for both lasers are presented, where X: LIDAR 1 refers to the returns associated with laser no. 1 in Fig. 1 and Y: LIDAR 2 refers to those associated with laser no. 2; the returns are normalized to the output energy of each laser pulse on a pulse-to-pulse basis. For the data shown, both lasers operated on the 10.611 μm $P(22)$ line at a PRF of 5.4 Hz and

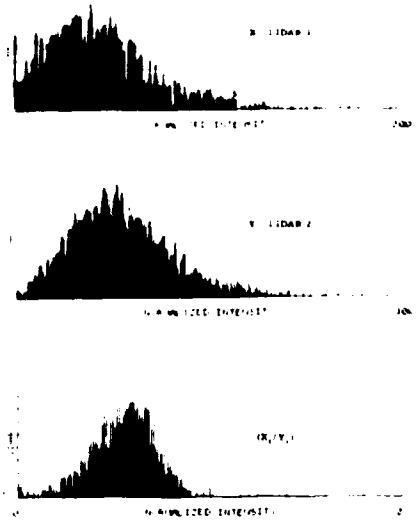

Fig. 16. Statistical distribution (histogram) of dual-laser LIDAR returns from a 1 in retroreflector at a range of 2.7 km and with a time separation between the LIDAR 1 and LIDAR 2 return of 35 μs. The normalized standard deviations of the distribution were $\sigma_x = 0.612$, $\sigma_y = 0.469$, and $\sigma_{x/y} = 0.312$. The alternating dark and light bands within the envelope of the histogram is an artifact and is due to the histogram resolution not being commensurate with the plotting resolution of the display.

the time separation between the laser firings was 35 μs; since both lasers were operating on the same frequency during these experiments, X and Y are used to designate the LIDAR returns rather than P and P'.

As seen in Figs. 14 and 15, the LIDAR returns from the retroreflector (specular target) are significantly correlated in time and have a greater statistical fluctuation than the returns obtained from the large building (diffuse or optically rough target). This is shown explicitly in Figs. 16 and 17, which present the histogram (statistical distribution) of the LIDAR returns using the same data as was used to produce Figs. 14 and 15. Included in Figs. 16 and 17 is the histogram of the ratio of the LIDAR returns on a pulse-pair basis (X_i/Y_i) where X_i is the ith return for LIDAR 1 and Y_i is the ith return for LIDAR 2. As seen from the histograms, the statistical distribution of the returns from the large diffuse target appears to be approximately Gaussian. On the other hand, the returns from the retroreflector are more skewed with a greater proportion of high intensity returns. The observed difference in the statistical distribution is related to the reflective properties of the targets and the relative size of the targets in relation to the transmitting and receiving optics of the LIDAR system [25], [30], [31]. The retroreflector is a specular target and glint (directional reflectance) plays a dominant role in its reflectivity, while the large building is a diffuse (optically rough) target and speckle (interference effects) forms a major reflective component. In addition, the 1 in retroreflector is much smaller than the projected LIDAR beam, while the diffuse target was much larger than the beam. It is interesting to note that the measured variances σ^2 of the distributions agree with preliminary theoretical calculations

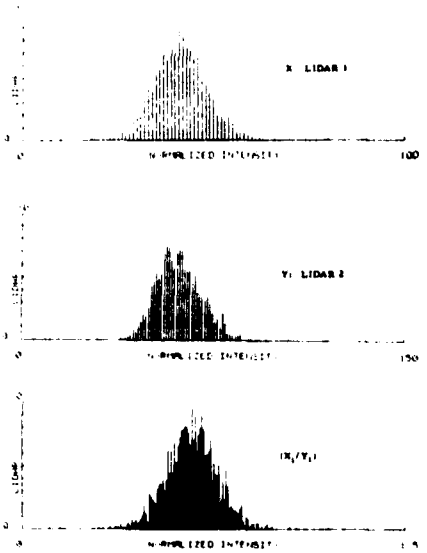

Fig. 17. Statistical distribution of LIDAR returns from a large painted building (diffuse target) at a range of 2.7 km. The normalized standard deviation of the distributions were $\sigma_x = 0.176$, $\sigma_y = 0.150$, and $\sigma_{x/y} = 0.151$.

that take into account the influence of aperture averaging, atmospheric turbulence, and the relative size of the LIDAR transmitting and receiving optics [30]; these calculations will be presented in a later paper after a more thorough investigation has been completed.

The obvious change in the distribution for the ratio of the returns on a pulse-pair basis (X_i/Y_i) compared to either X or Y for the returns from the retroreflector indicate that the higher intensity returns are significantly correlated. On the other hand, such correlation is not as evident for the diffuse target returns. This may be seen quantitatively by a study of the temporal cross correlation of the returns.

The temporal behavior of the DIAL returns was investigated by measuring the cross-correlation coefficient $\rho_{\Delta t}$ of the two LIDAR returns as a function of the time separation Δt between the two laser firings. The cross-correlation coefficient $\rho_{\Delta t}$ may be defined [32] as

$$\rho_{\Delta t} = \frac{\langle (X_i - \bar{X})(Y_j - \bar{Y}) \rangle}{[\langle (X_i - \bar{X})^2 \rangle \langle (Y_j - \bar{Y})^2 \rangle]^{1/2}} = \frac{\sigma_{xy}}{\sigma_x \sigma_y} \tag{12}$$

where X_i is the LIDAR return for LIDAR 1, Y_j is the return for LIDAR 2, Δt is the time separation between the X_i pulse and the Y_j pulse, and $\bar{X} = \langle X_i \rangle$ is the ensemble average of X. σ_{xy} is the covariance of X and Y; σ_x and σ_x^2 are the standard deviation and variance of X, respectively; and σ_y and σ_y^2 are the standard deviation and variance of Y, respectively. As seen in (12), $\rho_{\Delta t}$ represents the fraction of the total statistical fluctuations that is correlated.

Fig. 18 shows results of measurements of the temporal cross-correlation coefficient of the normalized LIDAR returns as a function of the time separation between the two laser pulses. The data shown represent a compilation of several data sets. The individual data points shown in Fig. 18 were

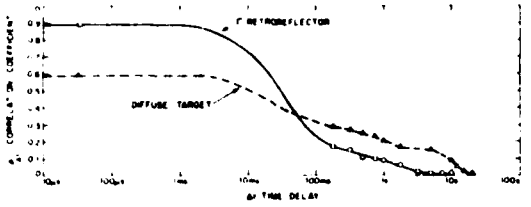

Fig. 18. Measured temporal cross-correlation coefficient $\rho_{\Delta t}$ for dual-laser DIAL returns as a function of time separation Δt.

obtained using the same LIDAR returns as shown in Figs. 14 and 15; in this case $\rho_{\Delta t}$ was calculated using Δt corresponding to nonadjacent pulse pairs X_i and Y_j; thus, $\Delta t = 35\ \mu s + (k/5.4\ \text{Hz})$ where $k = 0, 1, 2, \cdots$. The smooth curves in Fig. 18, shown for time separations less than 100 ms, were obtained from additional DIAL measurements of the same target returns but where the time separation between the two laser firings, Δt, was varied continuously from 3 μs to greater than 200 ms through use of the timing circuitry in Fig. 1 [8].

As seen in Fig. 18, $\rho_{\Delta t}$ is essentially constant for delay times less than 1-3 ms, decreases to a value near 0.1-0.2 for Δt on the order of 100 ms, and gradually decreases to a negligible value for Δt greater than 1-10 s.

This functional form for $\rho_{\Delta t}$ is consistent with previous measurements [33], [34] and is also consistent with a computation of the cross-spectral density function of the LIDAR returns; the cross-spectral density function between two time-history records is equal to the Fourier transform of the cross-correlation function [35]. It should be noted that while the general functional form for $\rho_{\Delta t}$ shown in Fig. 18 was observed for several other similar targets, diurnal variations were observed in the values of $\rho_{\Delta t}$ measured and were observed to be dependent upon atmospheric conditions. In general, it was found that the measured value of $\rho_{\Delta t}$ could vary by ± 0.1 over time periods of 10 to 30 min. As an example, for the diffuse target shown in Fig. 18 the value of $\rho_{\Delta t}$ near $\Delta t =$ 1-10 s was reduced to a value of 0.05 for a limited data set taken just 30 min later. Such variability is indicative of the nonstationary character of the atmosphere.

The observed differences in $\rho_{\Delta t}$ for the different targets may be understood in light of a theory which takes into account an additional uncorrelated noise term σ_u^2 in the overall measured variance of the LIDAR returns. This uncorrelated noise may be explicitly introduced by defining $\sigma_u^2 \equiv \sigma_x \sigma_y - \sigma_{xy}$. The physical interpretation of σ_u^2 may be easily seen under the simplifying conditions where $\sigma_x = \sigma_y \equiv \sigma$ and the variances of the statistical distributions are additive. Under these conditions, one may express the measured variance $\sigma^2 = \sigma_x \sigma_y$ as the sum of a correlated contribution $\sigma_c^2 = \sigma_{xy}$ and an uncorrelated contribution σ_u^2 as $\sigma^2 = \sigma_c^2 + \sigma_u^2$. Equation (12) then may be expressed in the form

$$\rho_0 = \sigma_c^2/(\sigma_c^2 + \sigma_u^2) = 1 - (\sigma_u/\sigma)^2 \tag{13}$$

where ρ_0 is the value of $\rho_{\Delta t}$ taken when Δt is shorter than the decorrelation time of the atmosphere (i.e., $\Delta t \simeq 35\ \mu s$ for the experimental data shown in Fig. 18). Thus, the effect of an uncorrelated noise component is to reduce the measured correlation coefficient from its maximum value of one. The

uncorrelated component of the variance, $\sigma_u^2 = (1 - \rho_0)\sigma^2$, is associated with the measurement uncertainty of the LIDAR returns during the time that the atmosphere is "frozen." The correlated component $\sigma_c^2 = \rho_0\sigma^2$ is related to the increase in the measurement uncertainty due to perturbations imposed on the LIDAR returns by atmospheric turbulence.

The experimental results shown in Fig. 17 and 18 may be compared to that predicted from (13). Using the values $\rho_0 = 0.59$, $\sigma_x = 0.176$, and $\sigma_y = 0.151$ for the diffuse target data, (13) yields $\sigma_u = 0.104$; for the retroreflector, $\rho_0 = 0.87$, $\sigma_x = 0.612$, and $\sigma_y = 0.469$, (13) yields $\sigma_u = 0.193$. Considering the variability in the experimental values of σ_x, σ_y, and ρ_0 taken over different time intervals, the two calculated values for σ_u are in reasonable agreement. This agreement tends to indicate that the observed departure of ρ_0 from unity is due, in part, to the presence and relative strength of the uncorrelated variance $(\sigma_u/\sigma)^2$. There are several possible sources of the uncorrelated noise term σ_u^2. These include laser power normalization errors, laser beam mismatch, the effect of nonadditive statistical distributions and laser propagation characteristics which are not explicitly atmosphere-dependent. Although a preliminary calculation based on the expected influence of atmospheric turbulence upon returns from specular and diffuse targets has been carried out [30], the results indicate that further measurements will be required to establish the relative contributions of these effects to σ_u^2.

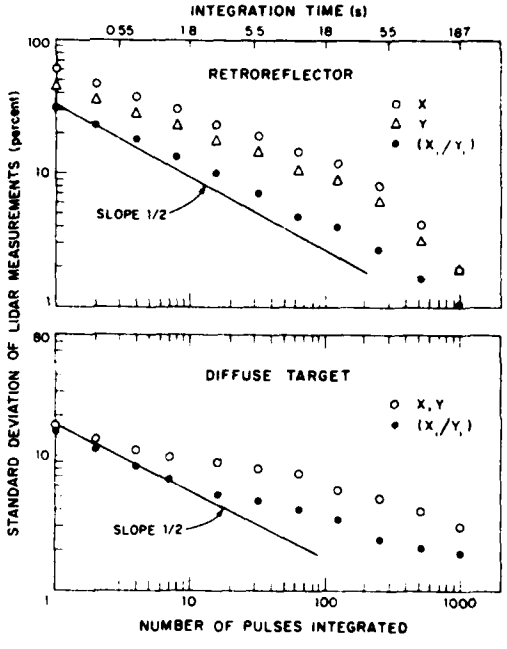

Fig. 19. Measured standard deviation (normalized to the mean) of LIDAR returns as a function of the number of pulses integrated; X and Y are single-laser returns and (X_i/Y_i) is the ratio of the pulse-pair returns.

B. Effects of Correlation on DIAL Measurement Errors

The overall uncertainty of a DIAL measurement is greatly influenced by atmospheric turbulence effects which produce temporal changes in the atmospheric absorption and propagation characteristics. The effect of such temporal changes has been studied extensively for one-way laser propagation. However, little experimental work has been conducted using two-way DIAL measurements. In this section, the results of our experiments [9], which provide information regarding the effect of atmospheric turbulence induced correlation on single- and dual-laser DIAL measurement errors, are given.

In order to investigate how the correlation results presented in Fig. 18 can influence a DIAL measurement, the measurement accuracy (standard deviation) of the dual-laser LIDAR returns were measured. Our results are given in Fig. 19. They are based on the same data as Fig. 18 and show the measured standard deviation (normalized to the mean) of the LIDAR returns as a function of the number of returns integrated. The data was obtained by recording the LIDAR returns for a 10 min period and later performing an integrated moving average of the data; the standard deviation presented in Fig. 19 is the standard deviation of this "moving window" average for N pulses contained within the window. Results are shown in the figure for both the single-laser LIDAR returns X and Y and that obtained by dividing the LIDAR returns on a pulse-pair basis (X_i/Y_i). For clarity, only the standard deviation obtained for X is shown for the diffuse target, since that obtained for Y was essentially the same within ±1 percent. It is evident from the results shown in Fig. 19 that the measurement error of the dual-laser DIAL system is considerably smaller than is obtained with the single-laser system. In addition, the measurement error is seen to decrease approximately as the square root of the number of pulses integrated, $\sqrt{N}$; the $\sqrt{N}$ behavior is expected since, for an ergodic process, the variance of the mean value of the distribution σ_m^2 is related [35] to the variance of the ensemble distribution σ_e^2 as $\sigma_m^2 = \sigma_e^2/N$. It may be noted that a similar set of measurements for the laboratory absorption cell signals yielded a standard deviation (normalized to the mean) on the order of 2-4 percent for $N = 1$ and decreased as the $\sqrt{N}$ to a level of 0.1 percent, the digitization error level of the A/D converters.

The results shown in Fig. 19 can be understood in terms of a theory which considers the effect of the nonzero temporal cross-correlation data (Fig. 18) on the statistical propagation of errors in the DIAL equation; this theory is an outgrowth of previous work by Schotland [36] and Kjelaas *et al.* [37].

The statistical propagation of error in a general function $g = f(Z_1, Z_2 \cdots)$ may be given to first order for slowly varying functions [38] as

$$\sigma_g^2 \simeq \sum_{l,k=1}^{n} \left(\frac{\partial f}{\partial Z_l}\bigg|_0\right)\left(\frac{\partial f}{\partial Z_k}\bigg|_0\right)\sigma_{Z_l Z_k} \tag{14}$$

where higher order terms in (14) associated with the Taylor series expansion are assumed to be negligible and the derivatives are evaluated at the equilibrium (mean) values $\overline{Z}_l$ and $\overline{Z}_k$. Equation (14) may be used on the function $\xi \equiv X_i/Y_i$ to obtain the corresponding measurement error in X/Y. This measurement error is directly related to remote sensing measurements since, in the DIAL equation (3), $\ln(\xi) \equiv \ln(X/Y) \equiv \ln(P/P')$. Performing this operation on ξ and using (12) to

express ρ_0, one obtains for the normalized variance of the dual-laser DIAL measurements

$$\sigma^2_{\ln(\xi)} = \frac{\sigma^2_\xi}{(\bar{\xi})^2} = \frac{\sigma_x^2}{(\bar{X})^2} + \frac{\sigma_y^2}{(\bar{Y})^2} - 2\rho_0 \frac{\sigma_x \sigma_y}{\bar{X}\bar{Y}} \tag{15}$$

where $\sigma_x^2 \equiv \sigma_{xx}$ and $\sigma_y^2 \equiv \sigma_{yy}$. Equation (15) may be simplified under the conditions that $\sigma_x = \sigma_y = \sigma$ and $\bar{\xi} = \bar{X} = \bar{Y} = 1$ as

$$\sigma_\xi^2 = 2\sigma^2 (1 - \rho_0). \tag{16}$$

As seen in (16), a value of $\rho_0 > 0$ reduces the overall dual-laser DIAL measurement error.

The experimental results given in Fig. 19 are in excellent accord with (15). Using the measured value of ρ_0 (Fig. 18) at $\Delta t = 35$ μs of 0.87 and 0.59, and the values from Fig. 19 of $(\sigma_x/\bar{X}) = 0.612$, $(\sigma_y/\bar{Y}) = 0.459$ and $(\sigma_x/\bar{X}) = 0.176$, $(\sigma_y/\bar{Y}) = 0.150$, (15) yields a value of $(\sigma_\xi/\bar{\xi}) = 0.308$ and 0.149 for the retroreflector and diffuse target, respectively. These values are in good agreement with the measured values of $\sigma_\xi/\bar{\xi} = 0.31$ and 0.15 shown in Fig. 19.

The observed deviations from the expected $\sqrt{N}$ behavior of σ versus N in Fig. 19 is also consistent with the long-term behavior of $\rho_{\Delta t}$ for $\Delta t > 200$ ms shown in Fig. 18. Since the effect of signal averaging of N pulses over a time period T is to operate with $1/T \int dt$ on (15), any nonstationary terms such as $\bar{X}$, σ_x, and thus $\rho_{\Delta t}$ in (15) will produce deviations from the expected $\sqrt{N}$ behavior. These deviations exemplify the role that long-term temporal changes in the atmosphere have on the signal averaged DIAL measurement error obtained from the time integral of (15) and are indicative of a nonergodic process (i.e., the ensemble average is not equal to the time average).

Within the framework of the validity of the above analysis it is interesting to relate the dual-laser measurement error $(\sigma_\xi/\bar{\xi})^2$ to the uncorrelated residual noise term presented in (13). Using (13) with (15) and (16), one obtains

$$\sigma_\xi^2 = (\sigma_x - \sigma_y)^2 + 2\sigma_u^2 \sim 2\sigma_u^2 \tag{17}$$

valid for $\sigma_x \simeq \sigma_y$. Equation (17) shows that the dual-laser measurement accuracy is primarily limited by the uncorrelated noise terms in the LIDAR measurements. Experience using the DIAL system shown in Fig. 3 has shown that this residual error term can be significantly reduced through judicious and careful alignment of the laser, optical, and electronic components; these considerations include laser operation in the TEM_{00} mode, appropriate AR-coated beamsplitters, alignment of ac/dc amplifier baselines, calibration of the A/D converters including pulse-to-pulse baseline subtraction, and careful alignment of all optical components. Under optimal conditions, the background measurement error of the internal laboratory absorption cell has been reduced to less than 2 percent. However, this value is considerably less than that of the smallest measured standard deviation of the LIDAR returns from a diffuse target, which is on the order of 8–10 percent and may be attributable in part to changes in the relative pointing direction of the laser beams from pulse to pulse [39].

VI. Conclusion

In this paper we have presented an overview of our laser remote sensing effort using a direct-detection 5 and 10 μm DIAL system. Our studies have demonstrated the capabilities and limitations of this system for the remote sensing of CO, NO, and C_2H_4 in the atmosphere using the backscattered radiation from topographic targets. The uncertainty of these DIAL measurements has been quantified and the results have been shown to be consistent with a simplified theory which, to first approximation, gives a quantitative formulation of the overall DIAL measurement error. The measurements presented here were obtained with a direct-detection DIAL system. It will be of considerable interest to extend these measurements to include the use of a heterodyne CO_2 DIAL system in order to compare the operational characteristics and associated measurement errors of both direct-detection and heterodyne-detection systems.

Acknowledgment

The authors would like to extend their appreciation for the helpful suggestions and encouragement of A. Mooradian and P. L. Kelley, who have been instrumental in the laser remote sensing effort. In particular, they would like to thank P. F. Moulton who helped in the design and development of the DIAL system. In addition, they would like to acknowledge the expert technical help of W. E. DeFeo and E. F. Casazza in the construction of the experimental apparatus.

References

[1] R. A. Baumgartner and R. L. Byer, "Remote SO_2 measurements at 4 μm with a continuously tunable source," *Opt. Lett.*, vol. 2, pp. 163–165, 1978.

[2] J. A. Cooney, "Measurements on the Raman component of laser atmospheric backscatter," *Appl. Phys. Lett.*, vol. 12, pp. 40–42, 1968.

[3] J. R. Rowlett, C. S. Gardner, E. S. Richter, and C. F. Sechrist, Jr., "LIDAR observations of wave-like structure in the atmospheric sodium layer," *Geo. Phys. Lett.*, vol. 5, pp. 683–686, 1978.

[4] C. C. Wang, L. I. Davis, Jr., P. M. Selzer, and R. Munoz, "Improved airborne measurements of OH in the atmosphere using the technique of laser-induced fluorescence," *J. Geophys. Res.*, vol. 86, pp. 1181–1186, 1981.

[5] H. Kildal and R. L. Byer, "Comparison of laser methods for the remote detection of atmospheric pollutants," *Proc. IEEE*, vol. 58, pp. 1644–1663, 1971.

[6] D. K. Killinger, N. Menyuk, and W. E. DeFeo, "Remote sensing of CO using frequency-doubled CO_2 laser radiation," *Appl. Phys. Lett.*, vol. 36, pp. 402–405, 1980.

[7] N. Menyuk, D. K. Killinger, and W. E. DeFeo, "Remote sensing of NO using a differential absorption LIDAR," *Appl. Opt.*, vol. 19, pp. 3282–3286, 1980.

[8] —, "Temporal correlation measurements of pulsed dual CO_2 LIDAR returns," *Opt. Lett.*, vol. 6, pp. 301–303, 1981.

[9] D. K. Killinger and N. Menyuk, "Effect of turbulence-induced correlation on laser remote sensing errors," *Appl. Phys. Lett.*, June 1981.

[10] N. Menyuk and P. F. Moulton, "Development of a high-repetition-rate mini-TEA CO_2 laser," *Rev. Sci. Instr.*, vol. 51, pp. 216–220, 1980.

[11] N. Menyuk, G. W. Iseler, and A. Mooradian, "High-efficiency high-average-power second-harmonic generation with $CdGeAs_2$," *Appl. Phys. Lett.*, vol. 29, pp. 422–424, 1976.

[12] R. L. Byer, "Review: Remote air pollution measurement," *Opt. Quantum Electron.*, vol. 7, pp. 147–177, 1975.

[13] G. Megie and R. T. Menzies, "Complementarity of UV and IR differential absorption LIDAR for global measurements of atmospheric species," *Appl. Opt.*, vol. 19, pp. 1173-1183, 1980.
[14] B. J. Rye, "The reference range for atmospheric backscatter LIDAR," *Opt. Quantum Electron.*, vol. 11, pp. 441-446, 1979.
[15] R. A. McClatchey and A. P. D'Agati, "Atmospheric transmission of laser radiation: Computer code LASER," AFGL-TR-78-0029, 1978.
[16] E. R. Murray and J. E. van der Laan, "Remote measurement of ethylene using a CO_2 differential-absorption LIDAR," *Appl. Opt.*, vol. 17, pp. 814-817, 1978.
[17] K. W. Rothe, "Monitoring of various atmospheric constituents using a CW chemical hydrogen/deuterium laser and a pulsed carbon dioxide laser," *Radio Electron. Eng.*, vol. 50, pp. 567-574, 1980.
[18] R. J. Nordstrom, J. H. Shaw, W. R. Skinner, J. G. Calvert, W. H. Chan, and W. M. Uselman, "Application of Fourier transform spectroscopy to air polution problems; Interim report, computer-generated long-path air spectra," Env. Res. Lab. Rep. EPA-600/3-77/026, 1977.
[19] R. R. Patty, G. M. Russwurm, W. A. McClenny, and D. R. Morgan, "CO_2 laser absorption coefficients for determining ambient levels of O_3, NH_3, and C_2H_4," *Appl. Opt.*, vol. 13, pp. 2850-2854, 1974.
[20] A. Mayer, J. Comera, H. Charpentier, and C. Jaussaud, "Absorption coefficients of various pollutant gases at CO_2 laser wavelengths; Application to the remote sensing of these pollutants," *Appl. Opt.*, vol. 17, pp. 391-393, 1978.
[21] A. Mooradian, D. K. Killinger, and N. Menyuk, "Remote sensing of turbine engine gases: Final report," ESD-TR-79-319/ESL-TR-80-09 (DDC AD-A084544), 1979.
[22] A. Valentin, J. P. Boissy, P. Cardinet, A. Henry, D. W. Chen, and K. N. Rao, "Determination, from NO fundamental band spectrum, of rotational, spin-orbit coupling and Λ type doubling constants for (v = 0) and (v = 1) levels," *C. R. Acad. Sci.*, vol. 283B, pp. 233-236, 1976.
[23] R. A. McClatchey, W. S. Benedict, S. A. Clough, D. E. Burch, R. F. Calfee, K. Fox, L. S. Rothman, and J. S. Garing, "AFCRL atmospheric absorption line parameters compilation," AFCRL-TR-73-0096, 1973.
[24] M. E. Thomas and R. J. Nordstrom, private communication.
[25] J. W. Goodman, "Some effects of target-induced scintillation on optical radar performance," *Proc. IEEE*, vol. 53, pp. 1688-1700, 1965.
[26] R. S. Lawrence and J. W. Strohbehn, "A survey of clear-air propagation errors relevant to optical communications," *Proc. IEEE*, vol. 58, pp. 1523-1545, 1970.
[27] J. L. Bufton, R. S. Iyer, and L. S. Taylor, "Scintillation statistics caused by atmospheric turbulence and speckle in satellite laser ranging," *Appl. Opt.*, vol. 16, pp. 2408-2413, 1977.
[28] R. L. Fante, "Electromagnetic beam propagation in a turbulent media: An update," *Proc. IEEE*, vol. 68, pp. 1424-1442, 1980.
[29] S. F. Clifford and R. J. Hill, "Relation between irradiance and log-amplitude variance for optical scintillation described by the K distortion," *J. Opt. Soc. Amer.*, vol. 71, pp. 112-114, 1981.
[30] J. H. Shapiro, "Imaging and target detection with a heterodyne-reception optical radar," Project Rep. TST-24, ESD-TR-78-275 (DDC AD-A063767), Lincoln Laboratory, M.I.T., 1978.
[31] ——, "Target detection with a direct-reception optical radar," Project Rep. TST-27, ESD-TR-78-290 (DDC AD-A065627), Lincoln Laboratory, M.I.T., 1978.
[32] G. E. P. Box and G. M. Jenkins, *Time Series Analysis.* San Francisco: Holden-Day, 1976.
[33] R. T. Ku, D. Hinkley, and J. O. Sample, "Long-path monitoring of atmospheric carbon monoxide with a tunable diode laser system," *Appl. Opt.*, vol. 14, pp. 854-861, 1975.
[34] B. Marthinsson, J. Johnasson, and S. T. Eng, "Air pollution monitoring with a computer-controlled CO_2-laser long-path absorption system," *Opt. Quantum Electron.*, vol. 12, pp. 327-334, 1980.
[35] J. S. Bendat and A. G. Piersol, *Engineering Applications of Correlation and Spectral Analysis.* New York: Wiley, 1980.
[36] R. M. Schotland, "Errors in the LIDAR measurement of atmospheric gases by differential absorption," *J. Appl. Meteor.*, vol. 13, pp. 71-77, 1974.
[37] A. G. Kjelaas, P. E. Nordal, and A. Bjerkestrand, "Scintillation and multiwavelength coherence effects in a long-path laser absorption spectrometer," *Appl. Opt.*, vol. 17, pp. 277-284, 1978.
[38] S. L. Meyer, *Data Analysis for Scientists and Engineers.* New York: Wiley, 1975.
[39] M. H. Lee and J. F. Holmes, "Effect of the turbulent atmosphere on the autocovariance function for a speckle field generated by a laser beam with random pointing error," *J. Opt. Soc. Amer.*, vol. 71, pp. 559-565, 1981.

Dennis K. Killinger was born in Boone, IA, on September 23, 1945. He received the B.A. degree from the University of Iowa, Iowa City, the M.A. degree from DePauw University, Greencastle, IN, and the Ph.D. degree in physics from the University of Michigan, Ann Arbor, in 1967, 1969, and 1978, respectively.

From 1969 to 1974 he conducted research on optical and microwave atmospheric propagation while employed as a research physicist at the Naval Avionics Laboratory. During 1974 to 1978, he was a Research Assistant at the University of Michigan where his research activities centered around laser physics, quantum optics, and molecular spectroscopy. He held a post-doctoral position at the Ford Scientific Research Laboratory during 1978 and 1979 where his research included the study of the oscillator strength, Gibbs free energy, and rotational electronic interaction of the OH free radical using high-resolution CW and pulsed frequency-doubled dye lasers. In 1979 he joined the Research Staff of the Quantum Electronics Group at Lincoln Laboratory, Massachusetts Institute of Technology, Lexington, MA, and is currently Program Manager of the Laser Remote Sensing Program. His present research activities have been directed toward the application of new laser, spectroscopic, and optical techniques for the remote sensing of trace species in the atmosphere.

Dr. Killinger is a member of the American Physical Society and the Optical Society of America.

Norman Menyuk was born in New York City, NY, in 1923. He received the B.S. degree from the South Dakota School of Mines and Technology, Rapid City, and the M.S. degree from Ohio State University, Columbus, in 1948 and 1949, respectively, both in physics.

Since 1952 he has been at Lincoln Laboratory, Massachusetts Institute of Technology, Lexington, MA, where for several years he was engaged in solid-state research involving magnetic phenomena. Since joining the Quantum Electronics Group he has investigated optical pumping of semiconductors, frequency conversion, laser development, and, most recently, the application of the latter two areas of research to problems of atmospheric remote sensing.

Mr. Menyuk is a Fellow of the American Physical Society, a member of the Optical Society of America, the New York Academy of Sciences, and an affiliate member (Magnetics Section) of the IEEE.

APPENDIX D

The following is a preprint of a journal article to be published in Applied Optics entitled "Laser Remote Sensing of Hydrazine, MMH, and UDMH Using a Differential-Absorption CO_2 LIDAR."

LASER REMOTE SENSING OF HYDRAZINE, MMH AND UDMH USING A DIFFERENTIAL-ABSORPTION CO_2 LIDAR*

N. Menyuk, D. K. Killinger, and W. E. DeFeo
Lincoln Laboratory, Massachusetts Institute of Technology
Lexington, Massachusetts 02173

Abstract

A dual mini-TEA CO_2 laser differential-absorption LIDAR system has been used to test the remote sensing of hydrazine, unsymmetrical dimethylhydrazine (UDMH) and monomethylhydrazine (MMH) under atmospheric conditions. Average concentrations of these compounds were measured using backscattered laser radiation from a target located at a range of 2.7 km. The experimental results indicate that average atmospheric concentration levels of the hydrazine compounds of the order of 40-100 parts per billion can be detected over ranges between 0.5 and 5 km. The level of concentration sensitivity over this interval was found to be limited primarily by atmospheric fluctuations. An investigation of the effect of these fluctuations on measurement uncertainties indicated that the fluctuations reduce the benefits of signal averaging over N pulses significantly below the expected square-root of N improvement. It is also shown that uncertainties due to long-term atmospheric drifts can effectively be reduced through use of dual-laser LIDAR return ratios.

*This work was supported by the Air Force Engineering and Services Center.

I. Introduction

The single-ended differential-absorption LIDAR (DIAL) technique has proved to be a sensitive method for the long-range remote sensing of molecular constituents in the ambient atmosphere. DIAL systems operating in the infrared have been used for monitoring the presence of major atmospheric constituents such as CO,[1,2] as well as trace constituents such as C_2H_4,[3,4] NO,[5] SO_2,[6] ozone[7] and others.[8] In this paper we report on the use of an infrared DIAL system to test the long-range remote sensing of hydrazine, monomethylhydrazine (MMH) and unsymmetrical dimethylhydrazine (UDMH) under atmospheric conditions. These compounds, which are used as rocket fuels among other applications, are known to be highly toxic.[9] To our knowledge, these measurements represent the first experimental test of long-range laser remote sensing of toxic hydrocarbon vapors in an atmospheric environment.

The possibility of accidental release of these compounds into the atmosphere, coupled with their acute toxicity, makes the ability to sensitively monitor their presence in the atmosphere extremely important. These considerations led Loper and his colleagues[10] to measure the vapor-phase absorption cross-sections of these compounds at a large number of CO_2 laser frequencies, where the hydrazines have moderately strong absorption bands. They used the results to estimate achievable detection sensitivities for the hydrazines and experimentally confirmed their estimate for UDMH in a laboratory experiment using a photoacoustic detection system.

In this paper, an experimental study is presented which includes an extension of the Loper et al.[10] measurements as well as an investigation of the capabilities and limitations of the DIAL technique as a rapid and sensitive means for remotely measuring the presence of hydrazine compounds in the atmosphere. Our experiments were carried out using a dual-laser CO_2 DIAL system in conjunction with a large optical tank which contained the toxic hydrazine compounds. LIDAR returns were obtained from laser beams which passed through the tank and were reflected from a topographic target at a range of 2.7 km. The experimental results established the capability of the DIAL system to remotely sense the presence of the hydrazine compounds

with a path-averaged detection sensitivity of 40 to 100 parts per billion (ppb) at this range, with the limitation set by atmospheric fluctuation. In addition, the results showed the dual-laser DIAL system to be capable of performing these measurements in real time despite the known rapid reactivity of the hydrazine compounds in air.[11,12]

The remote-sensing measurements and an analysis of the experimental results form the principal subjects of this paper. A description of the DIAL system used for these measurements is given in Section II. The basis for the choice of CO_2 laser transitions used for each of the molecules investigated is discussed in Section III. The effects of an air atmosphere on the temporal variation of the hydrazine compounds, and the ability of the DIAL system to follow these changes were studied in the laboratory, with the results described in Section IV. The remote sensing experimental results are given in Section V, and these results are analyzed in Section VI, where it is shown that atmospheric fluctuations are the major source of measurement uncertainty. To achieve a better understanding of these fluctuations and of the improvements achievable through signal averaging, additional experiments were carried out to study explicitly the accuracy and sensitivity limitations imposed on remote sensing measurements by the combination of atmospheric and temporal effects. The results of these experiments are given in Section VII.

II. Experimental Apparatus

The dual-laser DIAL system used in these experiments is shown schematically in Fig. 1, and has been described previously.[5,13] Two line-tunable mini-TEA CO_2 lasers[14] provided the pulsed transmitted radiation. Laser 1 was normally tuned to the low-absorption transition frequency and laser 2 was tuned to the high-absorption frequency of the hydrazine, UDMH or MMH species. The two lasers were separately triggered, and the time delay between the firing of the two lasers was maintained at 50 μs. For this short a delay time, the atmosphere is essentially "frozen" between firings.[13] The beam paths from the two lasers were joined through use of a 50/50 beam splitter. A portion of each beam was then directed to a pyroelectric detector to normalize the output of each pulse, and another portion was sent

through a Pyrex absorption cell (33 cm long x 2.54 cm dia. with BaF_2 windows) to a second pyroelectric detector. The cell served to calibrate absorption levels of the hydrazine compounds at the frequencies emitted by our lasers. The major part of the laser radiation was sent through a 10X beam expander and directed toward a topographic target located at a range of 2.7 km. The LIDAR returns and pyroelectric signals were recorded and analyzed in a computerized data acquisition system which determined the normalized differential-absorption of both the laser radiation through the laboratory absorption cell and the LIDAR returns. To measure absorption of the hydrazine compounds along the LIDAR path, a large, enclosed, chemically inert polypropylene tank 104 cm long x 62.5 cm dia. with 15° slanted polyethylene windows was placed outside the laboratory in the path of the laser beam. A moving polypropylene "flapper" was placed inside the tank to reduce stratification of the hydrazine species. The use of the tank as an enclosure for the hydrazine compounds was necessary in view of the known toxicity[9] of these species.

III. Choice of Laser Frequencies for Differential-Absorption Measurements of Hydrazine, UDMH and MMH

The choice of laser frequencies for the accurate real-time remote-sensing measurements of hydrazine compounds in the atmosphere must provide for a sufficient difference in absorption levels to yield a meaningful differential absorption in the laser return signals. In addition, atmospheric transmission and possible interference effects from other atmospheric species must be considered. The choice of frequencies is limited to those laser transitions available with our mini-TEA CO_2 lasers. Single line radiation has been obtained with these lasers from the P(8) to P(36) and the R(10) to R(34) lines of the $(00°1)$-$(10°0,02°0)_I$ transition near 10.6 μm and from the P(10) to P(34) and the R(10) to R(34) lines of the $(00°1)$-$(10°0,02°0)_{II}$ transitions near 9.4 μm.[14] The differential-absorption coefficients of hydrazine, UDMH and MMH at these CO_2 laser transition frequencies have been measured by Loper et al.[10] using a tunable low-pressure cw CO_2 laser.

The atmospheric transmission and possible interferences of other molecular species are obtained from the AFGL tapes of McClatchey et al.[15] Among

the potential interfering species, ethylene and ammonia are of particular importance. Ethylene exists as a trace molecule in the atmosphere and is present in vehicle exhausts. Average concentration levels in excess of 60 parts per billion (ppb) have been observed over an airbase.[4] Ammonia is both an atmospheric trace molecule with a normal concentration[16] between 2 and 20 ppb and a reaction product of hydrazine decomposition. We have used the absorption coefficients of ammonia and ethylene obtained at the CO_2 laser frequencies by Patty et al.[17]

On the basis of the above considerations, CO_2 laser frequency pairs were chosen which yielded as large a differential-absorption as possible consistent with minimal interference effects from either ethylene or ammonia. It should be noted that it is desirable to choose the frequency pairs close together in order to maximize the mutual coherence[18,19] of the two laser beams; however, this proved to be impractical for both UDMH and MMH.

A. Hydrazine (N_2H_4)

Significant absorption of hydrazine[10] occurs only in the 10.6-μm band of CO_2 laser transitions. CO_2 laser wavelengths longer than the P(30) line are eliminated by the extremely high NH_3 absorption. The most suitable laser transition pair is the P(22) transition at 10.611 μm as the high-absorption line and the P(28) transition at 10.674 μm as the low-absorption line. The corresponding absorption coefficients[10] are 5.41 and 2.17 $(cm\ atm)^{-1}$, respectively, yielding a differential-absorption of $\Delta\sigma = 3.24\ (cm\ atm)^{-1}$. With this choice, the frequencies are closely spaced, the differential-absorption levels of both C_2H_4 and NH_3 are smaller than that of hydrazine by over an order of magnitude, and the atmospheric transmittance level is acceptable at both frequencies. The corresponding absorption values are given in Table I along with the background atmospheric attenuation, β, for a U. S. Standard Atmosphere.[15]

B. UDMH $(CH_3)_2N_2H_2$

The choices of laser transition pairs for DIAL measurements of UDMH are extremely limited. The absorption coefficient of UDMH in the 9.4-μm CO_2 laser band is approximately 1.5 $(cm\ atm)^{-1}$, with very little variation within the R and P branches.[10] Significant absorption occurs in

the 10.6-μm band only for the longer wavelengths of the P branch, rising from ~ 1 to near 3 (cm atm)$^{-1}$ between the P(28) and P(36) laser transitions of the 10.6-μm band. There is virtually no absorption of UDMH within the R branch of the 10.6-μm band [$\sigma \sim 0.05$-0.2 (cm atm)$^{-1}$].

Absorption interferences occur in the 10.6-μm P branch due to NH_3 absorption lines. Between the P(32) and P(36) transitions, NH_3 absorption is a factor of 3 to 7 times greater than that of UDMH. Although NH_3 is only a minor product of UDMH decomposition,[12] this large a relative absorption level coupled with the possible presence of even small amounts of ambient NH_3 effectively allows only the P(28) or P(30) to be used for the high-absorption transitions. The UDMH absorption coefficients for these lines are 1.11 and 1.45 (cm atm)$^{-1}$, respectively.[10]

For the low-absorption transition, no other line could be found within the P branch of the 10.6-μm CO_2 laser band which, in conjunction with either the P(28) or P(30) transition, would yield a differential absorption level which was of the order of unity and significantly discriminated against both NH_3 and C_2H_4. In order to do so, it was necessary to choose the low-absorption line from within the R branch of the 10.6-μm band. Thus, the most suitable laser transition pair appears to be the P(30) line as the on-resonance transition and the R(10) line as the off-resonance transition, both in the 10.6-μm band. The relevant absorption values are given in Table I.

C. MMH ($CH_3N_2H_3$)

It is difficult to find a suitable pair of CO_2 laser transitions for the remote sensing of MMH. There is little MMH absorption anywhere within the 9.4 μm band, while absorption value variations within the available transition lines of the 10.6-μm band are extremely small. The single exception is the R(8) line, for which $\sigma = 3.5$ (cm atm)$^{-1}$ compared to values near unity for neighboring transitions.[10] However, the CO_2 mini-TEA lasers do not operate easily on this line; in addition, the absorption coefficient of NH_3 at the frequency of this transition is extremely large, namely 25.8 (cm atm)$^{-1}$. Therefore it was necessary to consider transition pairs involving CO_2 laser lines in different bands. It was found that of all the

9.4-μm band transitions only the R(18) transition will yield a sufficiently low C_2H_4 differential-absorption level to serve as a suitable off-resonance line. Further consideration established the R(30) line in the 10.6-μm band as the preferred on-resonance MMH-absorption transition. The absorption values for this transition pair are also given in Table I.

Although the absorption coefficients given by Loper et al.[10] were used to establish the preferred transitions for differential-absorption, the difference in the nature of their CO_2 laser and the CO_2 lasers used in our DIAL system requires that we separately determine the coefficients in conjunction with our differential-absorption measurements. Loper's results were obtained with a low-pressure cw CO_2 laser, which generally has a narrow gain-bandwidth (~ 100 MHz) capable of supporting only a single longitudinal mode located at or near line center. However, to achieve the high peak laser power needed for long-range remote sensing, our coherent radiation was provided by pulsed mini-TEA lasers operating at atmospheric pressure. These lasers have collision broadened gain-bandwidths on the order of 1 GHz and generally operate on more than one longitudinal mode within a single transition line. Each mode operates at a slightly different frequency and some tunability exists within each line. Therefore, there may well be differences between the absorption coefficient of a given molecule for a given CO_2 laser transition as measured by a TEA laser and by a low-pressure laser. This problem is overcome in our experiments by measuring the absorption coefficient of the molecule in the absorption cell simultaneously with the remote sensing measurement. This was done in conjunction with the remote sensing experiment described in Section V below; our resultant absorption coefficient values are included in Table I.

IV. Laboratory Measurements of Hydrazine Compounds in Air

Measurements of the differential absorption of the hydrazine compounds in an air atmosphere were carried out within the laboratory using the laboratory portion of the system shown in Fig. 1. In view of the reactivity of

the hydrazine compounds in air, these measurements were necessary to establish the ability of our dual-laser DIAL system to follow the instantaneous changes in concentration of the compounds in real time and to determine the extent to which this can be accomplished while averaging over a sufficiently large number of pulses to significantly reduce measurement uncertainties.

The measurements consisted of firing laser no. 1 on the low-absorption transition line followed by laser no. 2 firing 50 μs later on the high-absorption transition. Each beam was split, with one portion going to pyroelectric detector no. 1 to serve as the normalizing beam. The remainder of the beams passed through the Pyrex absorption cell which initially contained air at atmospheric pressure and to which a known amount of a hydrazine compound (in liquid form) was added. The beam transmitted through the cell was recorded by pyroelectric detector no. 2. The detector outputs along with gating circuitry then went to the computer system where each individual pulse was normalized to the laser energy in each pulse on a pulse-to-pulse basis. The normalized pulses from each laser were averaged over a preset number of pulses. The computer system was able to perform the normalization and averaging functions in real time with the lasers operating at a pulse repetition frequency of slightly under 20 Hz.

The 100% transmittance level through the absorption cell was established by recording the values of the normalized laser beams, averaged over a thousand pulses, after passage through the absorption cell containing air at atmospheric pressure. A known volume of a hydrazine compound in liquid form was then inserted by hypodermic syringe into the cell and the laser beam transmittance observed as a function of time. Initial values of the average relative transmittance were taken for every 100 pulses; after the rate of change declined sufficiently, values were taken of the average of 500 pulses from each laser. The system was able to average over this number of pulses and still follow the changing concentration levels without difficulty. As the following results will show, the temporal change in the concentration of the three compounds differed markedly from each other.

A. Hydrazine

The change in the relative transmittance of the P(22) and P(28) CO_2 laser transitions of the 10.6 μm band through the air-filled laboratory

cell after introducing 0.9 μℓ and 7.6 μℓ of hydrazine is shown as a function of time in Fig. 2. The results obtained using 0.9 μℓ of hydrazine indicate a maximum differential absorption almost an order of magnitude lower than the value that would be expected on the basis of published absorption coefficients[10] if one assumed all the hydrazine was present in vapor form. This large reduction is due to a combination of two effects; first, hydrazine has a slow vaporization rate due to its low vapor pressure (~ 14 Torr at 298 K)[9] and second, the hydrazine vapor has a high oxidation rate. Hence this result is not particularly surprising. It was observed that even after the absorption levels started to decrease, which occurred about 12 min after the introduction of hydrazine, some liquid was still present in the cell.

Figure 2 also shows the results after introducing 7.6 μℓ of hydrazine, an amount exceeding that required to produce a saturated vapor pressure (~ 4.4 μℓ). In this case, the relative transmittance reached a minimum value in less than 4 minutes and returned to a near-normal value after about 15 min. The maximum effective differential-absorption achieved under these conditions was approximately a factor of 4 below that predicted for saturated hydrazine vapor in the cell.

It is apparent from Fig. 2 that the DIAL system is capable of following relatively rapid changes in hydrazine concentration while averaging over large numbers (~ 100-500) of pulses.

B. UDMH

The time variation of transmittance through the air-containing absorption cell after the insertion of 9 μℓ of UDMH is shown in Fig. 3. These results are quite different than those shown in Fig. 2 for hydrazine. The vapor pressure of UDMH at room temperature (~ 160 Torr)[9] is an order of magnitude greater than that of hydrazine and, as seen in Fig. 3, the relative transmittance of both the P(30) and the R(10) radiation reaches a minimum within a minute after the insertion of the UDMH into the cell. The transmittance level then remains virtually constant, in agreement with studies[12,20] which indicate that UDMH is highly stable, even in an oxygen atmosphere.

C. MMH

Monomethylhydrazine has a vapor pressure of approximately 50 Torr at room temperature[9] and is much less volatile than UDMH. The variation with time of the relative transmittance of the 9.28 μm R(18) and 10.18 μm R(30) transitions after inserting 9 μℓ of MMH into the air-filled absorption cell is shown in Fig. 4. While the relative transmittance of both transitions decreased rapidly for the first 3-4 minutes, the relative transmittance of the 10.18 μm R(18) transition reached a minimum and then increased significantly as the MMH was oxidized, while that of the 9.28 μm R(18) radiation continued to decrease slowly. Apparently the oxidation product of MMH is more absorbing at the R(18) frequency than MMH itself. As a result, the differential-absorption of the two lines reduced to zero after about 14 min and then reversed sign.

To ascertain if ammonia, which is a known minor oxidation product of MMH,[12,21] might be the source of the continued absorption of the 9.28-μm R(18) line in Fig. 17, a similar experiment was performed with the 9.29-μm R(16) line substituted for the R(18) transition; the ammonia absorption coefficient at the R(16) transition frequency is over two orders of magnitude greater than at the R(18) frequency. The effective absorption of the MMH product at the R(16) frequency obtained 30 min after insertion of MMH into the absorption cell was found to be only 10% greater than the value obtained with the R(18) frequency. Ammonia can therefore be eliminated as the molecule primarily responsible for the continued decrease of the R(18) transmittance.

Methanol is another known product of MMH decomposition with absorption in the 9-10 μm region of the spectrum. However, this molecule can also be eliminated, as its absorption coefficient is greater at the 10.18-μm R(30) frequency than at the 9.28-μm R(18) frequency. It is possible that the particular molecule causing the effect may be one of the formaldehyde hydrazones which form the bulk of the MMH oxidation products.[12]

V. Laser Remote Sensing Measurements of Hydrazine, UDMH and MMH

Laser remote sensing measurements of hydrazine, UDMH and MMH were

carried out using the system shown in Fig. 1, with the polypropylene tank[22] set between the co-axial transmitter/detector and a 1 m x 1 m flame-sprayed aluminum target which was located 2.7 km distant and served as a diffuse target.

For these experiments, both the tank and the laboratory cell were initially filled with nitrogen gas, and simultaneous measurements were made of the normalized LIDAR returns and of the laser radiation transmitted through the cell. After averaging 1000 pulses to establish the 100% transmittance level, a known amount of a hydrazine compound was inserted into the cell and, as previously described, average relative transmittance levels were taken after a pre-set number of pulses from each laser. These measurements were carried out with the hydrazine compounds in an inert nitrogen atmosphere; therefore the results could be and were used to determine the absorption coefficients of the compounds at the measurement frequencies.

Shortly after inserting a hydrazine compound into the cell, a larger amount of the same compound was inserted into the nitrogen-filled tank. The results of the simultaneous cell transmittance and LIDAR measurements are discussed below for each of the hydrazine compounds in turn.

A. Hydrazine

The relative transmittance of the 10.61 μm P(22) and the 10.68 μm P(28) radiation through the nitrogen-filled cell after inserting 1.6 μℓ hydrazine is shown as a function of time in Fig. 5a. The normalized LIDAR returns obtained simultaneously are given in Fig. 5b. The LIDAR data shown was obtained after the insertion of 0.8 ml hydrazine into the nitrogen-filled tank. The lengthiness of the run was necessitated by the slow evaporation rate of the hydrazine in the tank; some liquid was present until almost 90 minutes after insertion. Each point shown during the initial period represents the average value of 500 pulses; this was increased to a 1500 pulse average and finally to a 3000 pulse average. The minimum relative transmittance values shown in Fig. 5a correspond to absorption coefficients of 4.77 and 2.06 $(cm\text{-}atm)^{-1}$ for the P(22) and P(28)

transition frequencies respectively. These results are in reasonable agreement with the respective published values[10] of 5.41 and 2.17 $(cm\text{-}atm)^{-1}$.

The most notable feature of the experimental results as seen in Figs. 5a and 5b is the marked contrast between the smooth variation of transmitted radiation through the laboratory cell and the large amount of scatter in the LIDAR returns. This effect was observed with all the hydrazine compounds. The deviations from a smooth line of the points shown in Fig. 5a of relative transmittance through the laboratory cell were generally less than 1% and approached the 0.1% digital quantization error of the data acquisition system.

The normalized standard deviation of the LIDAR 1 P(28) return from the smooth line shown in Fig. 5b was about 5% while the corresponding value for the LIDAR 2 P(22) return was approximately 2.5%. The difference may have been due to electronic effects or to differences in the pointing accuracy of the two laser systems.

It should be noted that the corresponding points for the relative transmittance through the laboratory cell in Fig. 5a and the LIDAR returns through the large tank given in Fig. 5b are based on the same set of laser pulses and identical normalization factors. Therefore, the larger deviations observed from the LIDAR returns must arise from effects occurring outside the confines of the laboratory. These are presumably due to a combination of laser beam properties and atmospheric effects. These deviations are the major factor limiting the sensitivity of our concentration measurements. The nature of these limitations and a general discussion of error sources is given more fully in Section VI.

B. UDMH

Similar sets of measurements, obtained after inserting 5.55 μℓ UDMH into the cell and 1.95 mℓ into the tank, are given in Figs. 6a and 6b. The initial set of points are based on 200-pulse averages, followed by 500- and 1000-pulse averages as indicated. The temporal behavior of the transmittance curve through the nitrogen-filled cell is seen to be similar to that shown in Fig. 3, where an air-filled cell was used. The stable level of relative transmittance obtained with the nitrogen-filled cell correspond to absorption coefficients of 2.22 and 0.18 $(cm\text{-}atm)^{-1}$ for the 10.7 μm P(30)

and 10.3 μm R(10) CO_2 laser transitions respectively. These values are in excellent agreement with the results obtained with the air-filled cell, as given in Fig. 3. However, they are significantly higher than the respective values of 1.45 and 0.05 $(cm\text{-}atm)^{-1}$ obtained by Loper et al.[10]

The LIDAR returns did not show an abrupt change after insertion of UDMH into the tank such as was seen in the cell. This was due to the longer time required to evaporate the larger quantity of UDMH liquid and for the vapors to be dispersed throughout the tank volume. The scatter in these LIDAR returns were also on the order of 5%.

C. MMH

The corresponding curves for monomethylhydrazine, obtained after inserting 6.3 μℓ MMH into the cell and 1.55 mℓ into the tank are given in Figs. 7a and 7b. The absorption coefficients based on the results shown in Fig. 7a are 1.69 and 0.31 for the 10.18 μm R(30) and the 9.28 μm R(18) transitions respectively, which are slightly higher than the corresponding values of 1.36 and 0.23 given by Loper et al.[10] The LIDAR return scatter is again seen to be large, with an average 4-5% deviation from a smooth curve.

The experimental results shown in Figs. 5b, 6b and 7b clearly demonstrate the ability of the dual-laser DIAL system to monitor the presence of hydrazine and its derivative compounds by remote sensing over a range of 2.7 km. Using the absorption coefficients in the laboratory absorption cell simultaneously with the LIDAR measurements, the LIDAR results indicated maximum vapor levels in the tank corresponding to concentrations of approximately 1500 ppm of hydrazine and UDMH and a concentration of 3000 ppm MMH. These values are about 20% low for hydrazine and UDMH, and about 40% high for MMH, relative to the amounts predicted on the basis of the liquid volume inserted. These results are not unreasonable in view of the uncertainties in the absolute vapor concentration within the tank. The uncertainties include possible error in the syringe reading, the possible presence of oxygen in the tank due to incomplete evacuation of air from the tank prior to insertion of the liquid and to leakage thereafter, and stratification of the vapor after evaporation. The latter effect was almost certainly the major source of the large excess absorption observed for MMH, as the "flapper" used to prevent stratification was not operational during the MMH experiment.

VI. Analysis of DIAL Sensitivity of the Hydrazine Compounds

The ability of the dual-laser DIAL system to detect the presence of the hydrazine compounds for a LIDAR range of 2.7 km was established by the experimental results described in the preceding section. These results can be used to determine the limits of sensitivity with which such measurements can be made at other detection ranges; that is, to establish the minimum path-averaged detectable concentration, n_{min}, of a trace species as a function of detection range, R.

There are two common approaches taken to evaluate n_{min}. At long ranges the limitation is generally established by setting the difference in the back-scattered return at the two frequencies equal to the noise of the detector. At shorter ranges, a more restrictive limitation may occur due to the inability of the signal processing system to distinguish changes in the normalized return signals, $\Delta P_r = P_r(\lambda_1) - P_r(\lambda_2)$, at the two frequencies, λ_1 and λ_2, below some predetermined value. The effects of both limitations on the detection sensitivity of molecular pollutants have been discussed previously.[4] For the case in which the difference in the return signals, ΔP_r, due to the differential-absorption of the absorbing species is set equal to the noise equivalent power of the detector (NEP), it was shown that

$$n_{min} = \frac{(NEP)\,\pi\, R}{2K\rho A\, P_o\, (\Delta\sigma) \exp(-2\beta R)} \qquad (1)$$

where K is the receiver efficiency, ρ is the reflectivity of the topographic target, A is the area of the receiving telescope, P_o is the output power of the laser beam, $\exp(-2\beta R)$ is the atmospheric attenuation and $\Delta\sigma$ is the difference in the absorption coefficients of the pollutant at the two wavelengths [$\Delta\sigma = \sigma(\lambda_2) - \sigma(\lambda_1)$]. The values taken to evaluate Eq. (1) for our DIAL system are: $P_o = 10^5$ W, A = 500 cm^2, (NEP) = 2 x 10^{-8} W, K = 0.1 and ρ = 0.1. Then, expressing n_{min} in parts per billion

$$n_{min}\,(ppb) = \frac{5.2\, R}{(\Delta\sigma) \exp(-2\beta R)} \qquad (2)$$

where the units are R(km), $\beta(km^{-1})$ and $\Delta\sigma(cm\text{-}atm)^{-1}$.

The values of n_{min} as a function of R have been evaluated on the basis of Eq. (2) for hydrazine, UDMH and MMH using our experimentally determined values of $\Delta\sigma$ and the U. S. Standard atmosphere absorption coefficients of β as given in Table I. The results are shown by the curves of Figs. 8, 9 and 10 labeled NEP limited. They represent the ultimate sensitivity of the instrumentation and determine the maximum achievable range for a given pulse energy level.

At shorter ranges a more restrictive limitation than that given in Eq. (2) may occur due to the inability of the measurement system to distinguish between the fractional change in the LIDAR return signal, $(\Delta P_r/P_r)$, due to real variations of the species concentrations and random fluctuations caused by atmospheric turbulence and other perturbations. For this case it may be shown[4] that

$$n_{min} = \frac{5 \times 10^3 (\Delta P_r/P_r)}{(\Delta\sigma)\, R} \qquad (3)$$

The smallest distinguishable value of $\Delta P_r/P_r$ in Eq. (3) must be at least as great as the fluctuations of the LIDAR returns around a "best-fit" smooth curve. A measure of these fluctuations is their standard deviation, σ_I, which may be taken as the lower limit of the value of $\Delta P_r/P_r$ in Eq. (3). On the basis of the laser remote sensing data presented in Section V, a pulse-averaged value for σ_I of approximately 0.05 was obtained at a range of 2.7 km. As seen in Figs. 5, 6 and 7, little significant improvement in σ_I was observed as the number of pulses averaged was increased from a few hundred up to 3000 pulses.

In general, the value of $\Delta P_r/P_r$ in Eq. (3) may be a function of both the DIAL system parameters and atmospheric effects. It is therefore reasonable to assume that $\Delta P_r/P_r$ will contain both a constant term and a range-dependent term. The value of the constant term contained within $\Delta P_r/P_r$ may be ascertained from short-range DIAL measurements as well as those obtained from laboratory measurements, which represents the limiting case of $R \approx 0$. Our measurements indicate that a conservative estimate of the value of the

constant term for our present DIAL system, $(\Delta P_r/P_r)_{min}$, is on the order of 0.01. The limitation due to this term alone corresponds to the dashed line labeled 1% in Figs. 8, 9, and 10.

The range-dependent contribution to $\Delta P_r/P_r$ arises from atmospheric turbulence effects. Although the atmosphere is effectively 'frozen' during the 50 μs delay between laser firings of our dual-laser DIAL system, the influence of atmospheric turbulence is significantly reduced only when the temporal correlation coefficient of these signals on a pulse-to-pulse basis is equal to or near unity. It has been found[13] that system noise caused by electronic noise, pulse-to-pulse directional shifts of the laser beams and changes in beam quality can give rise to a decorrelation effect which is comparable to the turbulence-induced correlation for LIDAR returns from a diffuse target. This is also the case in our hydrazine experiments, where we have obtained temporal correlation values of less than 0.5 from the LIDAR signal returns from lasers 1 and 2 on a pulse-to-pulse basis. In view of the above decorrelating processes, the effects of atmospheric turbulence can be reduced, but not eliminated.

The range dependence of atmospheric turbulence effects is quite strong. According to the Rytov formula,[23] atmospheric turbulence leads to a value for the log-amplitude variance, σ_χ^2 which is strongly range-dependent, as

$$\sigma_\chi^2 = 0.124\ C_n^2\ k^{7/6}\ R^{11/6} \qquad (4)$$

where C_n^2 is the refractive-index structure parameter, k is the wave vector $2\pi/\lambda$, and the numerical factor is dependent upon the nature of the wave source. For a log-normal distribution the measured normalized variance σ_I^2 of the LIDAR returns is related to σ_χ^2 according to the equation $\sigma_I^2 = \exp(4\sigma_\chi^2)-1$. For the moderate turbulence levels indicated by the measured variance values in our experiment, $\sigma_I^2 \ll 1$, the range dependence of σ_I^2 to lowest order will be the same as that of σ_χ^2; that is, $\sigma_I^2 \propto R^{11/6}$. Under these conditions, if the minimum range-dependent contribution of $(\Delta P_r/P_r)$ in Eq. (3) is taken as totally due to atmospheric fluctuations, and hence proportional to σ_I, the contribution to n_{min} has the form

$$n_{min} \propto \frac{R^{11/12}}{(\Delta\sigma)\,R} \propto \frac{R^{-1/12}}{\Delta\sigma} \quad . \tag{5}$$

Equation (5) can be expected to overemphasize the effect of atmospheric turbulence on the range dependence of statistical deviations in our measurements since it ignores reductions due to saturation and aperture averaging effects. However, pending a direct experimental determination of the range dependence of $\Delta P_r/P_r$, a reasonable first approximation assumes that n_{min} is simply the sum of the range-independent $\Delta P_r/P_r$ term of the form of Eq. (3) and a range-dependent $\Delta P_r/P_r$ term of the form of Eq. (5). Then,

$$n_{min} = \frac{1}{\Delta\sigma}\left[\frac{5 \times 10^3\,(\Delta P_r/P_r)_{min}}{R} + CR^{-1/12}\right] \tag{6}$$

where C is a constant to be determined experimentally and, as noted previously, $(\Delta P_r/P_r)_{min}$ is the minimum value of $(\Delta P_r/P_r)$, independent of range, and taken equal to 0.01. To evaluate C, the value for n_{min} in Eq. (3) for $(\Delta P_r/P_r) = 0.05$ and R=2.7 km is taken as a normalization point on the basis of the experimental measurements given in the previous section. Using this value for n_{min} in Eq. (6), one obtains C = 80.5. This value was then used in Eq. (6) to generate the curves labeled Eq. (6) in Figs. 8, 9, and 10. It is seen that, at the shortest ranges, n_{min} asymptotically approaches the ultimate system sensitivity, which is assumed equal to 1% in our calculations. As the range increases, the contribution of the second term on the right hand side of Eq. (6), which is almost independent of range, assumes greater relative importance.

The resultant predictions shown in Figs. 8, 9, and 10 indicate that path-averaged concentrations of the order of 35, 45 and 70 parts per billion over a range of 2.7 km should be observable for hydrazine, UDMH and MMH respectively under the conditions of our experiment.

VII. Analysis of Effects of Atmospheric Fluctuations and Signal Averaging on DIAL Sensitivity

The experimental and theoretical results presented in the previous two sections indicate that fluctuations due to atmospheric effects play a dominant role in limiting the sensitivity of our DIAL system for the remote sensing of the hydrazine compounds at intermediate ranges ($0.5 < R < 3$ km). The results in Figs. 5b, 6b and 7b further indicated that increasing the number of pulses averaged above a few hundred yielded relatively small reduction in the magnitude of the fluctuations, which indicates that these fluctuations are primarily due to atmospheric variations occurring over the time required to obtain the additional pulse returns.

In view of the importance of these atmospheric fluctuations in limiting the sensitivity of our measurements, a study was made to directly measure the improvement achievable by averaging over increasing numbers of pulses, and to establish the role of long-term versus short-term atmospheric fluctuations in setting the limits of measurement accuracy.

To accomplish this, laser 1 was fired on the P(28) line and 50 μs later laser 2 was fired on the P(22) line, as was the case for our hydrazine absorption measurements. The target remained the flame-sprayed aluminum plate at R = 2.7 km. However, the large tank was removed from the laser beam path; therefore, only atmospheric absorption was involved in the measurements.

A total of 22528 normalized LIDAR return pulses from each of the dual lasers was recorded for later statistical analysis. The entire process, including the time required to print out a preliminary real-time analysis after every 2048 pulses, took 40 minutes, corresponding to an overall pulse repetition rate of slightly under 10 Hz. The real-time analysis also established that the pulse-pair temporal correlation[13] of the normalized LIDAR returns from the corresponding pulses of laser 1 to laser 2 was approximately 0.3. Due to computational constraints, analysis was limited to blocks of 12288 pulses from each laser. The following discussion will analyze the data from both the first block of 12288 pulses and the final block of 12288 pulses, as they exhibited somewhat differing behavior.

The analyses included determination of the average values of the full block of pulses and of smaller sections of that block and a determination of the normalized standard deviation, σ, of the LIDAR returns as a function of N, the number of pulses being averaged in each section.

The standard deviation was measured as a function of N using a segmental averaging approach. As an example, for N=8 the segments averaged would be pulses 1-8, 9-16, 17-24,----12281-12288, and the measured standard deviation is based on the resultant 12288/N average values. This was the method used in our real-time determinations of standard deviation. The results obtained for the block containing the first 12288 pulses from both laser 1, L_1, and laser 2, L_2, are given in Table II, which shows the percentage standard deviation of the normalized LIDAR returns as N is increased from 1 to 2048 by factors of 2. Table II also shows the standard deviation using the ratio of the returns from the two lasers on a pulse-pair basis. There is no observable reduction in the standard deviation using the ratios, which is consistent with the fact that the measured temporal correlation coefficients between the individual laser pulses was less than 0.5.[4,24]

The standard deviation of the LIDAR returns obtained for N = 2048 was fully an order of magnitude greater than the standard deviation values of 0.22% and 0.25% obtained from the normalized laser 1 and 2 pulses respectively after passage through the laboratory cell containing air at atmospheric pressure. The standard deviation vs N was also calculated using a running average approach. Very little difference between the two averaging methods was observed for all values of N, with the results essentially identical for $N < 256$.

The variation of the segmental standard deviations of the returns from lasers 1 and 2 as a function of N is shown graphically in Fig. 11a. It is seen that the slope is significantly smaller than the predicted $N^{-1/2}$ dependence. This is presumably due to the fact that the atmospheric absorption being measured is varying significantly over time periods of the order

of or shorter than the measurement period. These changes in atmospheric absorption also provide a lower limit to the standard deviation achievable for large values of N.

To illustrate the extent of the variation in average value from segment to segment, the average value (normalized to unity over the complete block) is shown in Fig. 11b for the twenty-four N = 512 pulse segments. Each segment represents the average value over a time interval of slightly under one minute. From Table II, the results correspond to standard deviations of approximately 3.0 and 3.9% for the laser 1 and 2 returns respectively. Individual deviations from the mean as great as 10% are observed, but no long-term and large departures from the mean are observed.

The above results are in marked contrast with results obtained with the block of data containing the final 12288 pulses from both lasers. The results from the latter block are shown in Table III and Figs. 12a and 12b. Figure 12a shows that the variation of the standard deviation with N is again much slower than $N^{-1/2}$ for low N and becomes almost flat for N > 256. The results are in general accord with the results of the initial data block. However, the standard deviation values for N = 2048 of almost 7 and 5% for lasers 1 and 2 respectively are significantly higher than those obtained from the first block. The reason for the increase is apparent after considering the normalized segmental average values for this block, as shown in Fig. 12b for N = 512. It is seen that there is a slow but almost constant increase in the average value of the normalized LIDAR return segments from both lasers throughout the period encompassed by this block, corresponding to a decrease in atmospheric absorption over the 2.7 km interval at both the P(28) and P(22) CO_2 laser frequencies. That this is truly an atmospheric effect rather than an experimental artifact is indicated by the standard deviation values of 0.38 and 0.34% obtained from the corresponding normalized pulses from lasers 1 and 2 respectively in our simultaneous laboratory measurement through the air-filled cell.

A particularly important feature of the results shown in Table III and Fig. 12a is that the standard deviation of the ratios of the pulse-pair

laser returns, $\sigma_{L1/L2}$ as a function of N, closely resembles the values of the equivalent set, as given in Table II. This is in spite of the difference in the values for the individual lasers, σ_{L1} and σ_{L2}, and despite the small value (< 0.5) of the temporal correlation coefficient as measured on a pulse-to-pulse basis.

The reduction in the standard deviation values using the ratio L1/L2 relative to the values for the individual lasers occurs because the observed decrease in the atmospheric background absorption is slow compared to the measurement time of the individual segments. Under these circumstances, one can consider the temporal correlation of the segmental measurements relative to the average value of the full set. This is illustrated for the case N = 512 in Fig. 12b, where the measurement time was slightly under one minute. For the values shown in Fig. 12b, one obtains $\rho_s = 0.9$, where ρ_s is the correlation coefficient of the corresponding segments of the returns from lasers 1 and 2. Using this value and the values of σ_{L1} and σ_{L2} given in Table III for N = 512 in the equation[24]

$$\sigma^2_{L1/L2} = \sigma^2_{L1} + \sigma^2_{L2} - 2\rho_s\sigma_{L1}\sigma_{L2} \qquad (7)$$

leads to the calculated value $\sigma_{L1/L2}$ (calc) = 3.25%, which is in good agreement with the measured value $\sigma_{L1/L2}$ (meas) = 3.45%, as given in Table III. It is apparent that the use of the LIDAR return ratios from equivalent segments of a dual laser system can effectively eliminate much of the uncertainties due to slow drifts in atmospheric absorption when, as in this instance, the background absorption of the atmosphere is similar at the two laser frequencies.

The above analysis indicates that increased accuracy can sometimes be achieved using LIDAR return ratios even when the pulse-to-pulse correlation coefficient is less than 0.5. In this regard, a distinction between short-term and long-term atmospheric fluctuations must be made, since the

use of ratios can only be effective when the measurement time is short relative to the temporal variation of the atmosphere. The short term fluctuations occur in the order of 5-100 ms,[13] and significant improvements relative to these atmospheric changes occur only if the pulse-to-pulse correlation coefficient, ρ, of the normalized LIDAR returns from the closely spaced ($\sim$ 50 μs) dual-laser outputs is greater than 0.5.[24] For topographic target reflection, ρ is frequently near or below this value;[13] this was the case in our measurements, where $\rho \approx 0.3$. Thus, the use of LIDAR return ratios was not effective in eliminating the effect of short-term variations. However, our experiments have shown that when long-term atmospheric shifts are superimposed on short term effects, the use of dual-laser LIDAR return ratios can effectively reduce the standard deviation to values approaching those due to the rapid atmospheric fluctuation effects. Under the conditions of our experiments, as given in Table III, the use of ratios led to a reduction of the standard deviation from over 6% to approximately 2.5% after averaging over the order of 2000 pulses in a 3.5 minute interval.

It should be noted that the above analysis should be relevant to the hydrazine detection results presented in Section VI since the level of fluctuations observed with and without the hydrazine tank were essentially the same. It then follows that using a dual-laser DIAL system for the remote sensing of hydrazine compounds can be effective in reducing measurement uncertainties due to long-term atmospheric drifts.

VIII. Conclusions

In this paper we have experimentally demonstrated the capability of a dual-CO_2 laser differential-absorption LIDAR system to detect hydrazine, UDMH and MMH over distances approaching 3 km. In addition, the ability of the dual-laser DIAL system to follow the changes in the concentration of these species was also shown.

The sensitivity with which the concentration of these compounds could be measured was found to be limited by the minimum change in the differential-absorption LIDAR return, $\Delta P_r/P_r$, which could be distinguished from background fluctuations due to atmospheric turbulence effects. Therefore,

$\Delta P_r/P_r$ is itself range dependent. An equation expressing this dependence was derived and used to predict the minimum concentrations of the hydrazine molecules which our DIAL system could measure as a function of range. Our results indicate that even with conservative assumptions the presence of hydrazine, UDMH and MMH can be remotely detected using LIDAR returns from a topographic target with a sensitivity on the order of 100 ppb or better between 0.5 and 5 km.

REFERENCES

1. T. Henningsen, M. Garbuny, and R. L. Byer, Appl. Phys. Lett. 24, 242 (1974).
2. D. K. Killinger, N. Menyuk, and W. E. DeFeo, Appl. Phys. Lett. 36, 402 (1980).
3. E. R. Murray and J. E. van der Laan, Appl. Opt. 17, 814 (1978).
4. D. K. Killinger and N. Menyuk, IEEE J. Quantum Electron. QE-17, 1917 (1981).
5. N. Menyuk, D. K. Killinger, and W. E. DeFeo, Appl. Opt. 19, 3282 (1980).
6. R. A. Baumgartner and R. L. Byer, Opt. Lett. 2, 163 (1978).
7. K. Asai, T. Itabe, and T. Igarashi, Appl. Phys. Lett. 35, 60 (1979).
8. E. R. Murray, Opt. Eng. 17, 30 (1978).
9. H. W. Schiessl, "Hydrazine and Its Derivatives"in Kirk-Othmer: Encyclopedia of Chemical Technology, Vol. 12, 3rd Edition, (John Wiley & Sons, Inc., New York, 1980).
10. G. L. Loper, A. R. Calloway, M. A. Stamps, and J. A. Gelbwachs, Appl. Opt. 19, 2726 (1980).
11. J. N. Pitts, Jr., E. C. Tuazon, W. P. Carter, A. M. Winer, G. W. Harris, R. Atkinson, and R. A. Graham, "Atmospheric Chemistry of Hydrazines: Gas Phase Kinetics and Mechanistic Studies", Report No. ESL-TR-80-39, August 1980.
12. D. A. Stone, "The Autoxidation of Hydrazine Vapor", CEEDO-TR-78-17, January 1978, and "The Autoxidation of Monomethylhydrazine Vapor", CEEDO-TR-79-10, April 1979.
13. N. Menyuk and D. K. Killinger, Opt. Lett. 6, 301 (1981).
14. N. Menyuk and P. F. Moulton, Rev. Sci. Instrum. 51, 216 (1980).
15. R. A. McClatchey, R. W. Fenn, J. E. A. Selby, F. E. Volz, and J. S. Garing, "Optical Properties of the Atmosphere (Third Edition)", Report AFCRL-72-0497, Environmental Research Paper No. 411 (1972).
16. R. J. Brewer and C. W. Bruce, Appl. Opt. 17, 3746 (1978).
17. R. R. Patty, G. M. Russwurm, W. A. McClenny, and D. R. Morgan, Appl. Opt. 13, 2850 (1974).

18. S. T. Hong and A. Ishimaru, Radio Sci. 11, 551 (1976).
19. A. G. Kjelaas, P. E. Nordal, and A. Bjerkestrand, Appl. Opt. 17, 277 (1978).
20. G. L. Loper, "Gas Phase Kinetic Study of Air Oxidation of UDMH", in Proceedings, Conference on Environmental Chemistry of Hydrazine Fuels, Tyndall Air Force Base, CEEDO-TR-78-14, p. 129 (13 September 1977).
21. R. A. Saunders and J. T. Larkins, "Detection and Monitoring of Hydrazine, Monomethylhydrazine and Their Decomposition Products", NRL Memorandum Report 3313/AD-A027966 (1976).
22. To avoid confusion, the large container used for remote sensing will be referred to as a tank. The term cell will be reserved for the smaller Pyrex container used in the laboratory absorption measurements.
23. R. E. Hufnagel, "Propagation Through Atmospheric Turbulence", chapter 6 in The Infrared Handbook, W. L. Wolfe and G. J. Zissis, Eds., Office of Naval Research, Washington, D.C. (1978).
24. D. K. Killinger and N. Menyuk, Appl. Phys. Lett. 38, 968 (1981).

TABLE I

RELEVANT ABSORPTION PARAMETERS FOR THE REMOTE SENSING OF THE HYDRAZINES

CO_2 Laser Transition	Wavelength (μm)	Absorption Coefficients $(cm\text{-}atm)^{-1}$				Atmospheric Attenuation $\beta(km)^{-1}$
		(b)	(c)	(d)	(d)	(a)
		Hydrazine		NH_3	C_2H_4	
P(22)	10.611	4.77	5.41	0.045	1.09	0.1142
P(28)	10.675	2.06	2.17	0.36	1.30	0.0976
Differential Absorption		2.71	3.24	-0.315	-0.21	
		UDMH		NH_3	C_2H_4	
P(30)	10.696	2.22	1.45	0.86	1.63	0.0907
R(10)	10.318	0.18	0.05	0.78	1.51	0.1142
Differential Absorption		2.04	1.40	0.08	0.12	
		MMH		NH_3	C_2H_4	
R(30)	10.182	1.69	1.36	0.029	0.56	0.1137
R(18)	9.282	0.31	0.23	0.13	0.61	0.1418
Differential Absorption		1.38	1.13	-0.10	-0.05	

(a) Values given for U. S. Standard Atmosphere.
(b) This work.
(c) Ref. 10.
(d) Ref. 16.

TABLE II

PERCENTAGE STANDARD DEVIATION OF NORMALIZED LIDAR RETURNS FOR THE INITIAL BLOCK OF PULSES FOR LASER 1, LASER 2 AND THE RATIO OF RETURNS VERSUS NUMBER OF PULSES AVERAGED

	STANDARD DEVIATION (PERCENT)		
	Laser 1 P(28)	Laser 2 P(22)	Ratio L1/L2
N			
1	20.5%	17.7%	22.3%
2	16.7	14.6	17.0
4	13.8	12.2	13.3
8	11.3	10.1	10.8
16	9.0	8.3	8.7
32	7.3	7.0	7.6
64	6.0	6.1	6.6
128	4.8	5.2	5.8
256	3.8	4.5	4.9
512	3.0	3.9	4.0
1024	2.7	3.3	3.3
2048	2.2	2.8	2.4

TABLE III

PERCENTAGE STANDARD DEVIATION OF NORMALIZED LIDAR RETURNS FOR THE FINAL BLOCK OF PULSES FOR LASER 1, LASER 2 AND THE RATIO OF RETURNS VERSUS NUMBER OF PULSES AVERAGED

	STANDARD DEVIATION (PERCENT)		
	Laser 1 P(28)	Laser 2 P(22)	Ratio L1/L2
N			
1	21.7%	18.3%	22.2%
2	18.0	15.2	16.8
4	15.1	12.7	12.8
8	12.8	10.7	10.0
16	10.8	9.1	7.9
32	9.5	7.8	6.4
64	8.5	7.1	5.3
128	7.9	6.6	4.5
256	7.5	6.0	3.9
512	7.3	5.8	3.4
1024	7.0	5.2	2.8
2048	6.8	4.8	2.4

C82-3699C

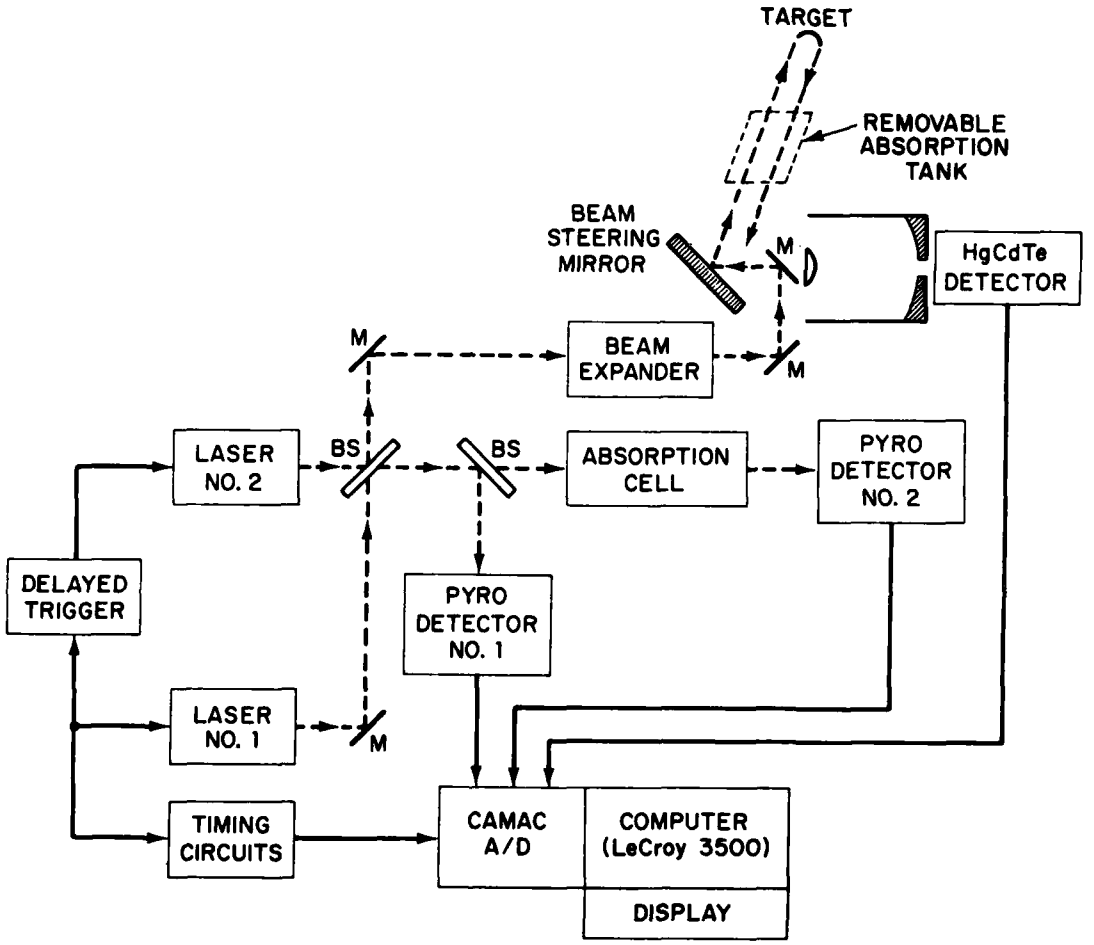

Fig. 1. Schematic of dual-laser LIDAR system used for remote sensing of hydrazine and its derivatives.

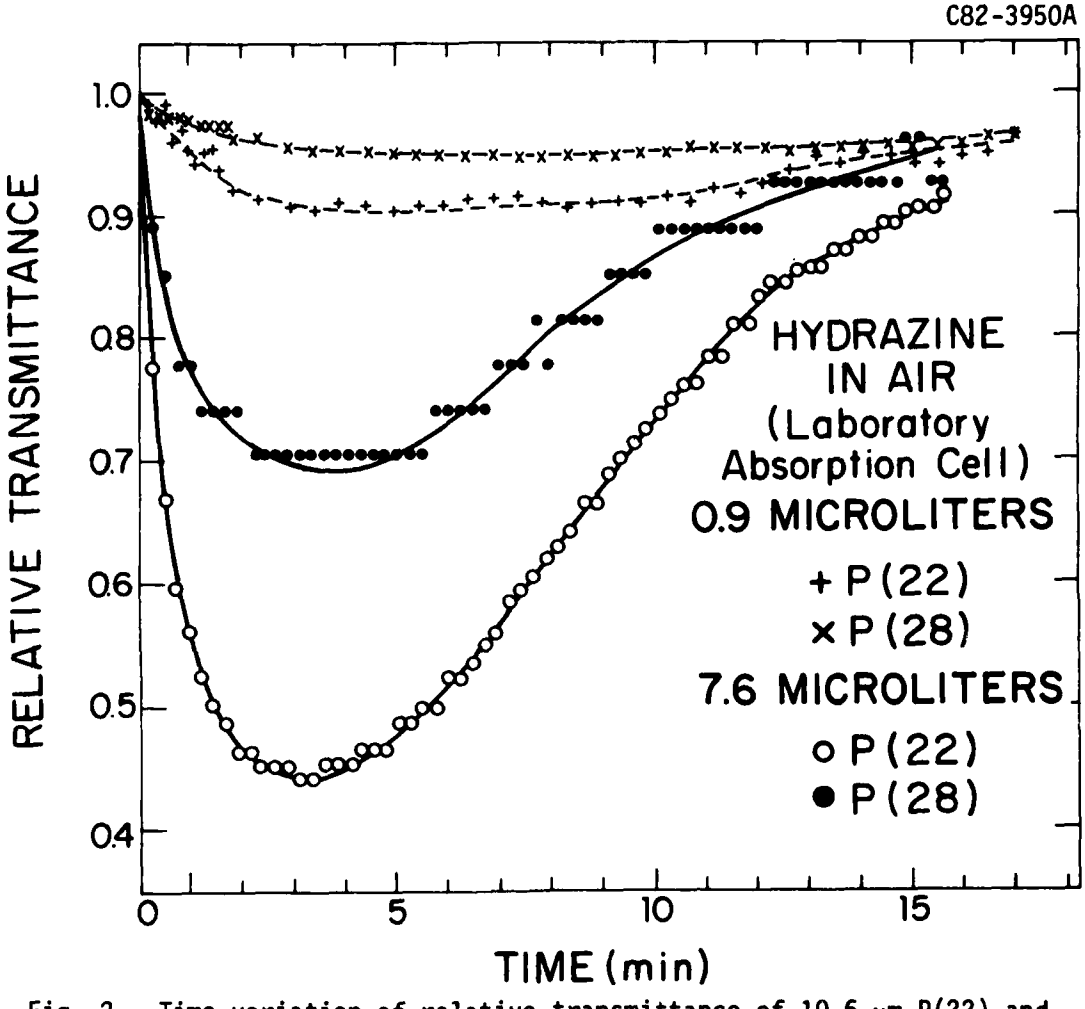

Fig. 2. Time variation of relative transmittance of 10.6-μm P(22) and 10.7-μm P(28) radiation through a 33 cm long laboratory absorption cell containing air after insertion of 0.9 μℓ and 7.6 μℓ of liquid hydrazine.

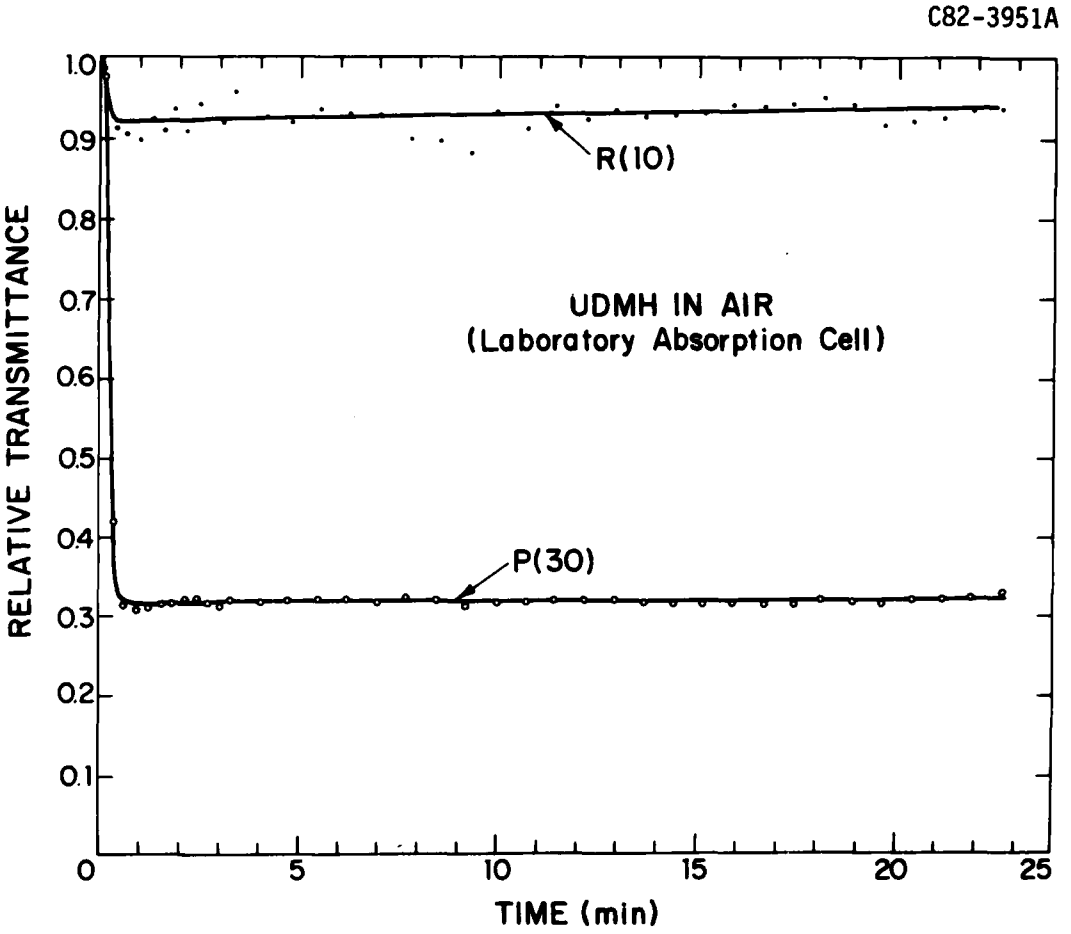

Fig. 3. Time variation of relative transmittance of 10.7-μm P(30) and 10.3-μm R(10) radiation through a laboratory absorption cell containing air after inserting 9 μℓ of liquid UDMH.

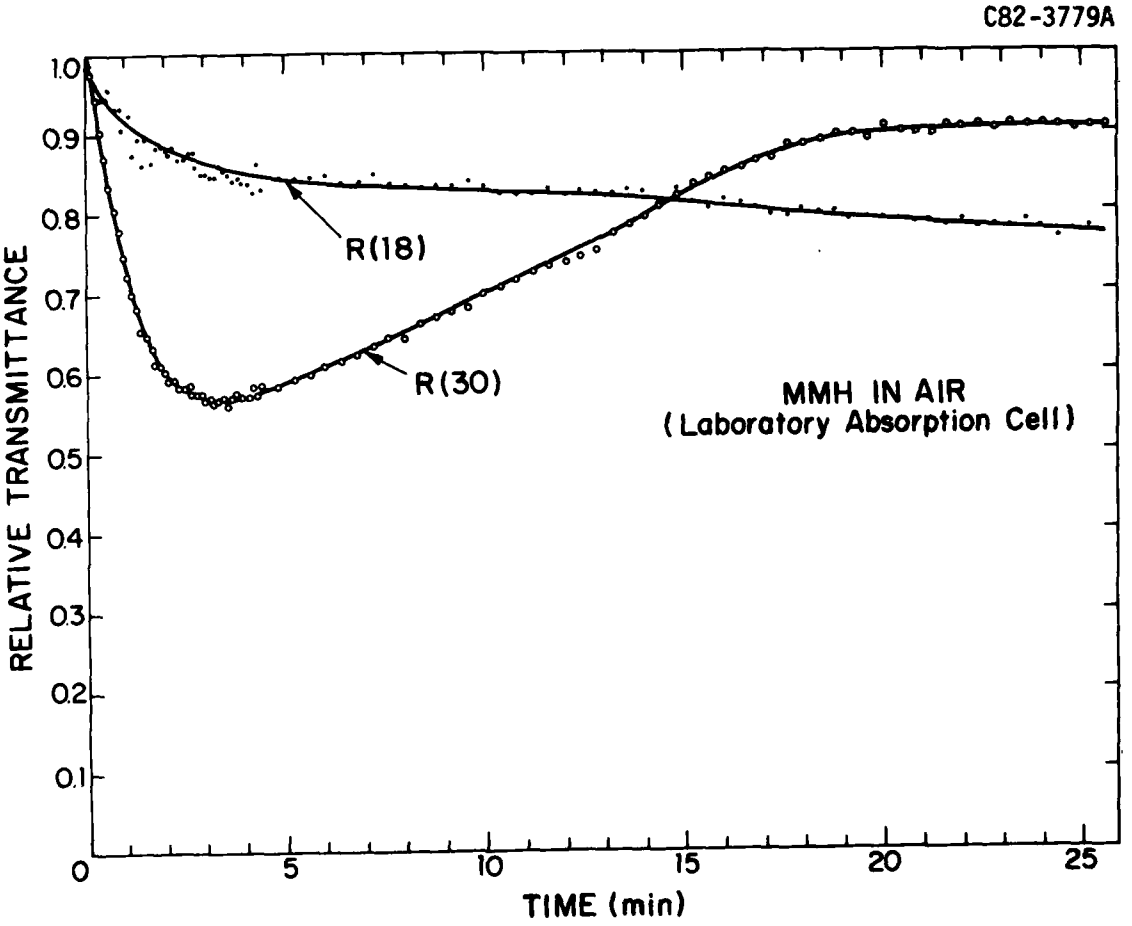

Fig. 4. Time variation of relative transmittance of 10.2-μm R(30) and 9.3-μm R(18) through a laboratory absorption cell containing air after inserting 9 μℓ of liquid MMH.

C82-3952

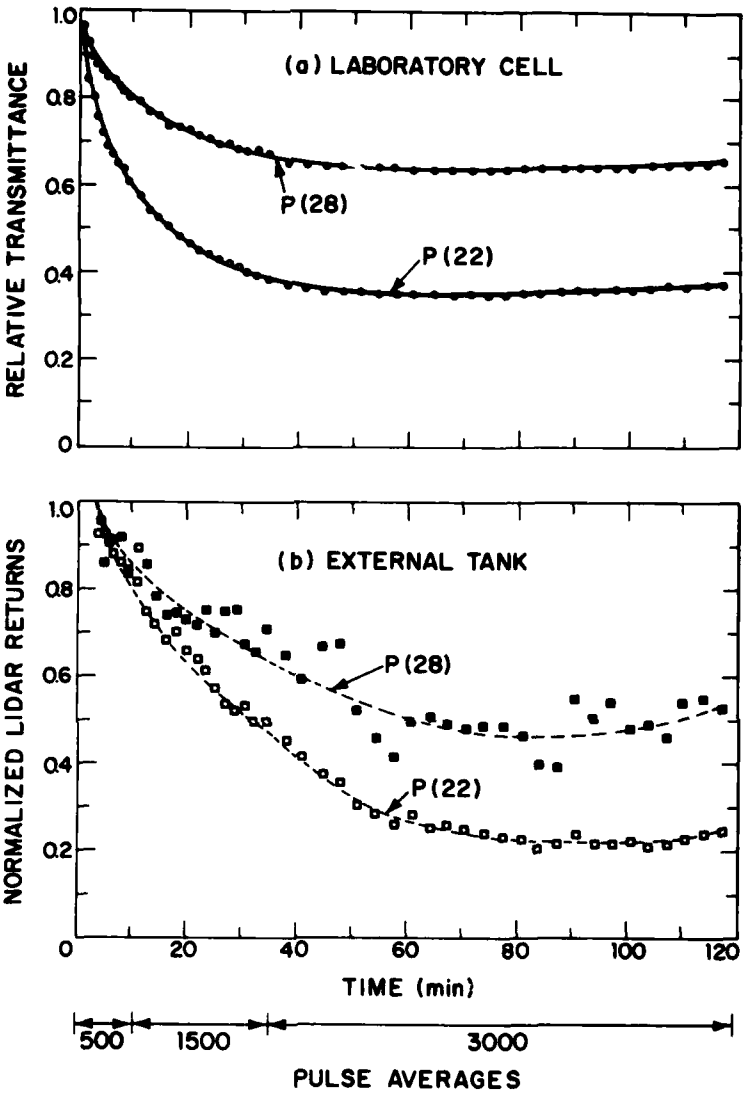

Fig. 5. Simultaneous differential-absorption measurements of hydrazine in nitrogen-filled laboratory absorption cell and tank. (a) Time variation of relative transmittance through cell after inserting 1.6 μℓ hydrazine; (b) LIDAR returns from laser pulses passing through tank and reflected from topographic target after inserting 0.8 mℓ hydrazine. The number of pulses averaged for each point is given below.

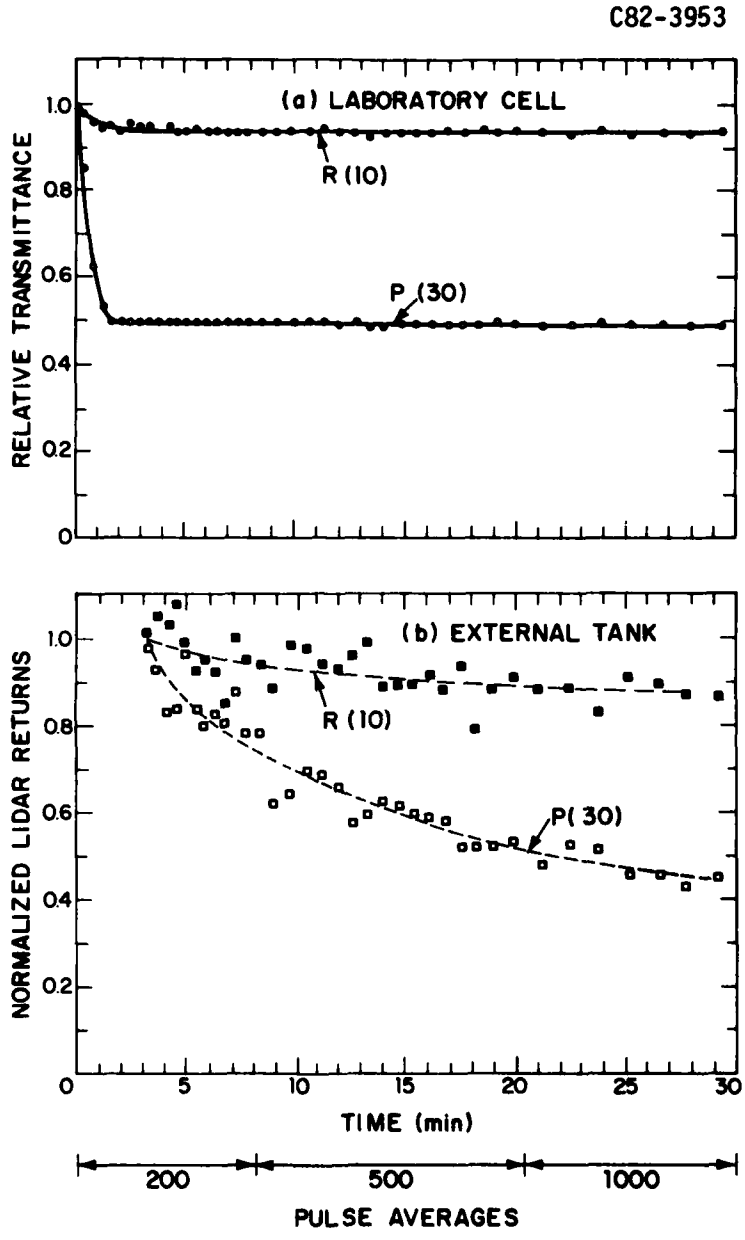

Fig. 6. Simultaneous differential-absorption measurements of UDMH in nitrogen-filled laboratory absorption cell and tank. (a) Time variation of relative transmittance through cell after inserting 5.5 μℓ UDMH: (b) LIDAR returns from laser pulses passing through tank and reflected from topographic target after inserting 1.95 mℓ UDMH.

C82-3954

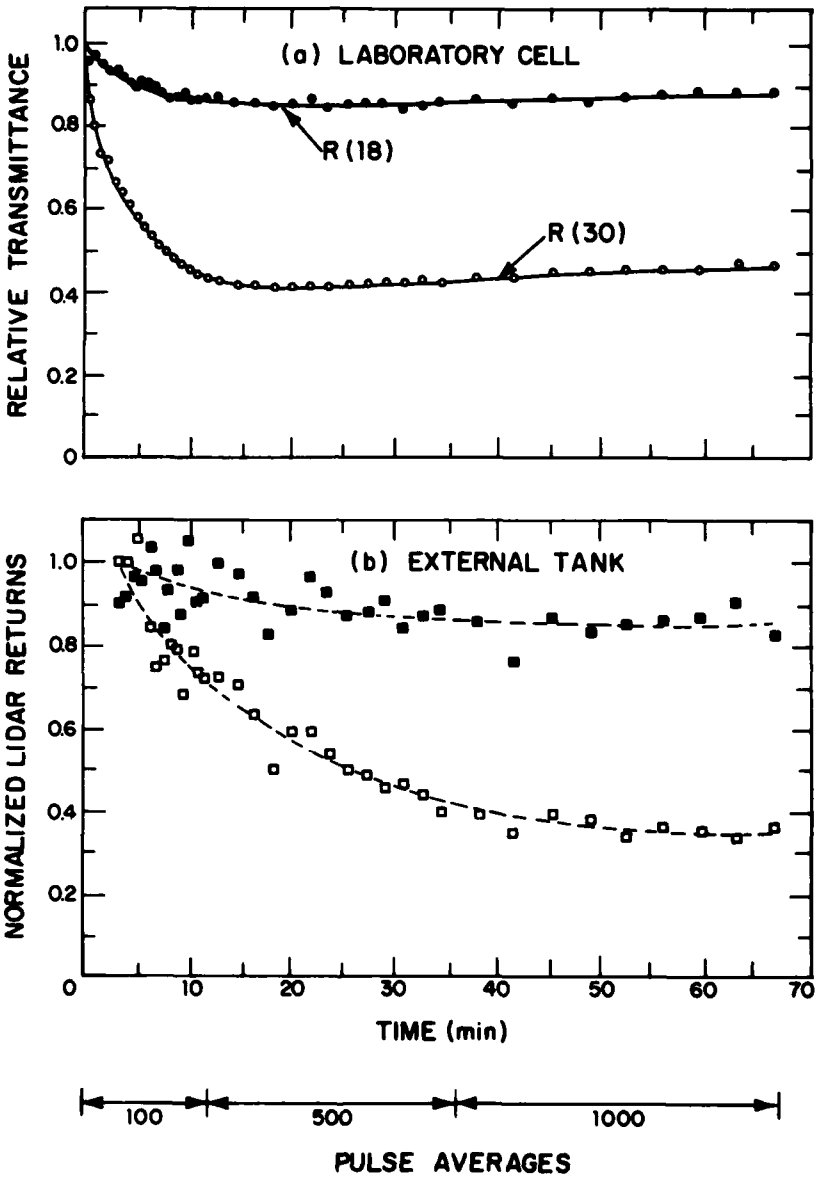

Fig. 7. Simultaneous differential-absorption measurements of MMH in nitrogen-filled laboratory absorption cell and tank. (a) Time variation of relative transmittance through cell after inserting 6.3 μℓ MMH; (b) LIDAR returns from laser pulses passing through tank and refected from topographic target after inserting 1.55 mℓ MMH.

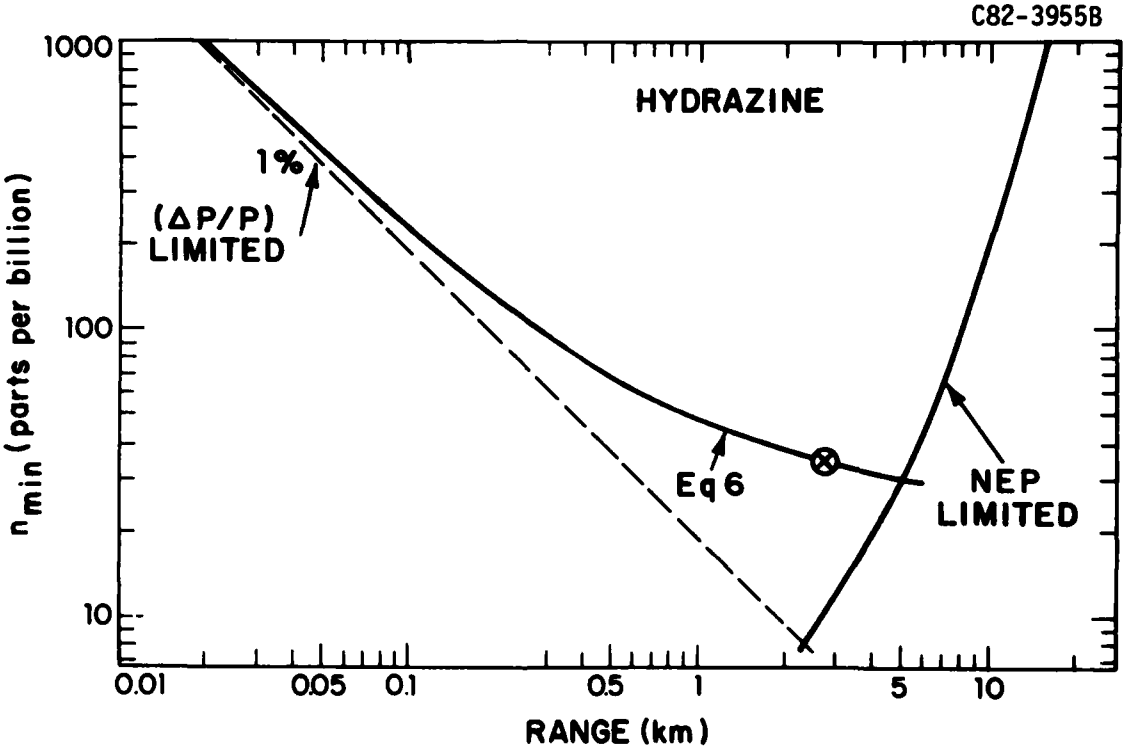

Fig. 8. Minimum detectable path-averaged hydrazine concentration by topographic reflection as a function of range. Normalization point shown is taken from the experimental results and corresponds to $\Delta P/P = 0.05$ at a range of 2.7 km.

C82-3956B

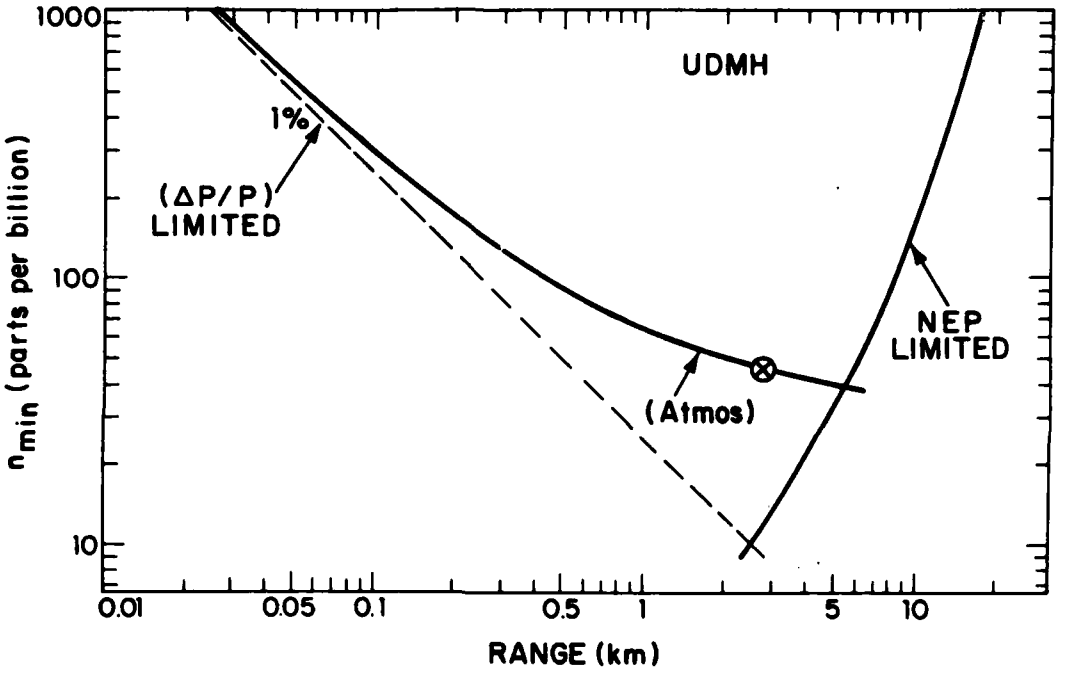

Fig. 9. Minimum detectable path-averaged UDMH concentration by topographic reflection as a function of range.

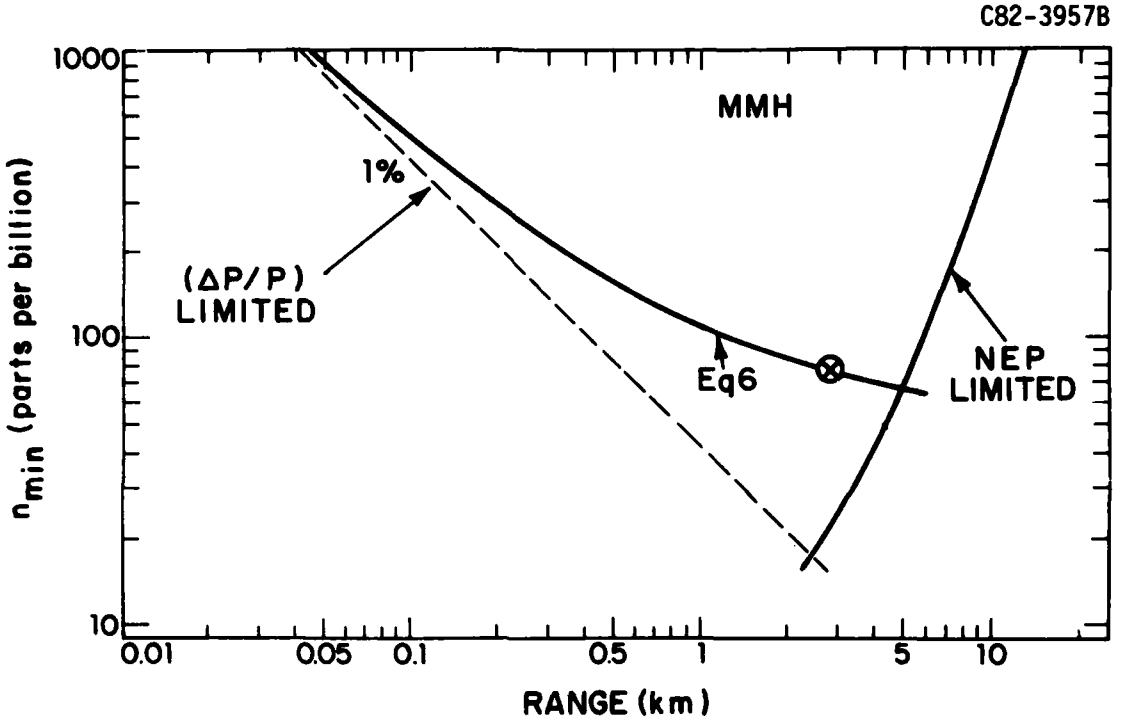

Fig. 10. Minimum detactable path-averaged MMH concentration by topographic reflection as a function of range.

C82-3958

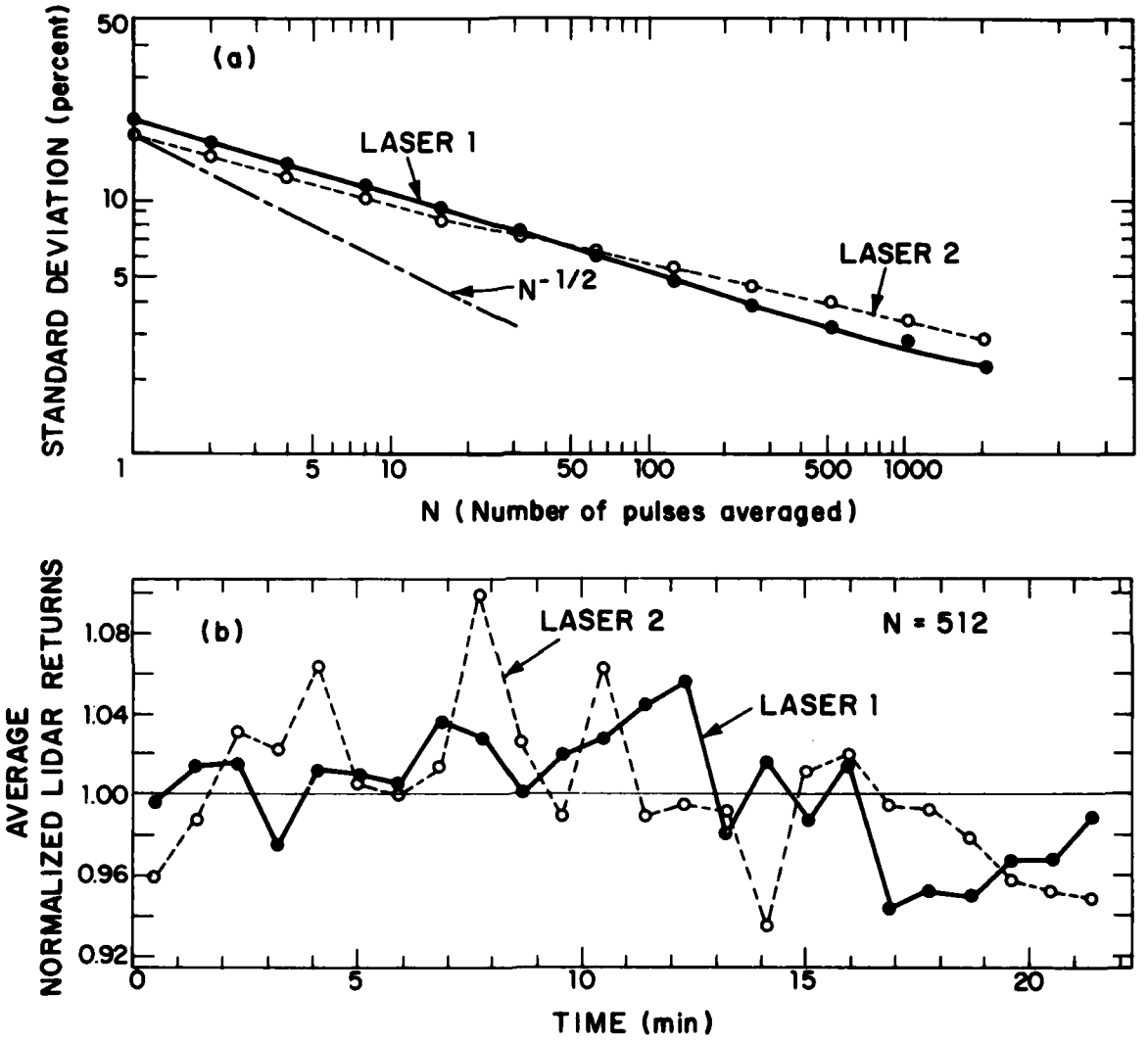

Fig. 11. Statistical analysis of segmentally averaged initial set of 12288 normalized pulses from laser 1 and 2. (a) standard deviation of the segment averages as a function of N, the number of pulses averaged per segment, (b) variation of the average value of the individual segments with time for N = 512.

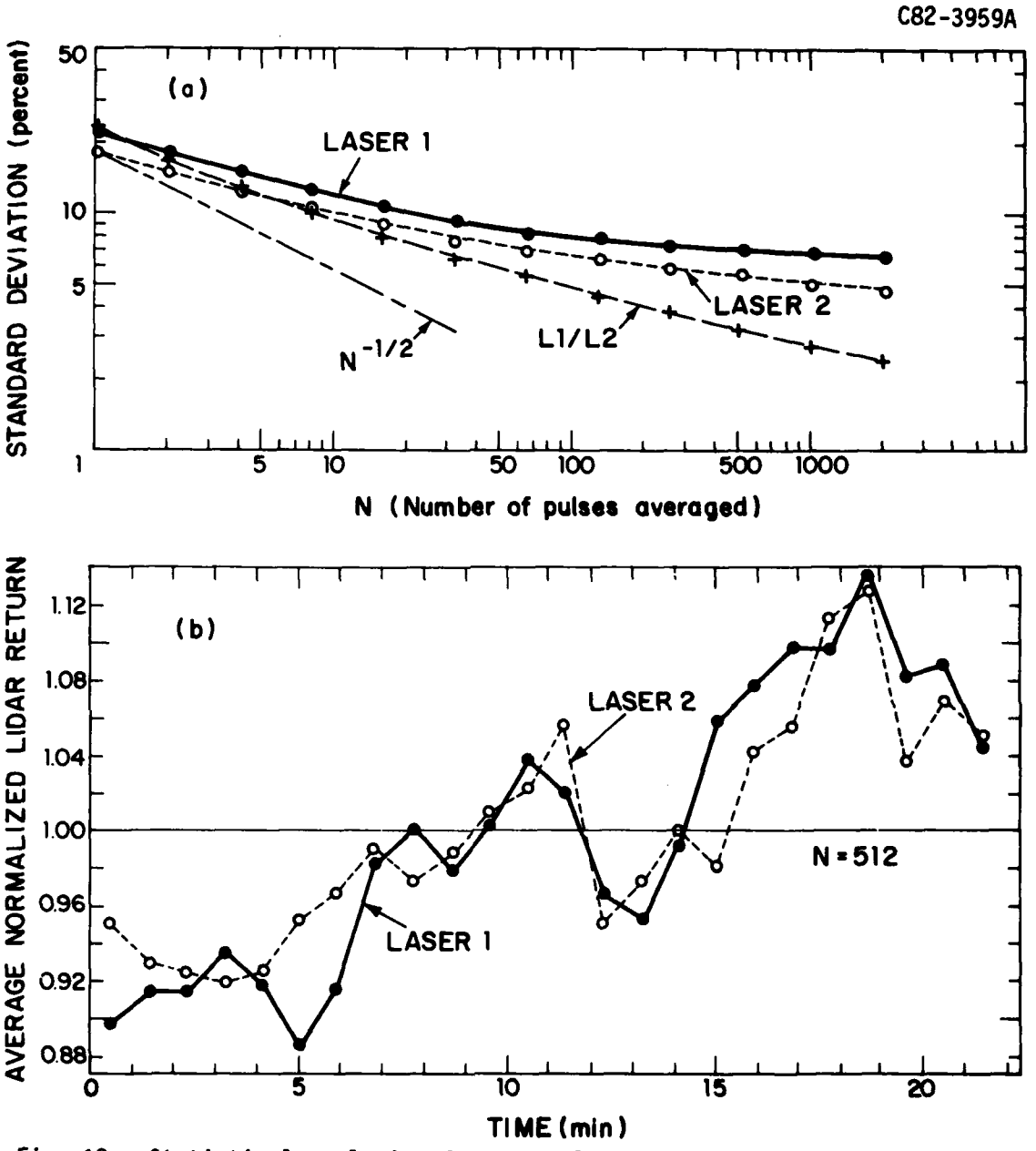

Fig. 12. Statistical analysis of segmentally averaged final set of 12288 normalized pulses from laser 1 and 2. (a) standard deviation of the segment averages of each of the lasers and of their ratio as a function of N, the number of pulses averaged per segment, (b) variation of the average value of the individual segments with time for N = 512.

UNCLASSIFIED

SECURITY CLASSIFICATION OF THIS PAGE *(When Data Entered)*

REPORT DOCUMENTATION PAGE		READ INSTRUCTIONS BEFORE COMPLETING FORM
1. REPORT NUMBER ESD-TR-82-014 ESL-TR-82-016	2. GOVT ACCESSION NO. AD-A115 443	3. RECIPIENT'S CATALOG NUMBER
4. TITLE *(and Subtitle)* Remote Sensing of Turbine Engine Gases		5. TYPE OF REPORT & PERIOD COVERED Final Report 1 October 1980 — 30 September 1981 6. PERFORMING ORG. REPORT NUMBER
7. AUTHOR*(s)* Dennis K. Killinger, Norman Menyuk, Aram Mooradian		8. CONTRACT OR GRANT NUMBER*(s)* F19628-80-C-0002
9. PERFORMING ORGANIZATION NAME AND ADDRESS Lincoln Laboratory, M.I.T. P.O. Box 73 Lexington, MA 02173-0073		10. PROGRAM ELEMENT, PROJECT, TASK AREA & WORK UNIT NUMBERS Program Element No. 62601F Project No. 19002023
11. CONTROLLING OFFICE NAME AND ADDRESS Engineering and Services Laboratory Air Force Engineering and Services Center Tyndall AFB, FL 32403		12. REPORT DATE 30 September 1981 13. NUMBER OF PAGES 90
14. MONITORING AGENCY NAME & ADDRESS *(if different from Controlling Office)* Electronic Systems Division Hanscom AFB, MA 01731		15. SECURITY CLASS. *(of this report)* Unclassified 15a. DECLASSIFICATION DOWNGRADING SCHEDULE

16. DISTRIBUTION STATEMENT *(of this Report)*

Approved for public release; distribution unlimited.

17. DISTRIBUTION STATEMENT *(of the abstract entered in Block 20, if different from Report)*

18. SUPPLEMENTARY NOTES

None

19. KEY WORDS *(Continue on reverse side if necessary and identify by block number)*

laser remote sensing
turbine engine gases
environmental monitoring
tactical detection and discrimination
mini-TEA CO_2 laser
LIDAR (DIAL) system
remote detection of CO, NO, C_2H_4, hydrazine MMH and UDMH

20. ABSTRACT *(Continue on reverse side if necessary and identify by block number)*

This is the FY 81 final report on the program entitled "Remote Sensing of Turbine Engine Gases", supported by the Air Force Engineering and Services Center (AFESC).

The specific tasks which were conducted during FY 81 for this research program consisted of the following: (1) the feasibility demonstration of a dual-laser differential-absorption LIDAR (DIAL) system for the remote sensing of CO, NO, and C_2H_4, (2) the development of a data acquisition and processing system for the dual-laser DIAL system, (3) the laser remote sensing of CO and C_2H_4 in the exhaust of a stationary jet aircraft, and (4) the laser remote sensing of hydrazine, monomethylhydrazine (MMH), and unsymmetrical dimethylhydrazine (UDMH).

DD FORM 1 Jan 73 1473 EDITION OF 1 NOV 65 IS OBSOLETE

UNCLASSIFIED

SECURITY CLASSIFICATION OF THIS PAGE *(When Data Entered)*


DATE
FILME
7-8